

2022

Semiconductor laser dynamics induced by optical feedback for photonic microwave sensing

Bairun Nie

Follow this and additional works at: <https://ro.uow.edu.au/theses1>

University of Wollongong

Copyright Warning

You may print or download ONE copy of this document for the purpose of your own research or study. The University does not authorise you to copy, communicate or otherwise make available electronically to any other person any copyright material contained on this site.

You are reminded of the following: This work is copyright. Apart from any use permitted under the Copyright Act 1968, no part of this work may be reproduced by any process, nor may any other exclusive right be exercised, without the permission of the author. Copyright owners are entitled to take legal action against persons who infringe their copyright. A reproduction of material that is protected by copyright may be a copyright infringement. A court may impose penalties and award damages in relation to offences and infringements relating to copyright material.

Higher penalties may apply, and higher damages may be awarded, for offences and infringements involving the conversion of material into digital or electronic form.

Unless otherwise indicated, the views expressed in this thesis are those of the author and do not necessarily represent the views of the University of Wollongong.

Research Online is the open access institutional repository for the University of Wollongong. For further information contact the UOW Library: research-pubs@uow.edu.au



SEMICONDUCTOR LASER DYNAMICS INDUCED BY OPTICAL FEEDBACK FOR PHOTONIC MICROWAVE SENSING

A Thesis Submitted in Partial Fulfilment of
the Requirements for the Award of the Degree of

Doctor of Philosophy

from

UNIVERSITY OF WOLLONGONG

by

BAIRUN NIE

Supervisor: A/Prof. Yanguang Yu
Co-supervisors: A/Prof. Qinghua Guo and Prof. Jiangtao Xi

School of Electrical, Computer and Telecommunications Engineering
Faculty of Engineering and Information Sciences

August 2022

CERTIFICATION

I, BAIRUN NIE, declare that this thesis, submitted in partial fulfilment of the requirements for the award of Doctor of Philosophy, in the School of Electrical, Computer and Telecommunications Engineering, Faculty of Engineering and Information Sciences, University of Wollongong, is wholly my own work unless otherwise referenced or acknowledged. The document has not been submitted for qualifications at any other academic institution.

BAIRUN NIE
17 August 2022

Dedicated to

My Family

Table of Contents

| | |
|--|-----------|
| List of Tables | iii |
| List of Figures | vii |
| ABSTRACT | viii |
| Acknowledgements | x |
| Publications in Ph.D. Study | xi |
| 1 Introduction | 1 |
| 1.1 Semiconductor Laser Dynamics | 1 |
| 1.2 Microwave Photonics | 4 |
| 1.3 Aims and Thesis Overview | 7 |
| 2 Literature Review | 10 |
| 2.1 Stability Behavior in Semiconductor Laser Dynamics | 10 |
| 2.1.1 Three-mirror model | 10 |
| 2.1.2 Lang-Kobayashi model | 13 |
| 2.1.3 Self-mixing interferometry | 17 |
| 2.2 Instability Behavior in Semiconductor Laser Dynamics | 22 |
| 2.2.1 Dynamic route path | 22 |
| 2.2.2 Determine boundary between stability and instability | 26 |
| 2.3 Photonic Microwave Signals Generation | 30 |
| 2.3.1 Microwave generation technologies | 30 |
| 2.3.2 Period-one oscillation technology | 34 |
| 3 New Approach for Period-one Photonic Microwave and Its Displacement Measurement | 38 |
| 3.1 Chapter Introduction | 38 |
| 3.2 Principle of SL with OF System | 41 |
| 3.2.1 Numerical study of SL with OF system | 41 |
| 3.2.2 MWP generation in P1 dynamics | 44 |
| 3.3 Proposed New Method for Displacement Measurement | 49 |
| 3.3.1 Determine P1 region and its influence parameters | 49 |
| 3.3.2 Utilizing P1 region for displacement sensing | 51 |
| 3.3.3 Model of laser intensity in P1 dynamics | 55 |
| 3.4 Experiments | 58 |

| | | |
|----------|---|------------|
| 3.4.1 | Implementation of experimental system | 58 |
| 3.4.2 | Experiment results | 65 |
| 3.5 | Chapter Summary | 70 |
| 4 | New Approach for Enhanced Displacement Measurement with Relaxation Oscillation | 72 |
| 4.1 | Chapter Introduction | 72 |
| 4.2 | The Behavior of Relaxation Oscillation Frequency | 75 |
| 4.3 | Sensing Signal Processing Algorithm | 80 |
| 4.4 | Experiments | 84 |
| 4.4.1 | Experiment results | 84 |
| 4.4.2 | Discussion | 87 |
| 4.5 | Chapter Summary | 90 |
| 5 | New Approach for Absolute Distance Measurement near Hopf-bifurcation Boundary | 92 |
| 5.1 | Chapter Introduction | 92 |
| 5.2 | Operating SL with OF at Switching Status | 95 |
| 5.3 | Absolute Distance Measurement Principle at Switching Status | 98 |
| 5.4 | Experiments | 104 |
| 5.4.1 | Experiment results | 104 |
| 5.4.2 | Measurement uncertainty | 106 |
| 5.5 | Chapter Summary | 109 |
| 6 | Conclusion | 110 |
| 6.1 | Research Contributions | 110 |
| 6.2 | Future Works | 113 |
| | References | 115 |
| A | Vita | 137 |
| B | List of Abbreviations | 138 |

List of Tables

| | | |
|-----|--|----|
| 2.1 | The Physical Meanings of the Symbols in the L-K Equations. | 14 |
| 2.2 | Comparison of MWP Generation Techniques. | 34 |
| 3.1 | Specifications of the Laser Diode HL8325G. | 60 |
| 3.2 | Specifications of the Laser Diode Mount TCLDM9. | 60 |
| 3.3 | Specifications of the Photodetector PDA8GS. | 61 |
| 3.4 | Specifications of the PZT PAS-009. | 62 |
| 3.5 | Specifications of the Oscilloscope DSA70804. | 62 |
| 3.6 | Displacement Results by PZT Controller and Proposed Algorithm. . . . | 70 |
| 4.1 | The Influence of J 's Control Accuracy on Measurement Error with $\kappa = 2.5 \times 10^{-3}$, $L = 300mm$ | 89 |
| 4.2 | The Influence of κ 's Control Accuracy on Measurement Error with $J/J_{th} = 1.1$, $L = 300mm$ | 90 |

List of Figures

| | | |
|------|--|----|
| 1.1 | Schematic diagrams of SLs under external perturbations for nonlinear dynamics. (a) Optical feedback scheme. (b) Optical injection scheme. (c) Current modulation scheme. (d) Optoelectronic feedback scheme. . | 2 |
| 1.2 | Schematic diagrams of (a) A conventional microwave system. (b) A typical microwave photonic system. (c) Our proposed principle for microwave system. | 5 |
| 2.1 | Simplified schematic diagram for the three mirrors model. | 10 |
| 2.2 | T-C diagram with five feedback regimes. | 17 |
| 2.3 | (a) Relationship between ϕ_s and ϕ_0 . (b) Relationship between g and ϕ_0 , when $C = 0.3$ and $\alpha = 3$ | 18 |
| 2.5 | (a) Relationship between ϕ_s and ϕ_0 . (b) Relationship between g and ϕ_0 , when $C = 2.5$ and $\alpha = 3$ | 19 |
| 2.4 | (a) Time-varying optical phase induced by a moving target. (b) Corresponding SMI signal when $C = 0.3$ and $\alpha = 3$ | 19 |
| 2.6 | (a) Time-varying optical phase induced by a moving target. (b) Corresponding SMI signal when $C = 2.5$ and $\alpha = 3$ | 20 |
| 2.7 | (a) Relationship between ϕ_s and ϕ_0 . (b) Relationship between g and ϕ_0 , when $C = 6$ and $\alpha = 3$ | 21 |
| 2.8 | (a) Time-varying optical phase induced by a moving target. (b) Corresponding SMI signal when $C = 6$ and $\alpha = 3$ | 21 |
| 2.9 | (a) S: steady state, and $\kappa = 0.003$. (b) P1: period-one state, and $\kappa = 0.006$. (c) QP: quasi-period state, and $\kappa = 0.010$. (d) C: chaos state, and $\kappa = 0.014$. (i) Waveform diagrams for different states. (ii) Power spectrum diagrams. (iii) Phase space diagrams. | 23 |
| 2.10 | Bifurcation diagram when $\alpha = 3$, $L = 210mm$, and $J = 1.1J_{th}$. S: steady state; P1: period-one state; QP: quasi-period state; C: chaos state. | 24 |
| 2.11 | Temporal waveform of the relaxation oscillation of the laser intensity when the laser is turned on. | 26 |
| 2.12 | Relaxation oscillation frequency as a function of the external cavity length. | 29 |
| 2.13 | Stability boundary described in the 3-parameter space of (κ, τ, J) , where $\tau = 2L/c$. The unstable region is above the surface. | 30 |

| | | |
|------|---|----|
| 3.1 | Schematic structure of an SL with OF system for displacement sensing. SL: semiconductor laser; BS: beam splitter; PD: photodetector. | 40 |
| 3.2 | (a) Typical MWP signal generated from P1 state. (b) Corresponding FFT spectrum of typical MWP signal. (c) Corresponding STFT spectrogram of typical MWP signal. | 45 |
| 3.3 | Frequency linewidth (black) and microwave power (red) as the function of the feedback strength κ | 46 |
| 3.4 | (a)-(c) show the influence of α on the state boundaries. S: steady state; P1: period-one state; QP: quasi-period state; C: chaos state; B_1 : boundary between S and P1; B_2 : boundary between P1 and QP; B_3 : boundary between QP and C. | 47 |
| 3.5 | (a)-(c) show the influence of J on the state boundaries. S: steady state; P1: period-one state; QP: quasi-period state; C: chaos state; B_1 : boundary between S and P1; B_2 : boundary between P1 and QP; B_3 : boundary between QP and C. | 48 |
| 3.6 | Influence of J on the P1 region with $\alpha = 3$. (a) $J = 1.1J_{th}$ and $D_1 = 120mm$. (b) $J = 1.3J_{th}$ and $D_2 = 70mm$. (c) $J = 1.5J_{th}$ and $D_3 = 50mm$ | 50 |
| 3.7 | Influence of α on the P1 region with $J = 1.1J_{th}$. (a) $\alpha = 3$. (b) $\alpha = 4.5$. (c) $\alpha = 6$ | 50 |
| 3.8 | Bifurcation diagram for an SL with OF system, $J = 1.1J_{th}$, $\alpha = 6$, and $L = 300mm$ | 52 |
| 3.9 | Utilizing P1 region for sensing. (a) Displacement of external target. (b) Corresponding MWP sensing signal in P1 region. | 53 |
| 3.10 | Relationship between f_R and ΔL | 53 |
| 3.11 | (a) Numerical solution of $I(t)_{P1-Envelope}$ under different feedback strength κ . (b) Comparison between the analytical solution from Equations (3.17) and the numerical solution from the L-K equations. | 55 |
| 3.12 | The experiment set-up of MWP sensing system. LD: laser diode; BS: beam splitter; VA: variable attenuator; OSC: oscilloscope; PZT: piezo-electric transducer actuator. | 58 |
| 3.13 | Typical characteristic curves of the laser diode Hitachi HL8325G. (The red dotted line is the case adopted in the following experimental operations.) (a) Optical output power versus injection current. (b) Laser wavelength versus operating temperature. | 59 |
| 3.14 | Laser diode and laser diode mount. | 61 |
| 3.15 | Fiber coupler, multi-mode fiber, and photodetector. | 62 |
| 3.16 | Assembled PZT and linear stage. | 63 |
| 3.17 | A typical example in experiments, which captured by the oscilloscope. Green: time domain MWP signal generated from P1 state. Orange: the corresponding spectrum of frequency domain MWP signal. | 64 |
| 3.18 | Mapping of dynamical states in the OF system with the parameter space of J/J_{th} and L . S: steady state; P1: period-one state; QP: quasi-period state. | 65 |

| | | |
|------|--|----|
| 3.19 | The core components of experiment set-up for displacement sensing. SL: semiconductor laser; BS: beam splitter; VA: variable attenuator; PD: photodetector. (The complete physical structure of the experimental system is shown in Figure 3.12.) | 66 |
| 3.20 | Measurement procedure of the proposed approach. | 67 |
| 3.21 | Pre-test results for the relationship between f_R and ΔL with $J = 1.1J_{th}$ ($46.2mA$), $L = 300mm$, and $\alpha = 4$ | 68 |
| 3.22 | Experiment results. (a) MWP sensing signal $E_{start}^2(t)$ at initial position. (b) Spectrum corresponding to the $E_{start}^2(t)$. (c) MWP sensing signal $E_{end}^2(t)$ at end position. (d) Spectrum corresponding to the $E_{end}^2(t)$ | 69 |
| 3.23 | (a) A linear displacement applied on target by PZT. (b) The corresponding MWP sensing signal. | 70 |
| 4.1 | The schematic diagram of MWP displacement sensing system. SL: semiconductor laser; LC: laser controller; BS: beam splitter; OI: optical isolator; PD: photodetector; OA: optical attenuator; OSC: oscilloscope; LMS: linear motor stage; PZT: piezoelectric transducer actuator. | 75 |
| 4.2 | State diagram in the coordinate plane of (κ, L) for the MWP displacement sensing system with $J = 1.1J_{th}$. S: steady state; P1: period-one state; QP: quasi-period state. B_1 : boundary between S and P1; B_2 : boundary between P1 and QP. | 76 |
| 4.3 | (a) Typical MWP signals generated from P1 state with $\kappa = 2.5 \times 10^{-3}$, $J = 1.1J_{th}$. (b) Corresponding spectrums of typical MWP signals. | 77 |
| 4.4 | (a) Relationship between f_R and L with $\kappa = 2.5 \times 10^{-3}$, $J = 1.1J_{th}$. (b) Enlargement of rectangular area 'M' with $L \in [410.00mm, 417.80mm]$ | 79 |
| 4.5 | Relationship between f_R and ΔL . (a) Enlargement of area 'a' with $\Delta L \in [4000\lambda_0, 4001.5\lambda_0]$. (b) Enlargement of area 'b' with $\Delta L \in [5923\lambda_0, 5924.5\lambda_0]$ | 80 |
| 4.6 | Measurement procedure of proposed algorithm. | 82 |
| 4.7 | (a) MWP signals at initial position and end position. (b) The relaxation oscillation frequencies corresponding to the initial position and the end position. | 83 |
| 4.8 | Experimental set-up. SL: semiconductor laser; BS: beam splitter; PD: photodetector; OA: optical attenuator; LMS: linear motor stage; PZT: piezoelectric transducer actuator. | 84 |
| 4.9 | Experiment results. (a) Relaxation oscillation frequency variation with displacements. (b) Spectrum for MWP sensing signal at start position. (c) Spectrum for MWP sensing signal at end position. | 85 |
| 4.10 | (a) The relationship between J and f_R . (b) The relationship between κ and f_R | 88 |
| 4.11 | The effect of injection current on the state diagram. (a) $J/J_{th} = 1.3$. (b) $J/J_{th} = 1.5$ | 90 |

| | | |
|------|---|-----|
| 5.1 | The experimental set-up of SL with OF distance sensing system. SL: semiconductor laser; LC: laser controller; BS: beam splitter; C: optical fiber coupler; PD: photodetector; OA: optical attenuator; OSC: oscilloscope; L_0 : initial external cavity; L_{01} : free space distance; L_{02} : optical fiber distance; ΔL : distance to be measured. | 96 |
| 5.2 | State diagram for an SLOF sensing system. Red line: Hopf-bifurcation boundary, where period-one state is above the boundary and stable state is below the boundary. Blue vertical dash line: critical external cavity length L_c . Black horizontal dash line: constant feedback strength κ_c | 97 |
| 5.3 | Phase space images of point A, point B, and point C, with $\tau = 200ns$ (corresponding $L = 30m$). (a) $\kappa = 0.0011$. (b) $\kappa = 0.0015$. (c) $\kappa = 0.0065$ | 98 |
| 5.4 | (a) Bifurcation diagrams. (b) Time-series signals $I(t)$ near hopf-bifurcation point (that is the switching status). (c) Phase space images near Hopf-bifurcation point. (i) $\tau_1 = 200ns$ (corresponding $L_1 = 30m$). (ii) $\tau_2 = 250ns$ (corresponding $L_2 = 37.5m$). (iii) $\tau_3 = 300ns$ (corresponding $L_3 = 45m$). The inset figures show the enlarged details. | 99 |
| 5.5 | STFT spectrograms corresponding to (a) $\tau_1 = 200ns$ (corresponding $L_1 = 30m$). (b) $\tau_2 = 250ns$ (corresponding $L_2 = 37.5m$). (c) $\tau_3 = 300ns$ (corresponding $L_3 = 45m$). | 101 |
| 5.6 | (a) Time-series signals $I(t)$ obtained at the switching status with $\tau = 200ns$ and corresponding $L = 30m$. (b) Normalized square wave signal $I(t)_{square-wave}$ obtained from $I(t)$ | 102 |
| 5.7 | (a) The relationship between κ versus duty cycle. (b) The relationship between J versus duty cycle. (c) The relationship between α versus duty cycle. | 103 |
| 5.8 | (a) Experimental square wave signal $I(t)$ with $L_1 = 22.500m$. (b) Experimental square wave signal $I(t)$ with $L_2 = 25.000m$ | 105 |
| 5.9 | Absolute distance measurements results. | 106 |
| 5.10 | (a) The distance measurement uncertainty of L_{02} by introducing different hollow fiber refractive indexes n_2 . (b) The hollow fiber refractive index measurement uncertainty of n_2 by introducing different distances of L_{02} | 108 |

SEMICONDUCTOR LASER DYNAMICS INDUCED BY OPTICAL FEEDBACK FOR PHOTONIC MICROWAVE SENSING

BAIRUN NIE

A Thesis for Doctor of Philosophy

School of Electrical, Computer and Telecommunications Engineering
University of Wollongong

ABSTRACT

As one of the most widely used light sources today, semiconductor lasers (SLs) are an important part of many optical systems, especially for sensing, communications, metrology, and storage applications. SLs have the advantages of small size, easy integration, and miniaturization. The massification of electronic devices has furthered this agenda, allowing the creation of portable systems capable of supporting optical sensing systems. Essentially, SLs are inherently nonlinear devices, in nonlinear systems, the folding and stretching behaviors of variables result in different dynamical routes. It is worth noting that under the conditions of a stable operation, an SL biased by constant current usually emits laser light with a constant intensity. However, with the introduction of external optical feedback (OF), the laser light can become unstable. SL will undergo from steady state, switching status, to period-one (P1) oscillation by crossing Hopf-bifurcation. In the P1 state, the system produces a modulation of the laser optical output power for the generation of microwave photonics (MWP) signals. In this thesis, we operate SL with OF scheme in P1 dynamics, and found that the proposed system has the great capability to achieve both displacement and absolute distance sensing applications with high resolution and wide measurement range, by using time-frequency information, relaxation oscillation information, and nonlinear dynamic characteristics carried in that SLs emit signals. The contributions of each chapter in this thesis are described in the following:

In Chapter 3, we propose an SL with OF set at the P1 dynamics to generate the MWP signal for displacement sensing. Different from the traditional MWP generation method, the designed laser nonlinear dynamics are used by slightly perturbing the SL source with the help of external feedback light to make the system work in the P1 dynamic state, thereby generating regular microwave oscillation. By using the fourth-order Runge-Kutta method to numerically solve the famous Lang-Kobayashi differential equation, the boundary of different laser dynamic states is delimited, so that the system can generate stable and sustainable MWP signals in P1 dynamics. A set of parameter selection rules for designing an SL based MWP displacement sensing system is obtained. In addition, a measurement algorithm for recovering the displacement from an MWP sensing signal is developed. By making full use of the sensing information carried in both amplitude and frequency of the MWP signal, displacement sensing with high resolution and high sensitivity can be achieved. Both simulations and experiments are conducted to verify the proposed method and show it is capable of realizing high measurement sensitivity, and high resolution for displacement sensing.

In Chapter 4, utilizing the rich nonlinear dynamics of an SL with OF, under the

proper controllable system parameters, the system enters the P1 dynamics through Hopf-bifurcation. In the P1 state, the detailed relationship between the relaxation oscillation frequency of MWP signals and external cavity length is studied through solving the Lang-Kobayashi delayed differential equations. The displacement measurement formula is thus obtained. In addition, the relevant signal processing algorithm is developed by considering mode-hopping, frequency-hopping, and sawtooth-like phenomena that occurred in the relaxation oscillation. The displacement measurement can be enhanced in a wider sensing range by fully using the relaxation oscillation frequency relationship. Verification results in simulation and experiment show that the proposed MWP displacement sensing system based on SL with OF contributes to designing a prototype of a compact displacement sensor with wide measurement range and high resolution.

In Chapter 5, OF induced switching status between two nonlinear dynamic states (stable and P1 states) is observed in the SL with OF system. Without the need for any electronic or optical modulation devices, the laser intensity can be modulated in a square wave form due to the switching via utilizing the inherent SL dynamics near Hopf-bifurcation boundary. The periodicity in the switching enables us to develop a new approach for long-distance sensing compared to other SL with OF based absolute distance measurement systems and lift the relevant restrictions that existed in the systems. Moreover, the impact of system controllable parameters on the duty cycle of the square wave signals generated was investigated as well, aiming to maintain the proposed system robustly operating at the switching status.

KEYWORDS: Semiconductor laser dynamics, optical feedback, photonic microwave, nonlinear dynamics, period-one oscillation, relaxation oscillation, displacement measurement, absolute distance measurement.

Acknowledgements

Four-year Ph.D. study is a long journey and a challenging milestone in my life. The completion of this thesis work would not be possible without the generous support I received from many kind people.

I foremost would like to express my deepest gratitude to my enthusiastic supervisors, A/Prof. Yanguang (Sunny) Yu, A/Prof. Qinghua Guo, and Prof. Jiangtao Xi for their support in all aspects throughout my Ph.D. journey. Not only for their tremendous academic support, but also for giving me so many wonderful opportunities. Without their enlightened instruction, impressive kindness, and patience, I could not have completed my thesis. Their keen and vigorous academic observation enlightened me not only during this thesis but I know it will continue to do so in my future career.

I extend my thanks to the University of Wollongong for the IPTA and UPA scholarship as financial support for me. Many thanks to the staff in the School of Electrical, Computer, and Telecommunications Engineering who have helped me to develop a fundamental and essential academic competence. My deep gratitude to many kind people, Dr. Bin Liu, Dr. Yuxi Ruan, Zhuqiu Chen, Can Fang, and Dr. Han Wang in the SPICR laboratory for their guidance and discussions. Many thanks also to friends Lei Mao, Honglin Ren, Jirui Guo, Di Pan, Lei Yu, Kaiyi Cao, and Qingtian Wang for their kind help, advisement, and encouragement. I treasure the time spent with all of them, and will always miss the fishing time in beautiful Lake Illawarra.

A special acknowledgment would like to give to the reviewers of this thesis and anonymous reviewers of previous journal publications. Thanks for all your suggestions, recommendations, and positive/negative comments. Only through a good peer-review process, it is possible to take a further step in research.

Finally, my most sincere thanks to my wife Chaohui (Cara) Chen, and my parents Yudong Nie, Ximei Chao for their incredible support, especially during my Ph.D. study going through the disaster of the global pandemic COVID-19 in human history. They gave me endless support and encouragement to pursue all of my passions. They are the most important people in my world and I dedicate this thesis to them.

Publications in Ph.D. Study

Journal Papers:¹

[J1] **B. Nie**, Y. Ruan, Y. Yu, Q. Guo, J. Xi, J. Tong, “Period-one microwave photonic sensing by a laser diode with optical feedback”, *IEEE Journal of Lightwave Technology*, vol. 38, no. 19, pp. 5423-5429, 2020. [IF: 4.439; JCR: Q1]

DOI: 10.1109/JLT.2020.2993320

[J2] **B. Nie**, Y. Ruan, Y. Yu, Q. Guo, J. Xi, J. Tong, H. Du, “Microwave photonic sensing for high performance displacement measurement based on period-one dynamics in a laser”, *IEEE Journal of Lightwave Technology*, vol. 40, no. 20, pp. 6737-6744, 2022. [IF: 4.439; JCR: Q1]

DOI: 10.1109/JLT.2022.3176318

[J3] **B. Nie**, Y. Ruan, Y. Yu, Q. Guo, C. Fang, J. Xi, J. Tong, H. Du, “Achieving long distance sensing using semiconductor laser with optical feedback by operating at switching status”, *Sensors*, vol. 22, no. 3, art. no. 963, 2022. [IF: 3.847; JCR: Q2]

DOI: 10.3390/s22030963

[J4] Z. Chen, Y. Yu, Y. Ruan, **B. Nie**, J. Xi, Q. Guo, J. Tong, “Dual-frequency doppler lidar based on external optical feedback effect in a laser”, *Sensors*, vol. 20, no. 21, art. no. 6303, 2020. [IF: 3.847; JCR: Q2]

DOI: 10.3390/s20216303

Conference Papers:

[C1] **B. Nie**, Y. Ruan, Z. Chen, Y. Yu, Q. Guo, J. Xi, J. Tong, “State boundaries in a laser diode with optical feedback and its sensing application”, pp. LTh4B-7, *Laser Congress (ASSL, LAC, LSC)*, OSA, Vienna, Austria, 2019.

DOI: 10.1364/LSC.2019.LTh4B.7

[C2] **B. Nie**, Z. Chen, Y. Ruan, Y. Yu, Q. Guo, J. Xi, J. Tong, “Chaotic lidar sensing performance analysis based on laser diode with optical feedback”, pp. JW7A.87, *Frontiers in Optics*, OSA, Washington, DC United States, 2021.

¹The content of this thesis involves publications of [J1, J2, J3, C1], other publications do not appear in this thesis.

DOI: 10.1364/FIO.2021.JW7A.87

[C3] Z. Chen, **B. Nie**, Y. Ruan, Y. Yu, Q. Guo, J. Xi, J. Tong, “Dual-frequency doppler lidar using periodic window with period-6 based on external optical feedback effect in a laser diode”, pp. FM1B.3, *Frontiers in Optics*, OSA, Washington, DC United States, 2021.

DOI: 10.1364/FIO.2021.FM1B.3

[C4] Q. Cheng, **B. Nie**, B. Ji, Y. Ruan, Y. Yu, “Development of a simulation platform for studying the dynamics of a semiconductor laser”, pp. JW6B-28, *Frontiers in Optics*, OSA, Washington, DC United States, 2020.

DOI: 10.1364/FIO.2020.JW6B.28

[C5] Y. Ruan, **B. Nie**, Y. Yu, J. Xi, Q. Guo, J. Tong, Z. Chen, “Achieving high resolution measurement using laser diode operating at period-one”, vol. 11197, pp. 111970I, *Future Sensing Technologies*, SPIE, Tokyo, Japan, 2019.

DOI: 10.1117/12.2542592

[C6] Y. Ruan, **B. Nie**, Z. Chen, Y. Yu, Q. Guo, J. Xi, J. Tong, “Sensing using dynamics of a laser diode with dual-cavity”, pp. LTh4B-5, *Laser Congress (ASSL, LAC, LSC)*, OSA, Vienna, Austria, 2019.

DOI: 10.1364/LSC.2019.LTh4B.5

[C7] Z. Chen, Y. Ruan, **B. Nie**, Y. Yu, Q. Guo, J. Xi, J. Tong, “Measuring linewidth enhancement factor by laser dynamics”, pp. JM5A-53, *Laser Congress (ASSL, LAC, LSC)*, OSA, Vienna, Austria, 2019.

DOI: 10.1364/ASSL.2019.JM5A.53

Chapter 1

Introduction

1.1 Semiconductor Laser Dynamics

Since the laser was predicted in 1958 [1], and the first ruby laser was invented in 1960 [2]. Soon, it was reported in a gas laser that external optical feedback (OF) can alter the laser intensity and shift its wavelength [3], which is occurred when a fraction of light back-reflected or back-scattered by an external target re-enters the laser inside cavity. At that time, researchers worked on how to suppress this unstable, uncertain output. For instance, through injection locking technology, external light is injected into the laser to achieve laser linewidth compression and low noise coherent laser output [4–6]. On the other hand, although external perturbations can cause undesirable and unpredictable operations in laser systems, they can also cause measurable disturbances to operating parameters, which can be used for metrology purposes. Utilizing characteristics that semiconductor laser (SL) sensitives to external perturbations. SLs can exhibit rich nonlinear dynamics subject to external perturbations, leading to an increase in the dynamical dimension of the system. These nonlinear dynamics contribute to a wide range of applications, including photonic microwave generation, laser sensing, secure communications, fast random bit sequence generation [6–9]. Typical

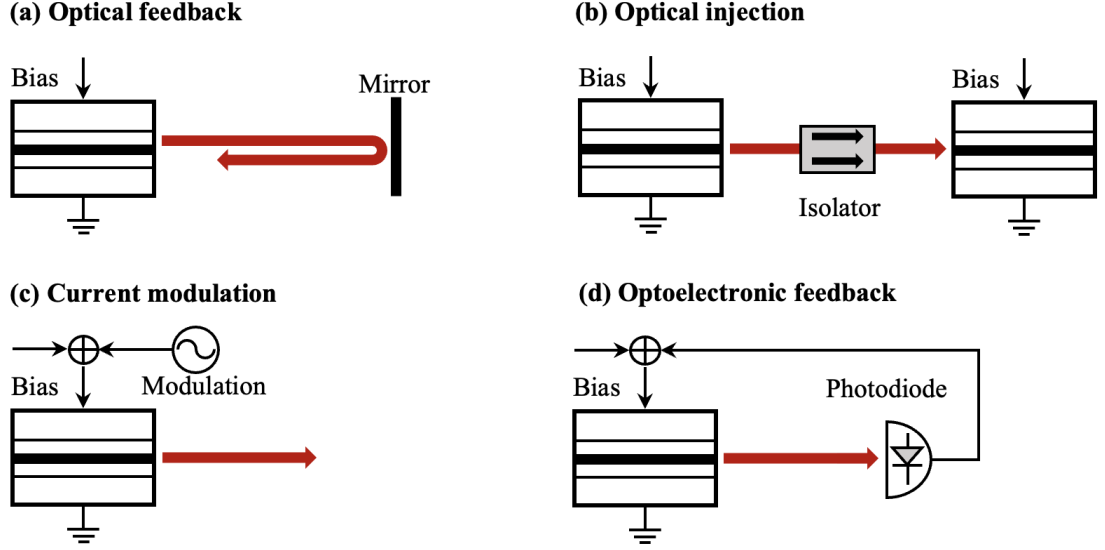


Figure 1.1: Schematic diagrams of SLs under external perturbations for nonlinear dynamics. (a) Optical feedback scheme. (b) Optical injection scheme. (c) Current modulation scheme. (d) Optoelectronic feedback scheme.

perturbation models including optical feedback, optical injection, current modulation, and optoelectronic feedback are depicted in Figure 1.1(a)-(d), respectively.

Optical feedback scheme in Figure 1.1(a): Returning a small fraction of the lasing emission into the SL inside cavity may result in rich nonlinear dynamics, with increasing perturbation, the SL gradually crosses the Hopf-bifurcation from the steady state, into the period-one (P1) oscillation state, quasi-period state, and finally towards the chaos state. The richness of the dynamics stems from the competition between the intrinsic relaxation oscillation frequency of the laser and the external cavity frequency [6].

Optical injection scheme in Figure 1.1(b): A laser from another SL can also be used to destabilize the laser output. The detuning frequency and injection strength are used to excite the nonlinear dynamics of the SL, which in turn can be designed and selected for specific needs. Similar with optical feedback, injection of either a polarized field or a single-mode into a laser emitting in several polarizations or longitudinal

mode components leads to new mechanisms for chaos instabilities but simultaneously provides additional ways to control the dynamics [10, 11]. However, optical injection often involves more than one laser, which increases the cost of the system.

Current modulation scheme in Figure 1.1(c): Current modulation is a perturbation scheme that introduces a variation of the charge carriers by varying the bias current. By breaking the equilibrium of charge carriers, current modulation can increase the dynamical dimension of the system, and thus inducing instabilities. However, experiment results showed that the intrinsic noise from quantum fluctuations typically prevents the observation of a period-doubling cascade to chaos, unless there is a careful tuning of both the modulation frequency and depth [12, 13].

Optoelectronic feedback scheme in Figure 1.1(d): The output of the SL is converted to an electrical current by a photodiode, then, utilizing amplified and re-applied an electrical feedback signal to the bias. In this way, the SL experiences a time-delayed contribution to its dynamics. The feedback may be positive or negative depending on the polarity of the amplifier in the feedback loop. Nonlinear dynamics typically arise when the time delay is larger than the laser relaxation oscillation time period [6]. However, optoelectronic feedback requires a complicated system setup and costly electronics.

In summary, no matter which of the above schemes, as a typical class B laser, SL shows instability, and complex dynamic characteristics only when some perturbations are introduced to increase the dynamical dimensions in the system. SLs are widely used in numerous applications due to their high efficiency, small size, compatibility with electronic components, and ease of pumping and modulation by current injection. These advantages allow many different ways to perturb SLs to exhibit a variety of nonlinear dynamics tailored to specific applications. In this thesis, with the aid of the many advantages in SLs mentioned, based on OF scheme, SL will undergo from

steady state, switching status, to P1 oscillation by crossing Hopf-bifurcation. The P1 dynamics produce an intensity-modulated optical wave and give regular pulsation at microwave frequencies for microwave photonics (MWP) signals generation. Utilizing the MWP signals generated in P1 dynamics, we develop and test capable of sensing applications for SL with OF system. The diversity of MWP are discussed in the next section.

1.2 Microwave Photonics

Back again to 1960s, when the laser was first invented, at the same time the idea of modulating the output of the laser in the microwave frequency range was proposed in 1962 [14]. Since then, many microwave generation technologies have been invented and extensive investments have been made [8, 15–18]. In a conventional microwave system, microwave or intermediate frequency (IF) signals are distributed or processed in the electrical domain using electronic components, as shown in Figure 1.2(a). To take benefits from modern photonics, the current MWP technology introduces broadband electrical-to-optical (EO) and optical-to-electrical (OE) conversions to the system so that the signals can be transmitted in an optical fiber or processed in the optical domain using optical devices, as shown in Figure 1.2(b). EO conversion with a bandwidth of several or tens of gigahertz can be implemented by a direct-modulated SL or a continuous-wave (CW) laser source together with an external modulator. For an SL, the output optical power would increase linearly with the drive current in a certain range, so EO conversion can be realized if the SL is properly biased and the drive current to the SL is controlled by a microwave or IF signal. In this thesis, a method to generate MWP is proposed. In a word, based on SL with OF, the SL is modulated through external optical feedback, and after OE conversion, the system directly outputs the MWP signal as shown in Figure 1.2(c), and detailed studies and

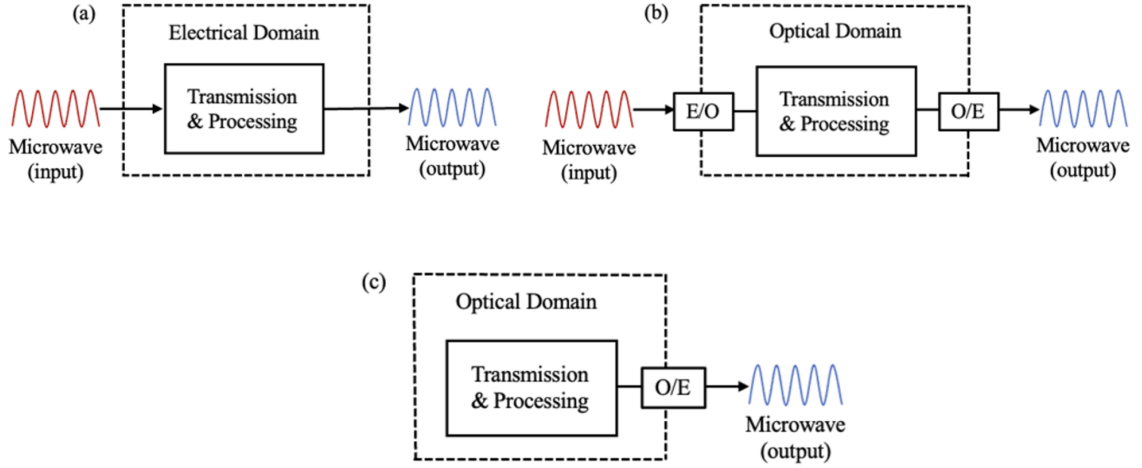


Figure 1.2: Schematic diagrams of (a) A conventional microwave system. (b) A typical microwave photonic system. (c) Our proposed principle for microwave system.

investigations are in the subsequent chapters.

MWP brings together the worlds of optoelectronics and microwave engineering, opening a door for numerous promising applications [17]. Over the past few decades, efforts have been made to improve functionality, accuracy, and response time of sensing applications, where high-speed generation, control, and processing of broadband signals are the key points. With the aids of wide bandwidth, flat response, low-loss transmission, multi-dimensional multiplexing, ultra-fast analog signal processing, and anti-electromagnetic interference provided by modern photonics for sensing applications, the resolution, coverage, and speed have been improved that were difficult to achieve in the past [17, 19]. Furthermore, different microwave photonic sensing application architectures have been recently proposed, which demonstrate the remarkable reconfigurability, versatility, wide-area distribution, and high-resolution imaging capabilities enabled by photonics [19].

Many photonic microwave generation approaches can yield very low phase noise by adopting high-frequency electronic components. These commonly used techniques can be summarized as direct modulation [20], external modulation [21], optical heterodyne

technique with cooperation with optical phase-lock loops (OPLL) [22, 23], and optoelectronic oscillator (OEO) [24]. All these techniques all rely on the high-frequency electronics, which are costly and complex to implement. Thus, some of the photonic microwave generations without relying on high-frequency electronic components were also investigated. These approaches are briefly introduced as follows: self-pulsating laser [25], dual-wavelength laser [26], optoelectronic oscillator [27], passively mode-locked laser [28–30], and P1 dynamics of semiconductor lasers [31–36].

Among these techniques, photonic microwave generation based on P1 oscillation dynamics has gained special attention due to its many advantages, such as widely tunable oscillation frequency, and nearly single-sideband spectrum in optical injection scheme [37]. As well as narrow frequency linewidth and good frequency stability in OF scheme [9, 31]. The P1 oscillation is one of the many nonlinear dynamics such as period-doubled, quasi-periodic, and chaotic oscillation under optical feedback effects on SL. P1 oscillation can be achieved when a stable locked laser experiences a Hopf-bifurcation, in which the intensity of the laser emission is oscillating at a microwave frequency [38, 39]. For photonic microwave generation, the nonlinear dynamical P1 oscillation offers the following advantages over other techniques: The microwave frequency generated from P1 oscillation can be broadly tunable, and it is far beyond the laser's relaxation resonance frequency, in some distributed feedback laser (DFB) lasers, the generated frequency can even be up to terahertz band [40, 41]. The generation of the optical microwave signal can be achieved without using any electronic microwave components [42]. On optical spectra, single-sideband can be generated by adjusting the injection parameters to minimize the chromatic dispersion introduced microwave power penalty during the transmission over long optical fibers [43]. Maximal microwave power at a constant average optical power can be produced because of nearly 100% intensity modulation depth [43, 44], and it is also possible to simultaneously use the bias current

of the electrically modulated laser to modulate the microwave signal [44].

1.3 Aims and Thesis Overview

The aim of the present work is to describe, develop and test the SL with OF system capable of sensing applications, including displacement measurement and absolute distance measurement with both high performances, based on rich nonlinear SL dynamics. Undamped relaxation oscillation and the beating of laser modes are demonstrated as the dominant mechanisms giving rise to complex SL dynamics. It is shown that active OF is essential for the preparation of the whole route path of dynamics for SL. SL will undergo from steady state, switching status, to P1 oscillation by crossing Hopf-bifurcation. The P1 dynamics produce an intensity-modulated optical wave and give regular pulsation at microwave frequencies for MWP signals generation. Subsequently, the thesis completes a field widely investigation and research on OF effects in SLs for sensing applications. MWP sensing and measurement based on inherent SL dynamics are envisioned to be a promising alternative to conventional pure electronic or optical solutions. This thesis involves seven chapters and is organized as below:

Chapter 1 briefly introduces the background of this thesis. In Section 1.1, the background of SL dynamics technology is introduced, which includes the different external perturbations, advantages/disadvantages, and applications. In Section 1.2, the background and technological evolution path of the MWP signal are reviewed, and the P1 dynamics used to generate the MWP signal in this thesis are briefly introduced.

Chapter 2 is the literature review. Firstly, the stable solutions of SL with OF system are derived from both three-mirror model and Lang-Kobayashi (L-K) equations are presented. Then, the rich nonlinear dynamics of SL induced by external OF are presented, which include P1, period-doubled, quasi-periodic, and chaotic oscillation. And determine the stability boundary of an SL with OF system between steady state

and P1 state. Lastly, a summary of the existing MWP generation technology is presented, especially the scheme of using P1 dynamics to generate MWP, and followed by an overview of the progress of MWP applications.

Chapter 3 utilizes an MWP generation method based on SL with OF system and then shows displacement sensing by making full use of the sensing information carried in both amplitude and frequency of the MWP signal. With the aid of a set of parameter selection rules for designing an SL based MWP displacement sensing system, displacement sensing with high resolution can be achieved. The L-K differential equations are solved by using the fourth-order Runge-Kutta method. In particular, the boundaries of different laser dynamic states are delimited, which guarantees the system can generate a stable and sustainable MWP signal. Then, the performance analysis of the generated MWP signals in P1 dynamics, and the experimental system implementation for the sensing platform are demonstrated. Simulations and experiments have been carried out to verify the effectiveness of the method, which displays that the method can achieve a higher measurement sensitivity and high resolution displacement sensing. **[Publication involved: J1, C1]**

Chapter 4 focuses on the detailed relationship between the relaxation oscillation frequency of the MWP signal and the external cavity length in the P1 state, which is studied based on the L-K delay differential equations. The relevant signal processing algorithms are developed by considering the mode-hopping, frequency-hopping, and sawtooth-like phenomena that occur in relaxation oscillation. Consequently, the displacement can be recovered in a wider range by fully using the relaxation oscillation frequency relationship. The verification results show that the proposed MWP displacement sensing system based on SL with OF scheme is helpful for designing a prototype of a compact displacement sensor with wide measurement range and high resolution. **[Publication involved: J2]**

Chapter 5 observes OF induced switching between stable and P1 states in an SL with OF system. Utilizing the inherent dynamics of the SLs, without using any high-speed electronic devices, photonic microwave signals with square wave envelopes can be generated by operating the SL with OF system near the Hopf-bifurcation boundary. It is found that the switching period of the square wave envelope is equal to the external cavity round trip time, which enables us to develop a new approach for long-distance measurement. In addition, the influence of system controllable parameters on the duty cycle are also investigated, a wide tuning range between 0% and 100% is implemented when system controllable parameters are properly adjusted, this ensures the proposed SL with OF system is robust for distance sensing. In proof-of-concept experiments, all test points agree with the theoretical results, showing a good sensing performance. This work contributes to designing a prototype of a compact distance sensor by using a square wave modulated photonic microwave signal configuration to realize a long absolute distance measurement. **[Publication involved: J3]**

Chapter 6 summarizes the contributions of this thesis and relevant publications based on this thesis. Then, it provides suggestions of potential future research directions.

Chapter 2

Literature Review

2.1 Stability Behavior in Semiconductor Laser Dynamics

2.1.1 Three-mirror model

The steady state mathematical model of the semiconductor laser (SL) subjected to optical feedback (OF) can be derived from the classical three-mirror model. The model consists of a Fabry-Perot (FP) type laser with facet reflection coefficients r_1 and r_2 , and the target with the reflection coefficient of r_3 [45, 46]. Therefore, a simplified

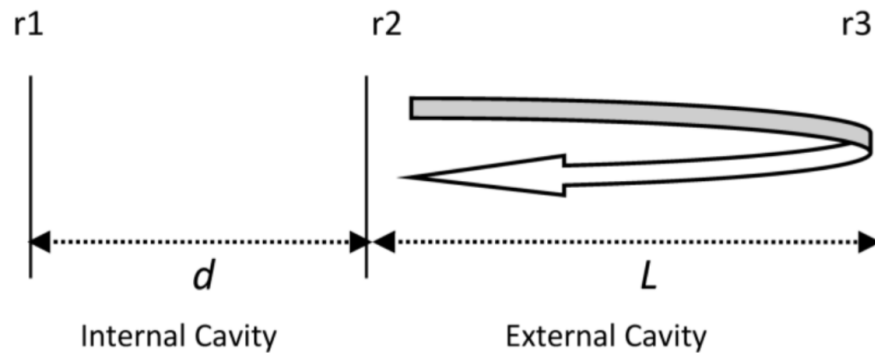


Figure 2.1: Simplified schematic diagram for the three mirrors model.

arrangement based on the schematic diagram shown in Figure 1.1(a) can be used for carrying out the derivation, which is shown in the following Figure 2.1.

Assuming $|r_2 r_3| \ll 1$, i.e., there is only one reflection within the external cavity, the effective reflection coefficient r_{eff} at the laser front facet can be expressed as [45,47]:

$$r_{eff} = A_{eff} \exp(-j\phi_{eff}) = r_2 + (1 - |r_2|^2) r_3 \exp(-j\omega_s \tau) \quad (2.1)$$

Where, ω_s is the laser angular frequency with optical feedback and τ is one round trip time of the light in the external cavity, and $\tau = 2L/c$, where c is the speed of light. Introducing a parameter κ for describing the coupling rate of re-injected light into the internal cavity length, named by optical feedback strength, which is expressed as:

$$\kappa = \eta(1 - |r_2|^2) \frac{r_3}{r_2} \quad (2.2)$$

Where, η is the coupling efficiency which accounts for possible loss on re-injection, e.g. mode mismatch and finite coherence length. When $\kappa \ll 1$, from Equation (2.1), we can get:

$$A_{eff} = r_2 [1 + \kappa \cos(\omega_s \tau)] \quad (2.3)$$

$$\phi_{eff} = \kappa \sin(\omega_s \tau) \quad (2.4)$$

As the roundtrip phase in the internal cavity must be equal to a multiple of 2π , the phase condition of compound cavity of the three-mirror model can be described using the following equation [45,47]:

$$\Delta\phi_L = -\alpha(g_c - g_{th})d + \tau_{in}(\omega_s - \omega_0) + \phi_{eff} \quad (2.5)$$

Where, $\Delta\phi_L$ corresponds to a change in the round trip phase compared to $2q\pi$, where q is an integer. α is called the linewidth enhancement factor, τ_{in} is the light round trip time in the internal cavity and ω_0 is the angular frequency of the solitary laser. g_c and g_{th} are the threshold gain with and without external cavity respectively [45, 48]. g_{th} can be express as:

$$g_{th} = a_s + d^{-1} \ln[(r_1 r_2)^{-1}] \quad (2.6)$$

Where, a_s accounts for any optical loss in the internal cavity. Additionally, g_c must satisfy the amplitude condition of the compound cavity [61, 92]:

$$r_1 A_{eff} \exp[(g_c - a_s)d] = 1 \quad (2.7)$$

Submitting Equation (2.3) and Equation (2.6) into Equation (2.7), we can obtain:

$$g_c - g_{th} = -\frac{\kappa}{d} \cos(\omega_s \tau) \quad (2.8)$$

Then inserting Equation (2.4) and Equation (2.8) into Equation (2.5) and letting $q = 0$, the phase equation of the three-mirror model is shown as below [49]:

$$\omega_s \tau = \omega_0 \tau - \frac{\kappa}{\tau_{in}} \tau \sqrt{1 + \alpha^2} \sin[\omega_s \tau + \arctan(\alpha)] \quad (2.9)$$

If we denote $\phi_s = \omega_s \tau$, $\phi_0 = \omega_0 \tau$, and $C = \frac{\kappa}{\tau_{in}} \tau \sqrt{1 + \alpha^2}$, (where C is feedback level), it can be finally derived as Equation (2.10) which is so-called the core part of self-mixing interferometry.

$$\phi_s = \phi_0 - C \sin[\phi_s + \arctan(\alpha)] \quad (2.10)$$

Where ϕ_s and ϕ_0 are respectively the light phase corresponding to the perturbed

and unperturbed laser angular frequency. Note that although the three-mirror model explains some interesting results, it lacks some details of the physical setting of the phenomenon, e.g., the material and associated effects for an SL [49]. Hence, in next section the well-known Lang-Kobayashi model is introduced.

2.1.2 Lang-Kobayashi model

Equation (2.9) can also be derived from the well-known Lang-Kobayashi (L-K) equations which are based on Lamb's equation and modified with the additional equation for the state concentration [49]. Compared to the three-mirror model, the L-K equations describe the active material and carry a description of laser oscillator equations which yield a much more complete description of the dynamic behavior of a single-mode SL with external OF. The well-known L-K equations [50] were first proposed in 1980 and the model consists of three simultaneous delay differential equations which are shown as below:

$$\frac{dE(t)}{dt} = \frac{1}{2} \left\{ G[N(t), E(t)] - \frac{1}{\tau_p} \right\} E(t) + \frac{\kappa}{\tau_{in}} E(t - \tau) \cos[\omega_0 \tau + \phi(t) - \phi(t - \tau)] \quad (2.11)$$

$$\frac{d\phi(t)}{dt} = \frac{1}{2} \alpha \left\{ G[N(t), E(t)] - \frac{1}{\tau_p} \right\} - \frac{\kappa}{\tau_{in}} \frac{E(t - \tau)}{E(t)} \sin[\omega_0 \tau + \phi(t) - \phi(t - \tau)] \quad (2.12)$$

$$\frac{dN(t)}{dt} = \frac{J}{eV} - \frac{N(t)}{\tau_s} - G[N(t), E(t)] E^2(t) \quad (2.13)$$

In above equations, there are three variables named as electric field amplitude $E(t)$, electric field phase $\phi(t)$, and carrier density $N(t)$. $\phi(t)$ is given by $\phi(t) =$

2.1. Stability Behavior in Semiconductor Laser Dynamics

Table 2.1: The Physical Meanings of the Symbols in the L-K Equations.

| SYMBOL | PHYSICAL MEANING | VALUE |
|---------------|---|----------------------------------|
| G_N | Model gain coefficient | $8.1 \times 10^{-13} m^3 s^{-1}$ |
| N_0 | Carrier density at transparency | $1.1 \times 10^{24} m^{-3}$ |
| ε | Nonlinear gain compression coefficient | $2.5 \times 10^{-23} m^3$ |
| τ_p | Photon lifetime | $2.0 \times 10^{-12} s$ |
| τ_s | Carrier lifetime | $2.0 \times 10^{-9} s$ |
| τ_{in} | Internal cavity round-trip time | $8.0 \times 10^{-12} s$ |
| e | Elementary charge | $1.6 \times 10^{-19} C$ |
| V | Volume of the active region | $1.0 \times 10^{-16} m^3$ |
| ω_0 | Unperturbed optical angular frequency of the SL, $\omega_0 = 2\pi c/\lambda_0$, where c is the speed of light, λ_0 is the wavelength of the SL | |
| Γ | Confinement factor | |
| α | Line-width enhancement factor | |
| J | Injection current | |
| κ | Feedback strength | |
| L | External cavity length | |
| τ | Light round-trip time in the external cavity, $\tau = 2L/c$ | |

$[\omega(t) - \omega_0]t$, where $\omega(t)$ is the instantaneous optical angular frequency for an SL with optical feedback, ω_0 is the unperturbed optical angular frequency for a solitary SL. $G[N(t), E(t)] = G_N [N(t) - N_0] [1 - \varepsilon \Gamma E^2(t)]$ is the modal gain per unit time. The physical meanings of the symbols appearing in Equations (2.11)-(2.13) and the values of the parameters used in this thesis can be found in Table 2.1 [51].

In 1995, the analytical self-mixing interferometry (SMI) or called laser feedback interferometry by solving the steady state solutions of the L-K equations are reported in [52]. Introducing E_s , ω_s , and N_s as the steady state solutions of electric field amplitude, angular frequency and carrier density, by setting $dE(t)/dt = 0$, $d\phi(t)/dt = \omega_s - \omega_0$, and $dN(t)/dt = 0$. Substituting $E(t) = E(t - \tau) = E_s$, $N(t) = N_s$, and $\phi(t) = (\omega_s - \omega_0)t$ into Equations (2.11)-(2.13), and ignoring the nonlinear gain, the well-known stationary solutions can be obtained as below:

$$\omega_s \tau = \omega_0 \tau - \frac{\kappa}{\tau_{in}} \tau \sqrt{1 + \alpha^2} \sin[\omega_s \tau + \arctan(\alpha)] \quad (2.14)$$

$$N_s = N_0 + \frac{1}{\tau_p G_N} - \frac{2\kappa \cos(\omega_s \tau)}{\tau_{in} G_N} \quad (2.15)$$

$$E_s^2 = \frac{J/(eV) - N_s/\tau_s}{G_N(N_s - N_0)} \quad (2.16)$$

Steady solution of SL with OF can be obtained by either the three-mirror model or the L-K model, Equation (2.14) is exactly the same as Equation (2.9). The L-K model is time-dependent and can be used to describe the dynamic properties of active materials. It is found to give a remarkably accurate model of both the weak-level feedback phenomena and the high-level feedback chaos-related dynamics. Although it is deduced on the basis of the performance on laser diodes, it predicts many complex behaviors over short-time scales that have been observed in practice. In contrast to the dynamic L-K model, there also exists three-mirror model of analyzing the laser feedback effect, which employs the geometry of the laser feedback cavity and effective reflectivity. Unlike the dynamic description obtained by adding the feedback effect component in the rate equations as in the L-K model, the three-mirror model employs the static analysis method. The three-mirror model is equivalent to the L-K model in analyzing the phenomena in the laser feedback technology, but the analysis processes of the two models focus on different aspects. The key point in the three-mirror model is to treat the reflective target as the third reflective mirror. This reflective mirror reflects the laser back into the resonant cavity, equivalent to changing the effective reflectivity of the laser output mirror, which induces modulation of the optical field inside the laser cavity.

From Equations (2.14)-(2.16) and by considering a moving target, the existing SMI model can be obtained as below by introducing:

$$\begin{cases} \phi_0 = \omega_0 \tau \\ \phi_s = \omega_s \tau \\ C = (\kappa \tau / \tau_{in}) \sqrt{1 + \alpha^2} \end{cases} \quad (2.17)$$

Then Equation (2.14) becomes:

$$\phi_s = \phi_0 - C \sin [\phi_s + \arctan(\alpha)] \quad (2.18)$$

Where ϕ_0 is associated with the external cavity length L , i.e., $\phi_0 = 4\pi L / \lambda_0$, where λ_0 is the unperturbed laser wavelength.

Equation (2.18) is called the phase equation which is the core part of the existing SMI model, and is the same equation as derived by the three mirrors model [refer Equation (2.10)]. By substituting Equation (2.15) into Equation (2.16), the normalized variation of the SL output power (that is the so called SMI signal g) can be obtained and described as [52]:

$$g = \cos(\phi_s) \quad (2.19)$$

Equations (2.18) and Equation (2.19) constitute the existing SMI model which has been widely accepted to describe the waveforms of SMI signals [47, 52–55]. As seen in Equation (2.18) and Equation (2.19), there is a straight forward procedure to constitute g , i.e., $\phi_0 \rightarrow \phi_s \rightarrow g$, and also a straight backward procedure, i.e., $g \rightarrow \phi_s \rightarrow \phi_0$, to obtain ϕ_0 , thus retrieving the external cavity information. Therefore, the knowledge of the theory of generating a SMI signal as well as its waveform is essential to achieve good performance of the SMI.

2.1.3 Self-mixing interferometry

In the SMI model, C is called optical feedback level as described in Equation 2.17, it is an important quantity for characterizing feedback. It was proposed by Acket in [56] and used to distinguish between the low feedback regime ($C < 1$) and high feedback regime ($C > 1$). A more detailed feedback regimes studied by Tkach and Chraplyvy presented a T-C diagram shown in Figure 2.2 which classified five feedback regimes [57].

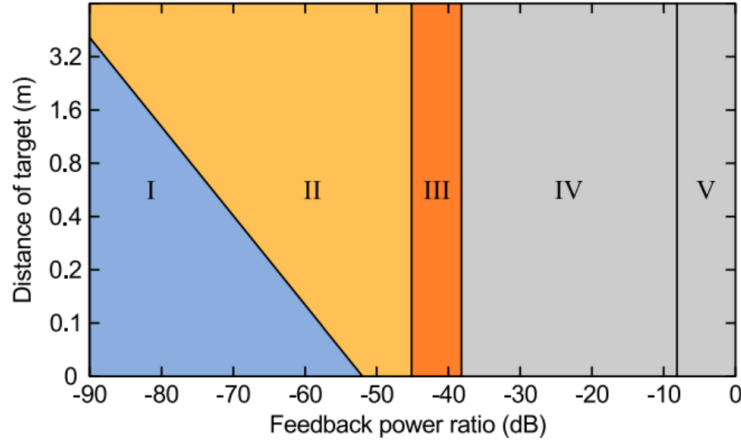


Figure 2.2: T-C diagram with five feedback regimes.

Most of the existing work on behavior study is mainly based on the analytical SMI model, i.e. Equation (2.18) and Equation (2.19). In this SMI model, the parameter C is of great significance, which characterizes the waveform shape of the SMI signal. It has been widely accepted that the operating regime of an SMI system can be divided into three regimes based on the value of C , i.e. weak feedback regime for $C < 1$, moderate feedback regime for $1 < C < 4.6$ and strong feedback regime for $C > 1$ [46, 49].

In weak feedback regime with $C < 1$, a unique mapping between ϕ_0 and ϕ_s can be found based on Equation (2.18). Even in some work, when the SMI is in weak feedback, the approximation of $\phi_s \approx \phi_0$ have been taken [58–61]. Figure 2.3(a) shows the relationship between ϕ_0 and ϕ_s when $C = 0.3$ and $\alpha = 3$. In weak feedback

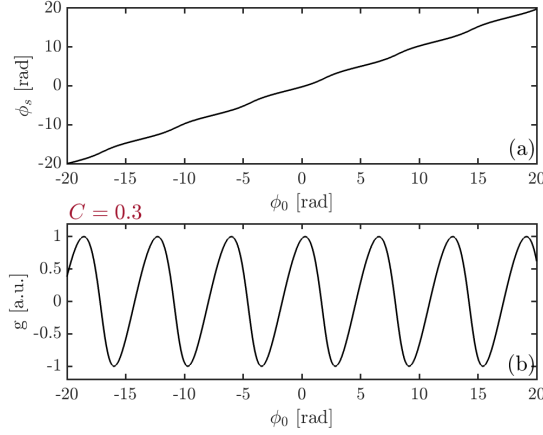


Figure 2.3: (a) Relationship between ϕ_s and ϕ_0 . (b) Relationship between g and ϕ_0 , when $C = 0.3$ and $\alpha = 3$.

regime, the SMI signals induced by a moving target have the similar fringe shape as the traditional two-beam interferometry, and also each fringe in SMI signals corresponds to half wavelength displacement ($\lambda_0/2$) for the external target. Figure 2.3(b) shows the relationship between SMI signal g and ϕ_0 .

Supposing an continuous sinusoidal displacement is applied on the target with $L(t) = L_0 + \Delta L \sin(2\pi f t)$, where L_0 , ΔL , and f are the initial external cavity length, the amplitude of the displacement and target vibrating frequency respectively, which are chosen as $L = 0.24m$, $\Delta L = 1.5\lambda_0$, and $f = 400kHz$. In this case, the variation of the initial optical phase can be expressed as: $\Delta\phi_0(t) = 4\pi\Delta L \sin(2\pi f t)/\lambda_0$. Figure 2.4 shows the time-varying optical phase and its corresponding SMI signal. It can be found the SMI signal in Figure 2.4(b) has the similar fringe shape as the traditional two-beam interferometry.

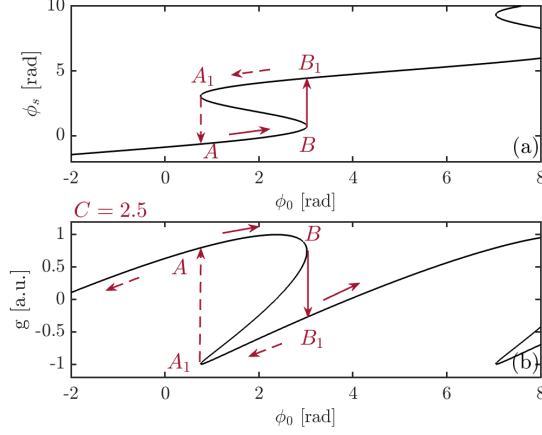


Figure 2.5: (a) Relationship between ϕ_s and ϕ_0 . (b) Relationship between g and ϕ_0 , when $C = 2.5$ and $\alpha = 3$.

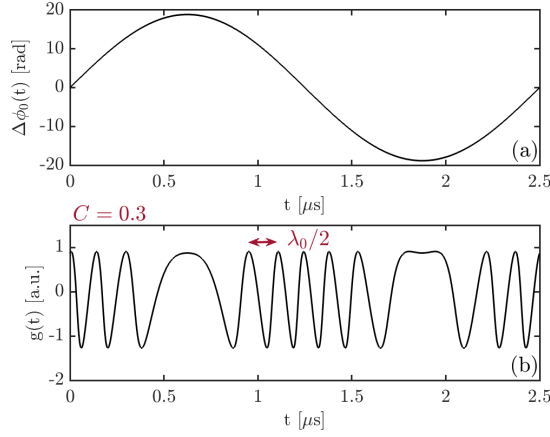


Figure 2.4: (a) Time-varying optical phase induced by a moving target. (b) Corresponding SMI signal when $C = 0.3$ and $\alpha = 3$.

In moderate feedback regime with $1 < C < 4.6$, three possible ϕ_0 may be yielded from Equation (2.18), two are stable and one is unstable. In this case, the SMI signals show hysteresis and producing sawtooth-like fringes. Varieties of SMI-based applications have set the SMI system in moderate feedback regime, and the behavior of SMI in this regime have been investigated intensely [52, 56, 62, 63]. Figure 2.5 shows the relationship between ϕ_0 and ϕ_s as well as g and ϕ_0 when $C = 2.5$ and $\alpha = 3$.

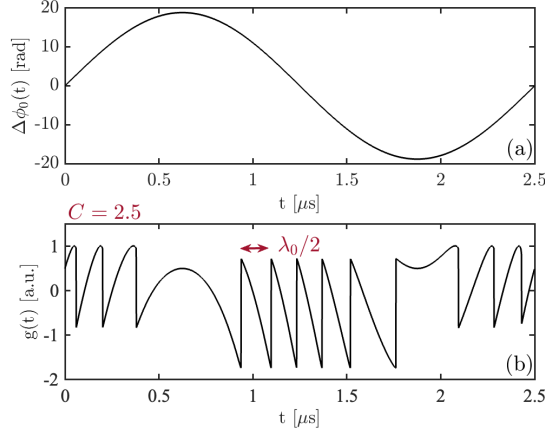


Figure 2.6: (a) Time-varying optical phase induced by a moving target. (b) Corresponding SMI signal when $C = 2.5$ and $\alpha = 3$.

Based on the behavior analysis in [52, 63], when ϕ_0 increases, that ϕ_s and g will track the route $A \rightarrow B \rightarrow B_1$ and it will vary following the route $B_1 \rightarrow A_1 \rightarrow A$ when ϕ_0 decreases. When ϕ_0 locates between point A and B , ϕ_0 will yields three ϕ_s , and the one located on the line $A_1 - B$ is unstable. Similarly, suppose a continuous sinusoidal displacement is applied on the target as same as in Figure 2.4(a), then we can get the corresponding SMI signal $g(t)$ as shown in Figure 2.6(b).

In strong feedback regime with $C > 4.6$, five or seven or even more possible ϕ_s may be yielded from Equation (2.8). In this situation, the SMI signals may experience fringe loss [46, 64, 65]. Additionally, when C increases to certain values, the shape of the SMI signals may closely replicates that of the external movement [46]. In 2009, Y. Yu et al. [65] studied the behavior of SMI system with a large C , and gave the details about the mode jumping rules, i.e. for a given ϕ_0 , which ϕ_s should be chosen. Figure 2.7 shows the relationship between ϕ_0 and ϕ_s as well as g and ϕ_0 when $C = 6$ and $\alpha = 3$. Based on the behavior analysis in [65], when ϕ_0 increases, that ϕ_s and g will track the route $B \rightarrow B_1 \rightarrow D \rightarrow D_1$ and it will vary following the route $C_1 \rightarrow C \rightarrow A_1 \rightarrow A$ when ϕ_0 decreases. Similarly, let's suppose a continuous sinusoidal displacement is applied on the target as same as in Figure 2.4(a), then we can get the corresponding

SMI signal $g(t)$ as shown in Figure 2.8(b).

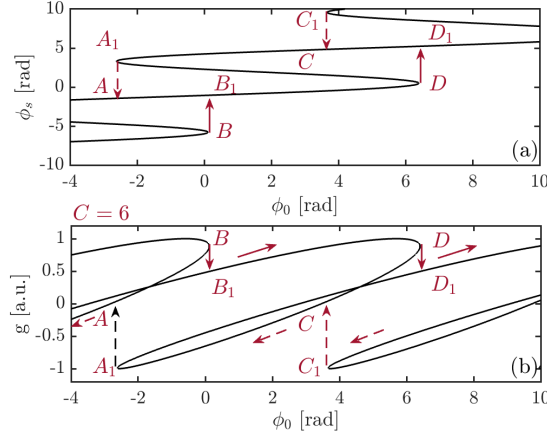


Figure 2.7: (a) Relationship between ϕ_s and ϕ_0 . (b) Relationship between g and ϕ_0 , when $C = 6$ and $\alpha = 3$.

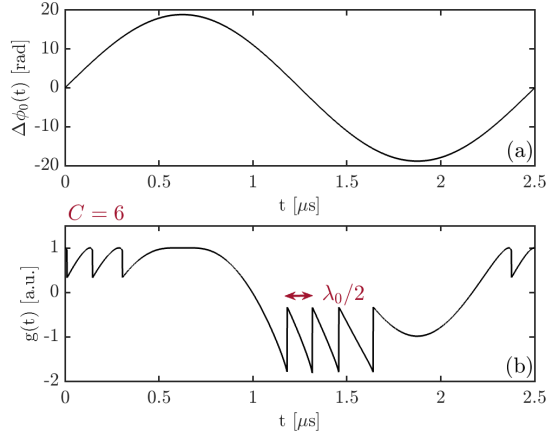


Figure 2.8: (a) Time-varying optical phase induced by a moving target. (b) Corresponding SMI signal when $C = 6$ and $\alpha = 3$.

2.2 Instability Behavior in Semiconductor Laser Dynamics

2.2.1 Dynamic route path

With further research on SL with the influence of optical feedback or optical injection, researchers realized that SL can achieve rich nonlinear dynamics and operated SL above steady state [66–70]. Of the five regions classified in the T-C diagram in Figure 2.2, four of them involve nonlinear dynamics [71]. With the system parameters change (e.g. increase external feedback or increase injection current), the SL dynamic route path will undergo from steady (S) state, period-one (P1) oscillation, quasi-period (QP) oscillation to chaos (C) oscillation.

When fixed $\alpha = 3$, $L = 210mm$, and $J = 1.1J_{th}$, where J_{th} is the threshold of the injection current. The dynamic behaviors of the SL output are showed in Figure 2.9(a)-(d) with four different feedback strength $\kappa = 0.003$, $\kappa = 0.006$, $\kappa = 0.010$, and $\kappa = 0.014$. The first column is the time domain waveform results. The second column is the power spectrum corresponding to the time domain. The third column shows the attractors in phase space. For small optical feedback strength $\kappa = 0.003$, the SL output power is constant as shown in Figure 2.9(a-i). For the external feedback strength of $\kappa = 0.006$. SL becomes unstable and exhibits a P1 oscillation as shown in Figure 2.9(b-i). The main frequency of the oscillation is $1.25GHz$ which is very close to the relaxation oscillation frequency at the solitary mode. With the feedback strength raised at $\kappa = 0.010$, a QP oscillation appears as shown in Figure 2.9(c-i). Figure 2.9(d-i) shows a chaotic oscillation at $\kappa = 0.014$. When the laser output power shows periodic oscillation, clear spectral peaks can be observed, however, in the chaotic state, clear spectral peaks are not observable but the spectrum is broadened around the relaxation oscillation frequency, as shown in Figure 2.9(d-ii).

2.2. Instability Behavior in Semiconductor Laser Dynamics

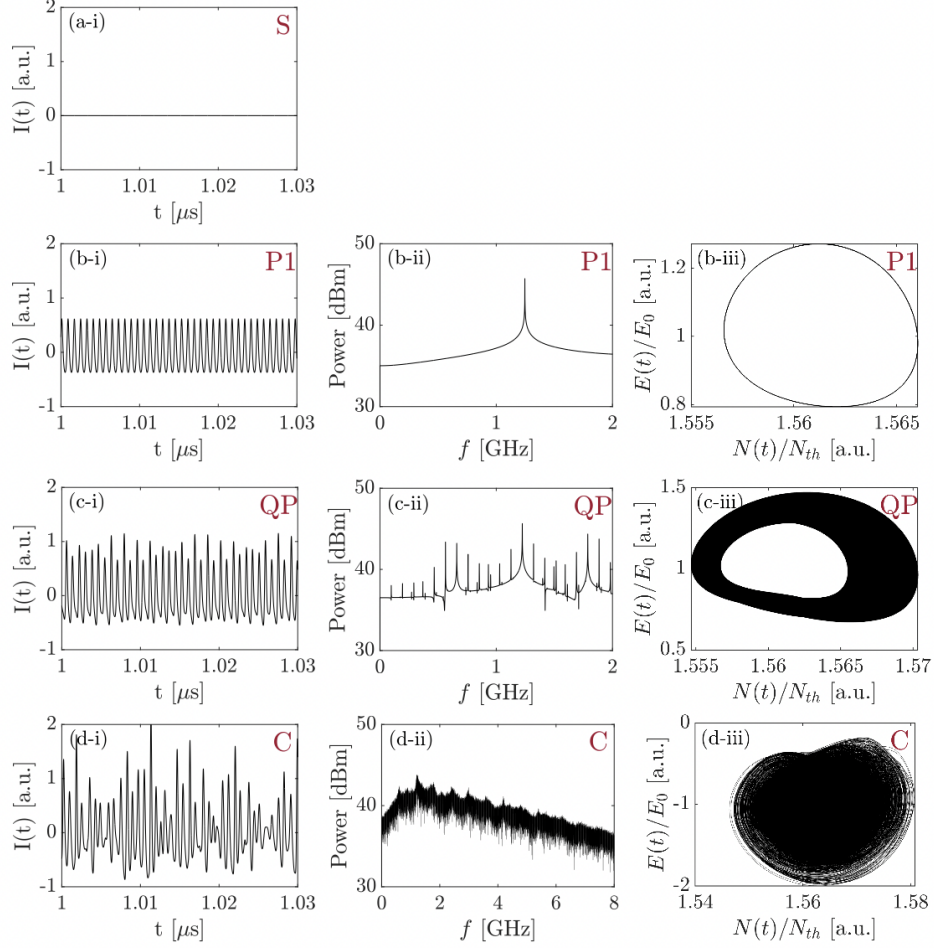


Figure 2.9: (a) S: steady state, and $\kappa = 0.003$. (b) P1: period-one state, and $\kappa = 0.006$. (c) QP: quasi-period state, and $\kappa = 0.010$. (d) C: chaos state, and $\kappa = 0.014$. (i) Waveform diagrams for different states. (ii) Power spectrum diagrams. (iii) Phase space diagrams.

The attractor is a trajectory in the phase space of the system variables and is frequently used for the analysis of chaotic oscillation [68]. When the SL output power at a stable oscillation is constant, the attractor becomes a fixed point in the phase space of the photon number (laser intensity) and the carrier density. For a P1 signal, the attractor forms a circle (referred to as a limit-cycle attractor) as shown in Figure 2.9(b-iii). However, the chaotic attractor behaves in a rather different way from fixed state or periodic oscillation. In chaotic oscillation, the trajectory goes around thick circles within the closed compact space, as shown in Figure 2.9(d-iii). The chaotic

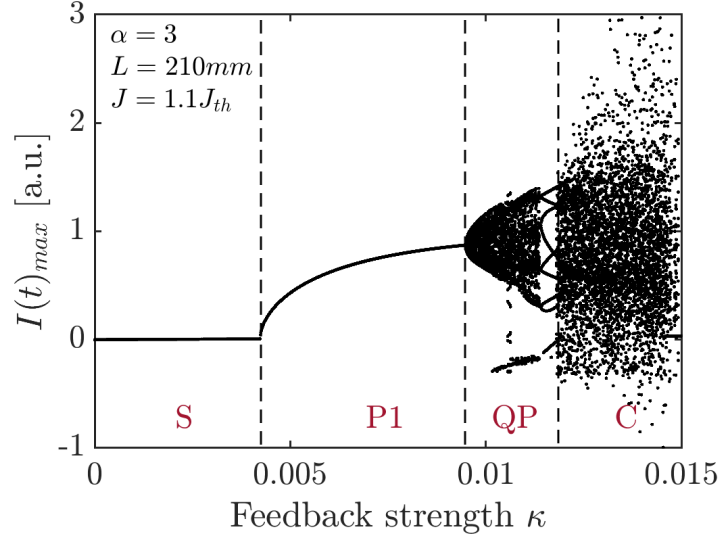


Figure 2.10: Bifurcation diagram when $\alpha = 3$, $L = 210mm$, and $J = 1.1J_{th}$. S: steady state; P1: period-one state; QP: quasi-period state; C: chaos state.

attractor of Figure 2.9(d-iii) is quite different from other periodic attractors and is referred to as a strange attractor. In fact, the chaotic trajectory goes around in a multidimensional space and never crosses in phase space.

Figure 2.10 shows the bifurcation diagram of the logistic map when κ is changed continuously from 0 to 0.015 with a step of $\Delta\kappa = 0.0001$, other parameters remain unchanged. The different dynamic states are separated by the dotted lines. From Figure 2.9 and Figure 2.10, it can be seen that SL with OF exhibits rich nonlinear dynamics, different states have different waveforms and characteristics. The properties of an SL can be significantly affected by OF. Make full use of the nonlinear dynamic characteristics of the laser, with the change of SL associated parameters, an SL may operate at different dynamical states.

In recent decades, various applications have been reported in different states. In steady state, an SL with OF can be utilized to detect the Doppler shift, vibration, velocity measurement, and displacement measurement [52, 55, 58, 63, 72]. In P1 state, a large sideband-rejection-ratio is obtained, with this unique advantage, P1 oscilla-

tion can be used to generate photonic microwaves and fiber-optic radio communication [8, 18, 37, 73]. In quasi-period state, SL with the influence from OF will generate subwavelength, by monitoring frequency shift can achieve multidimensional 2D measurement [74]. In chaos state, due to the broad bandwidth of chaotic oscillation and pseudo-randomness, it can be implemented in chaotic radar and chaotic secure communication [70, 75–77], et al.

In optical nonlinear dynamics, another important physical parameter is relaxation oscillation. The relaxation oscillation of laser intensity output is one of the important characteristics to determine the frequency range of the temporal dynamics of lasers. Figure 2.11 shows an example of relaxation oscillation of the laser intensity when the laser is turned on [67]. From Figure 2.11, it can be seen that the output of a continuously pumped laser consists of a series of tiny damped oscillation at the beginning time, and then gradually enter the steady-state output. This oscillation takes place with a period that is considerably longer than the photon lifetime in the class B laser. With the change of system parameters or increased external disturbance, there will be an undamped relaxation oscillation phenomenon that happened [78, 79]. The basic physical mechanism is the interplay between the laser intensity in the cavity and the population inversion. An increase in the laser intensity causes a reduction in the population inversion due to the increased rate of stimulated emission. This causes a reduction in the gain that tends to decrease the laser intensity. Then, the population inversion starts to increase again and the laser intensity follows the growth of the population inversion afterward. This oscillatory behavior between the laser intensity and the population inversion continues for several or tens of cycles and relaxes into stable values of the laser intensity and population inversion. Thus, this phenomenon is called relaxation oscillation.

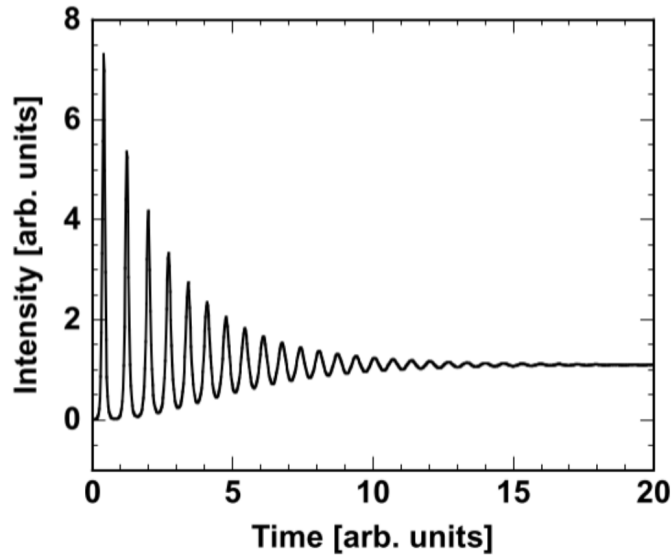


Figure 2.11: Temporal waveform of the relaxation oscillation of the laser intensity when the laser is turned on.

It is found that the relaxation oscillation frequency (f_R) in SLs is very fast at around a few GHz due to the short population and photon lifetimes, whereas the relaxation oscillation frequency in solid-state and gas lasers ranges from kHz to MHz . The relaxation oscillation in the intensity of laser output is usually observed just after the laser is turned on and approaches a steady-state operation. However, perturbations in the pumping power can also cause relaxation oscillation to appear spontaneously. The relaxation time is relatively larger than the oscillation time, which makes relaxation oscillation evident on the oscilloscope trace of the laser output intensity.

2.2.2 Determine boundary between stability and instability

The stability of a system is usually analyzed based on the system determinant. For an SL with OF, its system determinant is obtained based on analysis of the L-K equations near the stationary solutions [50, 80–82] described by:

2.2. Instability Behavior in Semiconductor Laser Dynamics

$$\omega_s \tau = \omega_0 \tau - \frac{\kappa}{\tau_{in}} \tau \sqrt{1 + \alpha^2} \sin(\omega_s \tau + \arctan \alpha) \quad (2.20)$$

$$N_s = N_0 + \frac{1/\tau_p - 2(\kappa/\tau_{in}) \cos(\phi_s)}{G_N(1 - \varepsilon \Gamma E_s^2)} \quad (2.21)$$

$$E_s^2 = \frac{J/(eV) - N_s/\tau_s}{1/\tau_p + 2(\kappa/\tau_{in}) \cos(\phi_s)} \quad (2.22)$$

Where E_s , N_s and ω_s represent the stationary solutions of L-K equations without ignoring the nonlinear gain for electric field amplitude, carrier density and angular frequency respectively. Note that, if ignoring the nonlinear term associated with $E(t)$ in Equation (2.13), i.e., $\varepsilon = 0$ the above stationary solutions are same as the ones used in [51, 81], that is Equation (2.14)-Equation (2.16).

Assuming that $E(t)$, $\omega(t)$ and $N(t)$ exhibit small deviations from above stationary solutions [denoted by $\delta_E(t)$, $\delta_\phi(t)$ and $\delta_N(t)$ respectively], the following linear differential equations can be obtained from the L-K Equations (2.11)-Equation (2.13) in matrix form:

$$\begin{bmatrix} \frac{d\delta_E(t)}{dt} \\ \frac{d\delta_\phi(t)}{dt} \\ \frac{d\delta_N(t)}{dt} \end{bmatrix} = A \begin{bmatrix} \delta_E(t) \\ \delta_\phi(t) \\ \delta_N(t) \end{bmatrix} + B \begin{bmatrix} \delta_E(t - \tau) \\ \delta_\phi(t - \tau) \\ 0 \end{bmatrix} \quad (2.23)$$

Where,

$$A = \begin{pmatrix} -\frac{\kappa}{\tau_{in}} \cos(\phi_s) - \varepsilon \Gamma G_N(N_s - N_0)E_s^2 & -\frac{\kappa}{\tau_{in}} \sin(\phi_s)E_s & \frac{1}{2}G_N(1 - \varepsilon \Gamma E_s^2)E_s \\ \frac{\kappa}{\tau_{in}E_s} \sin(\phi_s) - \alpha \varepsilon \Gamma G_N(N_s - N_0)E_s & -\frac{\kappa}{\tau_{in}} \cos(\phi_s) & \frac{1}{2}\alpha G_N(1 - \varepsilon \Gamma E_s^2) \\ -2G_N(N_s - N_0)E_s(1 - 2\varepsilon \Gamma E_s^2) & 0 & -\frac{1}{\tau_s} - G_N(1 - \varepsilon \Gamma E_s^2)E_s^2 \end{pmatrix} \quad (2.24)$$

$$B = \begin{pmatrix} \frac{\kappa}{\tau_{in}} \cos(\phi_s) & \frac{\kappa}{\tau_{in}} \sin(\phi_s) E_s & 0 \\ -\frac{\kappa}{\tau_{in} E_s} \sin(\phi_s) & \frac{\kappa}{\tau_{in}} \cos(\phi_s) & 0 \\ 0 & 0 & 0 \end{pmatrix} \quad (2.25)$$

The system determinant [denoted by $D(s)$] of Equation (2.23) is derived as:

$$D(s) = \det(sI - A - e^{-s\tau} B) = s^3 + X + Y + Z \quad (2.26)$$

Where, X, Y, Z are:

$$\begin{cases} X = s^2 \left[2 \frac{\kappa}{\tau_{in}} \cos(\phi_s) (1 - e^{-s\tau}) + \omega_{R1} + \frac{1}{\tau_R} \right] \\ Y = s \left\{ \left(\frac{\kappa}{\tau_{in}} \right)^2 (1 - e^{-s\tau})^2 + \frac{\kappa}{\tau_{in}} \left[\left(\frac{2}{\tau_R} + \omega_{R1} \right) \cos(\phi_s) - \alpha \omega_{R1} \sin(\phi_s) \right] (1 - e^{-s\tau}) + \frac{1}{\tau_R} \omega_{R1} + \omega_{R2}^2 \right\} \\ Z = \frac{1}{\tau_R} \left(\frac{\kappa}{\tau_{in}} \right)^2 (1 - e^{-s\tau})^2 + \frac{\kappa}{\tau_{in}} \left(\frac{1}{\tau_R} \omega_{R1} + \omega_{R2}^2 \right) [\cos(\phi_s) - \alpha \sin(\phi_s)] (1 - e^{-s\tau}) \end{cases} \quad (2.27)$$

Where τ_R is the damping time of the relaxation oscillation of an SL with OF, $\tau_R^{-1} = \tau_s^{-1} + G_N E_s^2 (1 - \varepsilon \Gamma E_s^2)$, $\omega_{R1} = \omega_R^2 \varepsilon \Gamma / [G_N (1 - \varepsilon \Gamma E_s^2)]$, $\omega_{R2}^2 = \omega_R^2 (1 - 2\varepsilon \Gamma E_s^2)$ and $\omega_R^2 = G_N E_s^2 G(N_s, E_s)$, where ω_R is the relaxation resonance angular frequency of an SL with OF.

Note that, ignoring the nonlinear gain ($\varepsilon = 0$) through stability analysis with the steady-state values, the characteristic equation $D(s) = 0$ should be derived [81]. Due to it is the fixed $D(s) = 0$ with $s = 0$, which does not effect the stability. Hence, for the case that the solution of $D(s) = 0$ with $s = j\Omega$, and $\Omega/2\pi$ being the base-band frequency, the condition of imaginary part for the stability is given by [66, 79, 81], and for all values of Ω satisfying Equation (2.28), where, $\tau_R^{-1} = \tau_s^{-1} + G_N E_s^2$ and $\omega_{R0}^2 = G_N E_s^2 / \tau_p$, where ω_{R0} is the relaxation resonance angular frequency of an SL without OF, according Equation (2.21), $N_s = N_0 + \frac{1/\tau_p}{G_N}$, therefore, $G(N_s, E_s) = 1/\tau_p$ with $\kappa = 0$ and $\varepsilon = 0$.

$$\Omega^2 - \omega_{R0}^2 = \frac{\Omega}{\tau_R} \cot\left(\frac{\Omega\tau}{2}\right) \quad (2.28)$$

$$f_R = \frac{1}{2\pi} \sqrt{\frac{G_N E_s^2}{\tau_p}} \sqrt{\frac{[1 - 2\frac{\kappa}{\tau_{in}}\tau_p \cos(\omega_s\tau)][1 + \frac{\kappa}{\tau_{in}}\tau \cos(\omega_s\tau) - \alpha\frac{\kappa}{\tau_{in}}\tau \sin(\omega_s\tau)]}{1 + (\frac{\kappa}{\tau_{in}})^2\tau^2 + 2\frac{\kappa}{\tau_{in}}\tau \cos(\omega_s\tau)}}} \quad (2.29)$$

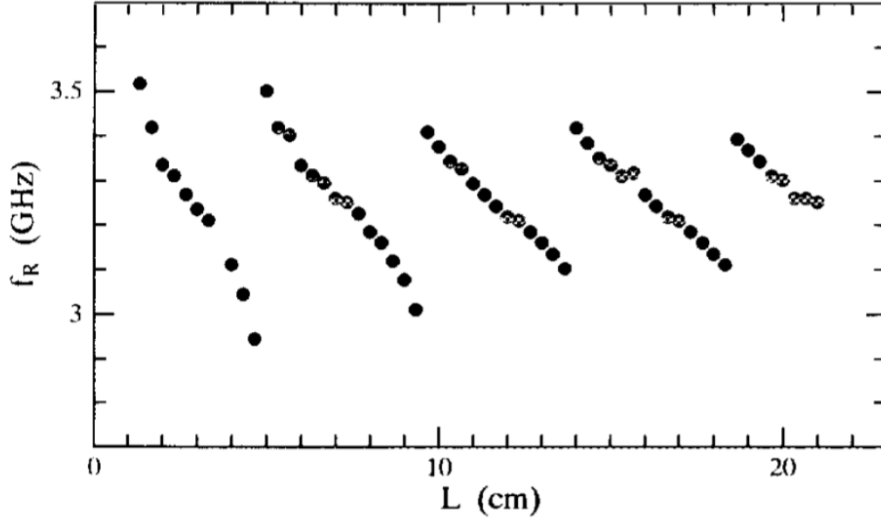


Figure 2.12: Relaxation oscillation frequency as a function of the external cavity length.

Equation (2.28) unveils the existence of excited periodic oscillation with a frequency $(\Omega/2\pi)$ strongly dependent on the external cavity round-trip time and varying periodically around the free-running angular ω_{R0} , which gives an expression for τ as a function of Ω [81]. And $\omega_{R0} = 2\pi f_{R0}$, where the relaxation oscillation frequency of solitary laser is $f_{R0} = \frac{1}{2\pi} \sqrt{\frac{G_N E_s^2}{\tau_p}}$, besides, the relaxation oscillation frequency f_R in an SL with OF is described as Equation (2.29) [68], under the OF condition, f_R is equal to excited frequency $\Omega/2\pi$. In 1998, as shown in Figure 2.12, the relationship between the relaxation oscillation frequency f_R (strictly speaking, it is excited frequency $\Omega/2\pi$ near the relaxation oscillation frequency f_{R0}) and the external cavity

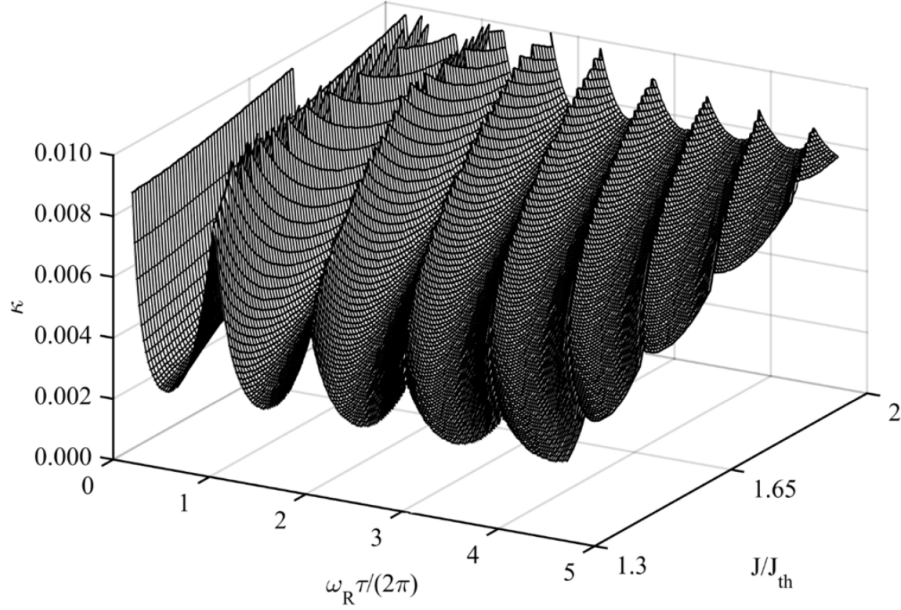


Figure 2.13: Stability boundary described in the 3-parameter space of (κ, τ, J) , where $\tau = 2L/c$. The unstable region is above the surface.

length L has been experimentally confirmed in a range of 30cm in Ref. [79], this periodic relationship between f_R and L shows that relaxation oscillation frequency carries information associated with the external cavity, thus has potential use for sensing and instrumentation. Additionally, in Ref. [83], the stability boundary is investigated and described in the 3-parameter space of (κ, τ, J) , where $\tau = 2L/c$, as shown in Figure 2.13, according the system determinant $D(s) = 0$ of Equation 2.26. It reveals stability boundary is a surface with periodical fluctuations, the area above the surface is the unstable region.

2.3 Photonic Microwave Signals Generation

2.3.1 Microwave generation technologies

Microwave frequencies are usually generated by electronic circuits that have multiple frequency multiplications to achieve the desired frequency. The system is complicated

and expensive. In addition, for many applications, the generated microwave signals must be transmitted to distributed remote sites. Due to the high losses associated with electrical transmission lines such as coaxial cables, wired distribution of microwave signals in the electrical domain is impractical. The wireless distribution of microwave signals is ideal for short distances, not long distances, because the propagation loss of microwaves increases with frequency. The generation of microwave signals through photonics has aroused extensive research interest due to its advantages of high speed, low power consumption, low cost and high reliability. Microwave photonic (MWP) signals can be effectively transmitted and widely distributed through low-loss, long-distance optical means, thereby circumventing the limitation of microwave distribution [84]. In this section, the main MWP generation technologies will be analyzed and discussed.

By using high-frequency electronic components, many MWP generation methods can produce very low phase noise. These commonly used techniques can be summarized as direct modulation, external modulation, optical heterodyne technology used in conjunction with optical phase-locked loops (OPLL), mode-locked semiconductor lasers, period-one (P1) dynamics, and optoelectronic oscillators (OEO). The expansion of technologies that rely on electronic resources is as follows:

A1. Direct modulation

The most direct method is to use an electronic microwave source to directly modulate the semiconductor laser. The disadvantage of using this technique is that the modulation bandwidth is limited by the inherent resonance frequency of the laser and the availability of high-frequency electronic microwave sources. And the modulation depth is also relatively low. Using optical injection locking can slightly increase this limit [20, 85, 86].

A2. External modulation

Using an external modulator to modulate the laser optical output. These approaches introduced the electro-optic materials such as lithium niobate [87], polymers [88, 89], and the semiconductors [90]. MWP signal generation utilizing external modulation can attain very high frequency and low phase noise microwave signals, but there is a drawback resulting from the insertion loss of the modulators.

A3. Optical heterodyne

The optical heterodyne technique can easily achieve terahertz photonic microwaves by beating between two optical beams with certain wavelength spacing, and by hybridizing two optical components with different frequencies on the detector, such the technique has very wide tunability [22]. However, the inevitable mismatch of optical phases and fluctuated amplitudes between two noncoherent lasers results in extremely poor microwave stability, which becomes an Achilles' heel for applications requiring high stability [91]. In order to further stabilize the signal, the optical phase difference between the two optical components is tracked by using a reference frequency from a stable electronic microwave source to compare the output signal of the detector [92]. By further introducing sideband injection locking, frequency stability can be improved [23, 93].

The above-mentioned technologies are the technologies that rely on high-frequency electronic equipment, and these technologies are expensive and complicated to implement. Therefore, some MWP generations that do not rely on high-frequency electronic components have also been studied. These methods are briefly described as follows:

B1. Self-pulsating laser

By exciting the relaxation resonance in a two-section laser, through the interaction between the two parts, self-pulsing can be excited, and the frequency is usually limited to a few gigahertz [25, 94].

B2. Dual-wavelength laser

In a dual-wavelength laser, the two optical components are generated in the same optical cavity. Therefore, the stable microwave frequencies can be obtained by the intrinsic relation of common noise. To achieve the dual-wavelength operation, the proper seeding from independent lasers [26] or by incorporating gratings for mode-selection in fiber ring lasers can be used [95, 96].

B3. Optoelectronic oscillator

The optoelectronic oscillator (OEO) can use a very long optical fiber loop to generate a very stable microwave signal, while multiple loops can be used to suppress parasitic noise [97, 98]. The disadvantage of using OEO is that the construction requires high frequency components such as microwave filters, microwave amplifiers, photodetectors, and optical modulators. The tunability is limited by these electronics' bandwidth. Some of these electronic components can be replaced by optical components, however, by doing so, the complexity of the implementation is also increased [27, 99–101].

B4. Passively mode-locked laser

Utilizing passively mode-locked laser can produce monolithic photonic microwave generation with frequency over $100GHz$. The microwave linewidth is typically less than $1MHz$ by using this method, [30, 102]. The limitation of this method is that the tunability is usually controlled by the fixed cavity length. Besides, the system is complex, costly, and the frequency of the microwave signal is difficult to adjust [28].

B5. Period-one dynamics

One of the prominent techniques is based on P1 nonlinear dynamics. Through optical feedback or optical injection, the laser can be driven to a periodic oscillation state, especially P1 oscillation. The laser emission intensity oscillates at the microwave frequency. The rich advantages and diversity of P1 dynamics are detailed in the following section. Although the microwave photon signal generation based on P1 oscillation has

2.3. Photonic Microwave Signals Generation

Table 2.2: Comparison of MWP Generation Techniques.

| | Electronics | Tunability | Maximum Frequency | Microwave Linewidth | Single Sideband | Modulation Type | Stability | Optical Loss |
|---------------------|-------------|------------|-------------------|----------------------|-------------------------|-----------------|-----------|--------------|
| Direct Modulation | Moderate | Fair | 30 GHz | Determined by source | Special design required | AM | Good | None |
| Optical Heterodyne | Simple | Good | ~THz | Broad | Yes | None | Poor | None |
| OPLL | Complicated | Fair | 330 GHz | Narrow (~mHz) | Yes | None | Good | None |
| Dual-mode Laser | Complicated | Good | 42 GHz | Moderate (~MHz) | Yes | None | Poor | None |
| External Modulation | Moderate | Fair | 40 GHz | Determined by source | Special design required | AM/PM | Good | Large |
| Mode Locking | Moderate | Poor | 30 GHz | Narrow (~Hz-mHz) | No | None | Good | Large |
| OEO | Complicated | Poor | 75 GHz | Narrow (~mHz) | No | AM/PM | Good | Large |
| P1 Dynamics | Simple | Good | 100 GHz | Moderate (~MHz-mHz) | Yes | FM | Poor | None |

many advantages, it is not without disadvantages. Due to the spontaneous emission, the inherent phase noise in the nonlinear P1 oscillation can impair its application. For example, phase noise will reduce the signal-to-noise ratio in communications [44]. Phase noise also increases the linewidth of the generated microwaves, which affects the performance of radio over optical fiber (RoF) applications and the maximum detection range of the Doppler velocimeter [35, 103].

Additionally, the MWP generation techniques mentioned above are listed systematically in Table 2.2 from the review work in Ref. [84].

2.3.2 Period-one oscillation technology

It can be seen from Table 2.2 that the advantages of microwave generation based on P1 oscillation are very prominent. Including simple structure, good tunability, nearly single sideband, and almost none optical loss. Recently, the use of MWP generated by nonlinear dynamic P1 oscillation has been studied for microwave generation [18, 33, 37, 39, 40, 42, 104–106].

In P1 dynamics by using external OF, the P1 oscillation is one of the many nonlinear dynamics such as period-doubled, quasi-periodic, and chaotic oscillation under external optical disturbance to the SL. P1 oscillation can be achieved when a stable locked laser experiences a Hopf-bifurcation, which the intensity of the laser emission is oscillating at a microwave frequency [7, 38, 39]. The OF scheme includes two character-

istic time scales for controlling dynamics, namely the laser relaxation oscillation time and the external cavity round-trip time. The former characterizes the energy exchange rate between carriers and photons, thereby adjusting the oscillation frequency of P1 dynamics. The latter corresponds to external cavity modes, which could be helpful to stabilize P1 dynamics. Once P1 frequency components are locked to these modes, the phase noise originating from intrinsic spontaneous emission will be effectively suppressed [7, 34, 69, 107, 108]. Then, by reducing the microwave linewidth to much smaller than the linewidth of the free-running laser, the corresponding P1 oscillation can be stabilized. However, other external cavity modes that are not occupied by the P1 frequency are usually represented by residual noise peaks near the P1 microwave frequency, which will damage the stability [35, 36, 107]. In P1 dynamics by using optical injection, there are two dominant frequencies: one is generated from the optical injection while the other one is emitted near the cavity resonance frequency [104]. The frequency of photonic microwave generation based on P1 can be broadly tunable by changing the injection power or frequency detuning. The generated frequency can far exceed the relaxation oscillation frequency of the injected semiconductor laser. Photonic microwave generation based on P1 oscillation has been investigated extensively in conventional single-mode distributed feedback (DFB) laser [39, 41]. The results show that 100GHz with a tuning range of tens of gigahertz photonic microwave signal can be achieved using P1 oscillation in DFB lasers [109]. Recently, a tunable photonic microwave with the continuous tuning of the frequency up to 20GHz has also been achieved experimentally in a quantum dot laser based on P1 oscillation [110].

For photonic microwave generation, the nonlinear dynamical P1 oscillation offers the following advantages over other techniques. Firstly, The microwave frequency generated from P1 oscillation by optical injection method is broadly tunable, and it is far beyond the laser's relaxation resonance frequency, in some DFB lasers, the

generated frequency can even be up to terahertz band [40,41]. Secondly, the microwave frequency of P1 oscillation generated by the OF method has the advantages of narrow linewidth and easy to produce stable P1 state. Thirdly, the generation of the optical microwave signal can be achieved without using any electronic microwave components [42,84]. Fourthly, on optical spectra, single-sideband can be generated by adjusting the injection parameters to minimize the chromatic dispersion introduced microwave power penalty during the transmission over long optical fibers [8,43,73,111]. Fifthly, maximal microwave power at a constant average optical power can be produced because of nearly 100% intensity modulation depth [43,44]. Sixthly, The bias current of the laser can be modulated electrically or optically at the same time to modulate the microwave signal [44,112].

Due to the listed advantages above, the P1 oscillation is implemented into a number of applications such as radio-over-fiber (RoF) [44], clock frequency division [113,114], modulation formation conversion [109,111], uplink transmission [73,112], long-detection-range Doppler velocimeter [109], and photonic microwave amplification [43]. Despite many of the advantages, the P1 oscillation is not without its limitations. The P1 oscillation dynamics characteristically contains phase noise due to the fluctuations in the lasers. This phase noise causes performance issues in many applications: in communication links, the reduction of signal-to-noise ratio [83], reduction on the maximal detection range in Doppler velocimeters [100], and the degradations of the noise performance in photonic microwave amplification [93]. Thus, there are some techniques developed to reduce the phase noise. In DFB lasers, locking the P1 oscillation using a stable electronic microwave source were introduced in the year 1999, the which the generated microwave signal frequency is up to $17GHz$ and its linewidth is below $1kHz$ [101]. Self-injection locking using optoelectronic feedback also narrowed the microwave signal linewidth to about $10kHz$ [56], however, this approach requires

2.3. Photonic Microwave Signals Generation

high-speed microwave amplifiers for the electric feedback. Polarization rotated feedback with optoelectronic feedback was also reported, it reduced the linewidth to about $3kHz$ for a P1 oscillation generated microwave at $6GHz$ [87], the imperfection of this method is that the tunability is restricted by the electronic circuitries.

To address these limitations, a promising OF scheme has been applied to overcome the above bottlenecks [102, 115]. The OF scheme was introduced to generate narrow microwave linewidth, which, provides comparable linewidth reduction without adding extra electrical components and has no restrictions on the tunability, in addition, since the feedback laser of the OF scheme is phase-locked to the original laser, the frequency of the microwave signal obtained by the OF scheme is more stable. In the following chapters, we describe, develop and test the SL with OF system. Based on rich nonlinear SL dynamics, it focuses on the capability of sensing applications, including displacement measurement and absolute distance measurement with both high performances. A field-wide investigation and research on OF effects in SLs for sensing applications is completed, and shows that photonic microwave sensing based on inherent SL dynamics is envisioned to be a promising alternative to conventional pure electronic or optical solutions.

Chapter 3

New Approach for Period-one Photonic Microwave and Its Displacement Measurement

3.1 Chapter Introduction

Semiconductor laser (SL) attracts much attention from researchers due to its small size, low cost in manufacturing, and operate at low power consumption. It has been found that external optical feedback (OF) can significantly affect the properties and behaviors of an SL [50,116]. Regarding the OF effect in an SL, on one hand, researchers try to avoid or eliminate the influence of OF on an SL. On the other hand, researchers actively make full use of OF for sensing and instrumentation. For example, utilizing SL with OF contributes to the discovery of a new class of laser interferometry which is named as self-mixing interferometry (SMI) or optical feedback interferometry (OFI) [49]. The principle of such interferometer and the physical process is that, when a portion of the light is back-scattered or back-reflected by an external target and re-enter the SL internal cavity, both laser intensity and its frequency can be altered

by the movement information associated with the target. The schematic structure of a typical SL with OF displacement sensing system is depicted in Figure 3.1, it mainly includes three parts, laser source, signal detection system, and measurement target. The core components consist of an SL, an external photodetector (PD), and an external target. In fact, SLs are inherently nonlinear devices [117], in nonlinear systems, the folding and stretching behaviors of variables result in different dynamical routes [118]. Under the different operational conditions, the SL undergoes from steady (S) state, period-one (P1) oscillation, quasi-period (QP) oscillation to chaos (C) [68]. Various potential applications have been investigated and reported in different dynamic states. In steady state, an SL with OF can be utilized to detect the Doppler shift, vibration, velocity measurement, and displacement [46, 116, 119, 120]. In P1 state, the optical injection and optical feedback schemes were used to generate microwave [117, 121, 122]. In Ref. [121], a periodic switching between two nonlinear dynamic states caused by optical feedback is demonstrated. By adjusting the feedback strength, the duty cycle of the periodic state can be adjusted, thereby a tunable method for generating microwave photonic (MWP) signal is proposed. In Ref. [122], a method of generating reconfigurable radar waveform based on optical injection is presented. In this method, a low-speed control signal is used to adjust the injection strength so that to control the output microwave frequency. The Ref. [122] experimentally proved that the proposed microwave generator can be used for radar applications. Other applications for MWP include MWP processing, sensing, and fiber-optic radio communication [8, 73, 84, 123–125]. In quasi-period state, SL with the influence from OF will generate subwavelength, by monitoring frequency shift can achieve multi-dimensional 2D measurement [74]. In chaos state, due to the broad bandwidth and pseudo-randomness of chaotic oscillation, it can be implemented in chaotic radar and chaotic secure communication [77, 126] et al.

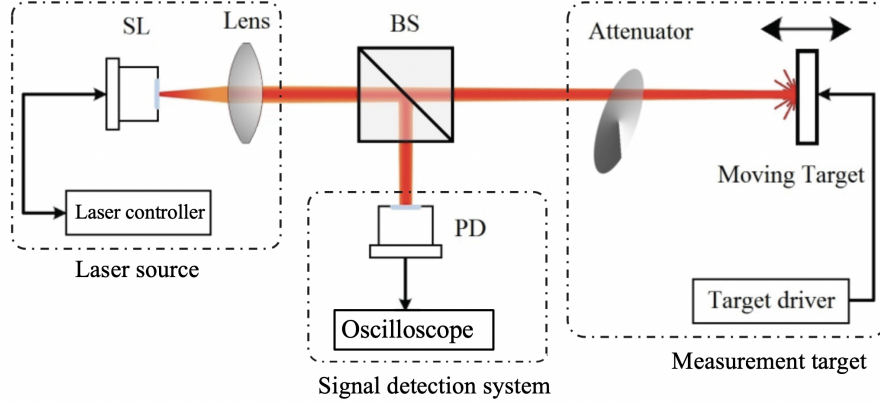


Figure 3.1: Schematic structure of an SL with OF system for displacement sensing. SL: semiconductor laser; BS: beam splitter; PD: photodetector.

An SL with OF sensing system operates at steady state (that is SMI) can provide a displacement measurement resolution with half laser wavelength ($\lambda_0/2$). For further improving the sensing resolution, one group of researchers make use of SMI sensing model to retrieve displacement from an SMI waveform [55, 62]. Theoretically, this method can achieve super high resolution. However, due to inevitable intensity noise and inaccurate model parameters, the resolution is still very limited, e.g., the work in Ref. [62] declared that $40nm$ resolution can be achieved experimentally. Another group of researchers modulate the SL injection current or external cavity to have the displacement to be carried in the phase of an SMI signal, e.g., the work in Ref. [60] achieves a resolution of $15nm$ in experiment by retrieving the initial phase using fast Fourier transform (FFT). It requires a target to be measured must be in a low speed relative to the modulation period and the measurement range is about $1\mu m$. The work in Ref. [127] added extra physical components and combined the high sensitivity of a frequency-shifted feedback laser with the axial positioning capability of a confocal microscope, it reached $2nm$ resolution with about $10\mu m$ measurement range. The work in Ref. [128] proposes to set the SL in an SMI sensing system operating at P1 state to generate MWP signal for sensing. This can provide a resolution of $\lambda_0/1280$

theoretically. And the work in Ref. [129], an SL with dual-cavity OF operating at P1 state was proposed to deal with the target has a low reflectivity by utilizing MWP signal. It demonstrated the measurement sensitivity can be boosted up to 268 times compared to a general SMI sensing. However, how to design an SL with OF system that can robustly working at P1 state to generate MWP signal and what is the applicable measurable range are not discussed in previous studies.

In this chapter, we propose to improve the sensing performance for an SL based MWP displacement sensing system, in terms of measurement resolution and measurement sensitivity. We first determine the P1 region boundaries for an SL with OF system and study the P1 boundaries characteristics. Then, we investigate how the system controllable parameters influence the P1 boundaries, from which a set of parameters selection rules are presented. The implementation of experimental system is also demonstrated. As an application example, an experimental displacement sensing system is investigated.

3.2 Principle of SL with OF System

3.2.1 Numerical study of SL with OF system

SL dynamics can be affected by external perturbations including OF, optical injection, current modulation, and optoelectronic feedback. By varying external perturbations, an SL can work at steady state, P1 oscillation, quasi-period (QP) oscillation, or chaos (C). The rich dynamics of SLs have been investigated and found their various potential applications in optical communications, defense and security, radar detection, etc [6, 130, 131]. These SL operation states have great potential to develop novel MWP techniques such as all-optical microwave frequency conversion [132] and single-sideband frequency modulation [133]. The dynamic of an SL with optical feedback can be

3.2. Principle of SL with OF System

theoretically characterized by the Lang-Kobayashi (L-K) rate equations [50]. In order to clearly show the derivation of solving the L-K equations, let's rewrite the L-K equations as follows:

$$\frac{dE(t)}{dt} = \frac{1}{2} \left\{ G[N(t), E(t)] - \frac{1}{\tau_p} \right\} E(t) + \frac{\kappa}{\tau_{in}} E(t - \tau) \cos[\omega_0 \tau + \phi(t) - \phi(t - \tau)] \quad (3.1)$$

$$\frac{d\phi(t)}{dt} = \frac{1}{2} \alpha \left\{ G[N(t), E(t)] - \frac{1}{\tau_p} \right\} - \frac{\kappa}{\tau_{in}} \frac{E(t - \tau)}{E(t)} \sin[\omega_0 \tau + \phi(t) - \phi(t - \tau)] \quad (3.2)$$

$$\frac{dN(t)}{dt} = \frac{J}{eV} - \frac{N(t)}{\tau_s} - G[N(t), E(t)] E^2(t) \quad (3.3)$$

In the above equations, three main variables are used for describing the behavior of an SL with optical feedback, which are the amplitude of the electric field $E(t)$, the phase of the electric field $\phi(t)$, and the carrier density $N(t)$. The SL operating conditions are mainly determined by the four controllable parameters: line-width enhancement factor (α), external cavity length (L), injection current density (J), and feedback strength (κ). The other parameters in the L-K equations are internal parameters associated with the SL, and their physical meanings are detailed in Table 2.1.

The L-K equations are ordinary differential equations, there are lots of numerical solutions for ordinary differential equations. To overcome this problem, in this thesis, the fourth-order Runge-Kutta method is used to solve the L-K equations [134, 135]. The Runge-Kutta method is a method of using the Taylor expansion of the function derivative to replace the derivative for the numerical solution of the differential equation. Consider the following system of differential equations, $dE/dt = f(t, E, \phi, N)$, $d\phi/dt = g(t, E, \phi, N)$, and $dN/dt = p(t, E, \phi, N)$, where $E(t_0) = E_0$, $\phi(t_0) = \phi_0$,

3.2. Principle of SL with OF System

and $N(t_0) = N_0$. Then, get the numerical solution in the interval of $a \leq t \leq b$. Substituting the first-order differential equations $dt = t_{k+1} - t_k$, $dE = E_{k+1} - E_k$, and $dN = N_{k+1} - N_k$ into system differential equations, then we can get the following Equations (3.4), where $k \in [0, 1, 2, \dots, M - 1]$.

$$\begin{cases} E_{k+1} - E_k = f(t_k, E_k, \phi_k, N_k)(t_{k+1} - t_k) \\ \phi_{k+1} - \phi_k = g(t_k, E_k, \phi_k, N_k)(t_{k+1} - t_k) \\ N_{k+1} - N_k = p(t_k, E_k, \phi_k, N_k)(t_{k+1} - t_k) \end{cases} \quad (3.4)$$

$$\begin{cases} t_{k+1} = t_k + h \\ E_{k+1} = E_k + hf(t_k, E_k, \phi_k, N_k) \\ \phi_{k+1} = \phi_k + hg(t_k, E_k, \phi_k, N_k) \\ N_{k+1} = N_k + hp(t_k, E_k, \phi_k, N_k) \end{cases} \quad (3.5)$$

Divide the interval $[a, b]$ into M subintervals, the width of each subinterval is $h = (b - a)/M$, the interval grid point satisfies $t_{k+1} = t_k + h$, and then substitute it into Equation (3.4), In this way, an iterative solution formula for the original differential equations in the interval $[a, b]$ can be obtained as Equation (3.5). This is the basic principle of the Runge-Kutta method to solve differential equations, that is, the differential equations are used to approximate the derivatives of the differential equations to be solved to obtain the differential equations, and then the solution interval is partitioned to obtain the subintervals of the differential iteration. Finally, the alternative equations are solved on each sub-division. Generally, in order to obtain higher calculation accuracy, it is necessary to use a higher order Taylor expansion to approximate the derivative, reduce the length of the iteration subinterval, and increase the number of iterations. The fourth-order Runge-Kutta method can simulate the accuracy of the fourth-order Taylor method, consequently, the calculation formulas and strategies for $E(t)$, $\phi(t)$, and $N(t)$ are shown in Equations (3.6)–Equations (3.8), thus,

the L-K equations can be numerically solved.

$$\begin{cases} E_{k+1} = E_k + h(f_1 + 2f_2 + 2f_3 + f_4)/6 \\ f_1 = f(t_k, E_k) \\ f_2 = f(t_k + h/2, E_k + hf_1/2) \\ f_3 = f(t_k + h/2, E_k + hf_2/2) \\ f_4 = f(t_k + h, E_k + hf_3) \end{cases} \quad (3.6)$$

$$\begin{cases} \phi_{k+1} = \phi_k + h(g_1 + 2g_2 + 2g_3 + g_4)/6 \\ g_1 = g(t_k, \phi_k) \\ g_2 = g(t_k + h/2, \phi_k + hg_1/2) \\ g_3 = g(t_k + h/2, \phi_k + hg_2/2) \\ g_4 = g(t_k + h, \phi_k + hg_3) \end{cases} \quad (3.7)$$

$$\begin{cases} N_{k+1} = N_k + h(p_1 + 2p_2 + 2p_3 + p_4)/6 \\ p_1 = p(t_k, N_k) \\ p_2 = p(t_k + h/2, N_k + hp_1/2) \\ p_3 = p(t_k + h/2, N_k + hp_2/2) \\ p_4 = p(t_k + h, N_k + hp_3) \end{cases} \quad (3.8)$$

3.2.2 MWP generation in P1 dynamics

As discussed above, by using the fourth-order Runge-Kutta method, $E(t)$, $\phi(t)$, and $N(t)$ can be solved. Focus on generating MWP signals in P1 state. A relative normalized laser intensity $I(t)$ is used to represent the MWP sensing signal, defined $I(t) = [E^2(t) - \overline{E^2(t)}]/E_0^2$, where $\overline{E^2(t)}$ is the mean of $E^2(t)$, and $E_0^2(t)$ is the laser intensity without OF. We set SL external controllable parameters are $J = 1.1J_{th}$, $\kappa = 2.5 \times 10^{-3}$, $L = 410mm$, and $\alpha = 6$, other parameters are adopted from Table 2.1. As an example, a typical MWP signal generated in the P1 state obtained from solving

3.2. Principle of SL with OF System

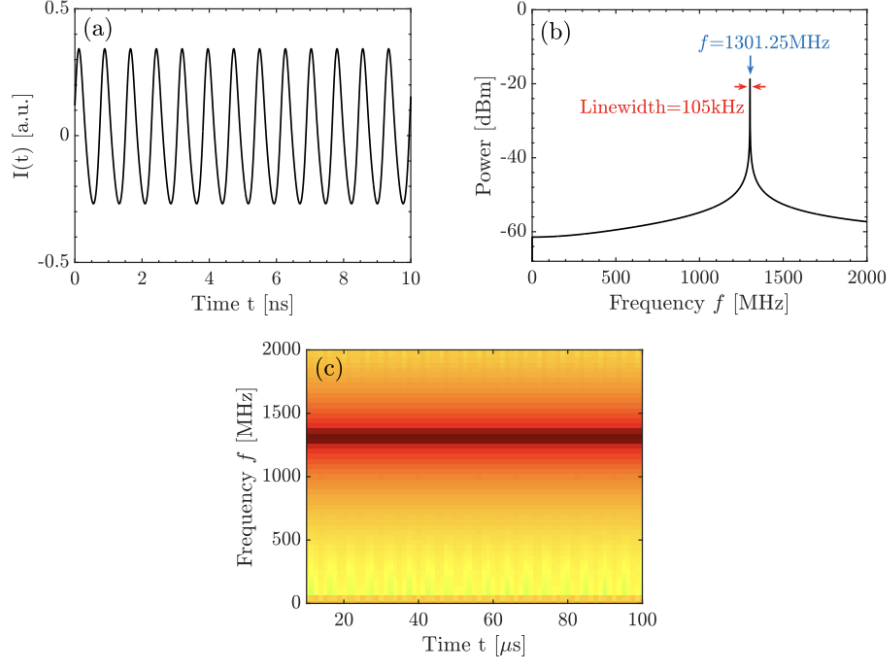


Figure 3.2: (a) Typical MWP signal generated from P1 state. (b) Corresponding FFT spectrum of typical MWP signal. (c) Corresponding STFT spectrogram of typical MWP signal.

L-K equations are shown in Figure 3.2(a), and the corresponding frequency-domain information of MWP signals are shown in Figure 3.2(b)-(c) via applying fast Fourier transform (FFT), and short-time Fourier transform (STFT) on time-domain signal, respectively. It can be seen that when the SL is accompanied by the external perturbation of optical feedback, the stable locked SL can enter the P1 dynamics by crossing the Hopf-bifurcation. The P1 state produces intensity-modulated light waves and produces regular pulsations at a microwave frequency at 1301.25 MHz , accompanied by a narrow frequency linewidth of 105 kHz . (Note: the frequency range of microwave is approximately between 300 MHz and 300 GHz). And the high frequency component shows high stability without any change over time.

Figure 3.3 presents the influence of the feedback strength κ on the frequency linewidth and frequency power of the generated microwave signals based on P1 oscillation in an SL with OF system. Other parameters are same as those in Figure

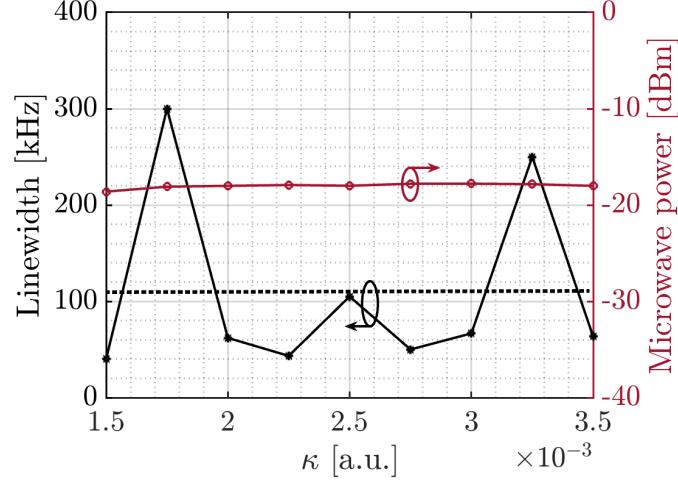


Figure 3.3: Frequency linewidth (black) and microwave power (red) as the function of the feedback strength κ .

3.2. The SL with OF system can operate at P1 region from $\kappa = 1.25 \times 10^{-3}$ to $\kappa = 3.57 \times 10^{-3}$, based on bifurcation analysis. Therefore, the relationship between feedback strength κ versus frequency linewidth and microwave power are investigated, by varying κ from $\kappa = 1.5 \times 10^{-3}$ to $\kappa = 3.5 \times 10^{-3}$ with a step size of 0.5×10^{-3} , for each κ , determining the frequency linewidth and microwave power from FFT of the temporal signals. The results show that within the whole P1 region, the fluctuation range of frequency linewidth is roughly from 30kHz to 300kHz , with a narrowly average frequency linewidth of 109kHz in dotted line. The reason for the frequency linewidth fluctuation may come from the effect of external feedback on the optical phase, resulting in the phase perturbation, which leads to the frequency linewidth fluctuation in P1 dynamics. The microwave power is also a key parameter used to evaluate the generated microwave signal. The power of the microwave signal here is defined as the peak power at the fundamental frequency in the power spectrum. The results show that the microwave power changes only slightly with the feedback strength increases, and basically stabilizes at a value of about -18dBm , until the P1 dynamic state is crossed. Figure 3.3 indicates that the MWP signals generated in the

3.2. Principle of SL with OF System

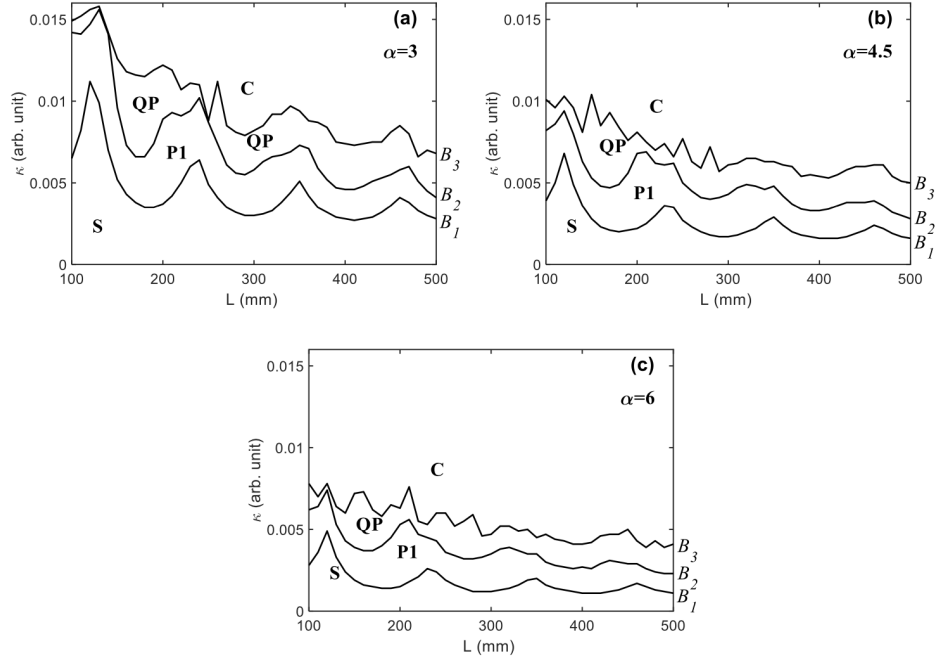


Figure 3.4: (a)-(c) show the influence of α on the state boundaries. S: steady state; P1: period-one state; QP: quasi-period state; C: chaos state; B_1 : boundary between S and P1; B_2 : boundary between P1 and QP; B_3 : boundary between QP and C.

entire P1 region all have a narrow linewidth and good microwave power stability.

An important figure for understanding the SL with OF system is the two parameters stability mapping of the dynamics as shown in Figure 3.4 and Figure 3.5, thereby, the different dynamic states can be recognized. We solved the L-K equations to get the laser intensity $I(t)$, from the waveforms of $I(t)$, the states can be determined. The states corresponding to different sets of an SL associated parameters are presented in the coordinate plane of (κ, L) and the state boundaries divide different state regions. In below simulations, we define the boundaries between S and P1 as B_1 , P1 and QP as B_2 , QP and C as B_3 , respectively.

In the following, the influence of system parameters on state boundaries are investigated to achieve a robust P1 state to generate MWP signal. Firstly, we set $J = 1.1J_{th}$, where J_{th} is the threshold of the injection current density, and set different values with $\alpha = 3, 4.5, 6$, respectively. By varying the L from 100mm to 500mm with a step of

3.2. Principle of SL with OF System

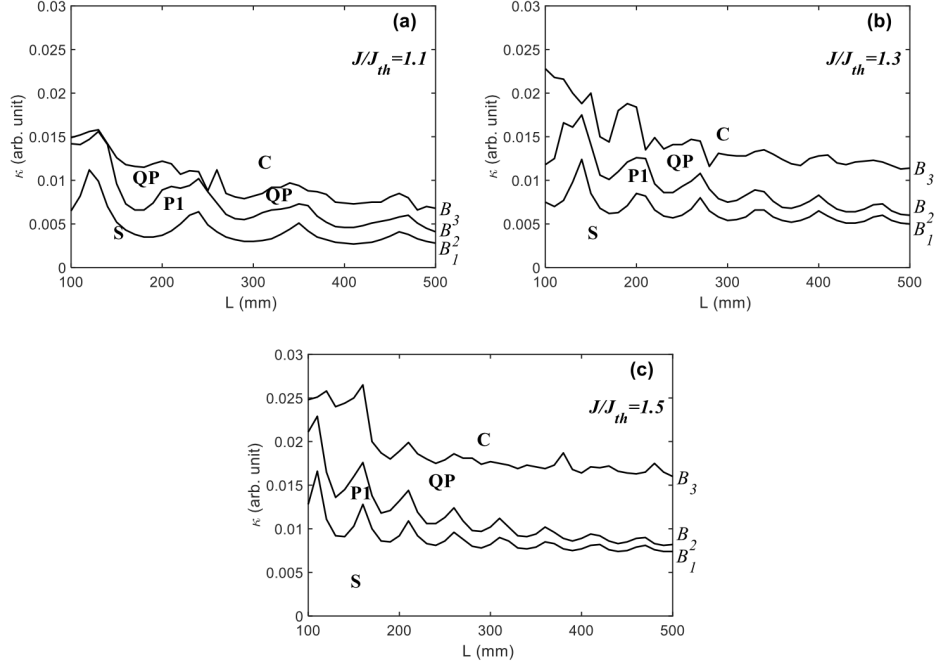


Figure 3.5: (a)-(c) show the influence of J on the state boundaries. S: steady state; P1: period-one state; QP: quasi-period state; C: chaos state; B_1 : boundary between S and P1; B_2 : boundary between P1 and QP; B_3 : boundary between QP and C.

10mm, for each L , gradually increase κ from 0 to 0.015 with step of 0.0001, to observe the waveform of $I(t)$ and record the corresponding state. The results are presented in Figure 3.4, it can be seen: For the S region, with L increases, the B_1 boundary shows a periodic enhancement feature with an slightly downward trend. With α increases, the S region size gradually decreases. For the P1 region, with L increases, it gradually narrows, and it also demonstrates a periodic enhancement feature. Furthermore, with α increases, P1 region becomes flattered with an unchanged period. For the C region, the increase of L or the increase of α will both cause the decrease of the B_3 boundary. In a similar way to investigate the influence from J . We set $\alpha = 3$ and $J/J_{th} = 1.1, 1.3, 1.5$, respectively. The results are shown in Figure 3.5. It can be observed: For S region, with J increases, the B_1 boundary indicates an upward trend. For the P1 region, with J increases, it also displays an upward trend and maintaining the periodic enhancement characteristic, however, the period of fluctuation becomes

decrease. For the C region, with J increases, the B_3 boundary presents a trend of upward. Based on the results of the this section, we can see that when we apply a low injection current density J and a large line-width enhancement factor α , the P1 region can be made wider, which is beneficial for the SL with OF system to work robustly in the P1 state.

3.3 Proposed New Method for Displacement Measurement

3.3.1 Determine P1 region and its influence parameters

As mentioned and discussed in previous chapters, the dynamic behaviors of an SL with OF can be described by the well-known Lang-Kobayashi (L-K) equations [50]. Through numerically solving above L-K equations, the laser intensity $E^2(t)$ can be obtained, $E^2(t)$ is also called sensing signal. The SL dynamic states can be identified by observing the waveform of $E^2(t)$. Under the proper external perturbations, the system can enter P1 dynamics through Hopf-bifurcation with undamped relaxation resonance of the SL [68]. To determine the P1 region and study its features, we present all the dynamic states of an SL in the coordinate plane of (κ, L) , each state on the (κ, L) plane is determined by both internal and external parameters of the SL. The internal parameters are fixed for a certain SL but the injection current (J) and line-width enhancement factor (α) may varies when designing a system. Thus, there is a need to study how these two parameters influence the P1 region, from which we can determine an optimal P1 region for sensing.

Firstly, we study the influence of injection current J on the P1 region. Fixing line-width enhancement factor with $\alpha = 3$, we set injection current with $J = 1.1J_{th}$, $J = 1.3J_{th}$, and $J = 1.5J_{th}$ respectively, where J_{th} is the threshold of the injection

3.3. Proposed New Method for Displacement Measurement

current. For each case, we vary the external cavity length L which travels from 0mm to 500mm with a step of $\Delta L = 5\text{mm}$. At each L , we increase feedback strength κ from 0 to 0.04 with step of $\Delta\kappa = 0.0001$ and finer when close to the state boundaries, then using L-K equations to generate $E^2(t)$ for every κ value. For each given set of parameters, we record the corresponding SL state on the (κ, L) plane. The SL states diagrams are obtained and shown in Figure 3.6, where the P1 region is the shaded area. It can be seen, the P1 region is a fluctuated band with an approximately modulation period denoted by D along L direction. At a suitable κ value, with the changes of L , the system switches between steady state and P1 state. This provides the possibility to implement a tunable optical microwave generator.

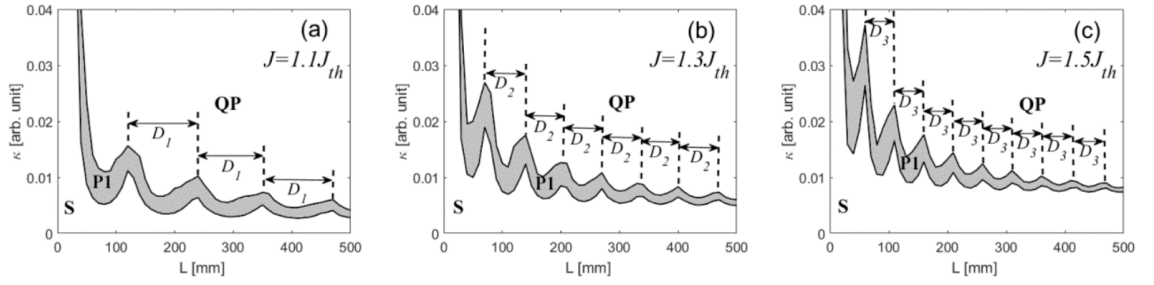


Figure 3.6: Influence of J on the P1 region with $\alpha = 3$. (a) $J = 1.1J_{th}$ and $D_1 = 120\text{mm}$. (b) $J = 1.3J_{th}$ and $D_2 = 70\text{mm}$. (c) $J = 1.5J_{th}$ and $D_3 = 50\text{mm}$.

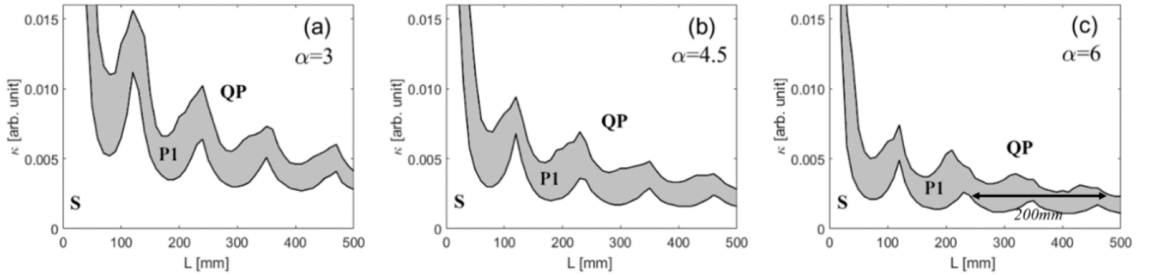


Figure 3.7: Influence of α on the P1 region with $J = 1.1J_{th}$. (a) $\alpha = 3$. (b) $\alpha = 4.5$. (c) $\alpha = 6$.

The approximate modulation periods D are shown on Figure 3.6, with $D_1 = 120\text{mm}$, $D_1 = 70\text{mm}$, and $D_1 = 50\text{mm}$, it indicates the modulation periods are

3.3. Proposed New Method for Displacement Measurement

decreasing with increasing of J . Each case also shows that the P1 region with a slight downward trend, which indicates the shorter the external cavity is, the higher κ is required to maintain the SL in P1 state. With the length of the external cavity increases, a lower feedback strength will cause the system switching between S and P1 state periodically. Furthermore, an increasing J causes narrower band of P1 region and move the band location to the high κ level. This will make the SL more difficult to be kept within P1 region.

Then, we investigate the influence of line-width enhancement factor α on the P1 region. We set three different line-width enhancement factors as $\alpha = 3$, $\alpha = 4.5$, and $\alpha = 6$, with a fixed injection current at $J = 1.1J_{th}$. The results are shown in Figure 3.7. It can be seen that α has a strong influence on the P1 region for $L < 300mm$. A large α leads to a low κ level is required to be maintained in P1 state, the overall P1 region tends flatter with increasing α . Therefore, an SL with a large line-width enhancement factors α is more likely to operate at P1 region.

3.3.2 Utilizing P1 region for displacement sensing

Based on the study of the P1 region in above, a low J and a relative large α are adopted to obtain a wide P1 region as show in Figure 3.7(c), an operating range is indicated up to about $200mm$. With this knowledge, we can operate an SL at a stable P1 state. Therefore, for the following simulations, we set $J = 1.1J_{th}$, $\alpha = 6$, $L = 300mm$. Through solving L-K equations, a bifurcation diagram for the SL can be obtained and shown in Figure 3.8. A relative laser intensity $I(t)$ is used to represent the MWP sensing signal, we define laser intensity $I(t)$ (normalized $I(t) = [E^2(t) - \overline{E^2(t)}]/E_0^2$, where E_0^2 is the laser intensity without optical feedback). It can be seen in the range from $\kappa = 1.25 \times 10^{-3}$ to $\kappa = 3.57 \times 10^{-3}$ (Hopf-bifurcation point to Neimark-Sacker bifurcation point), we can guarantee the SL with OF operating at P1 state. To test

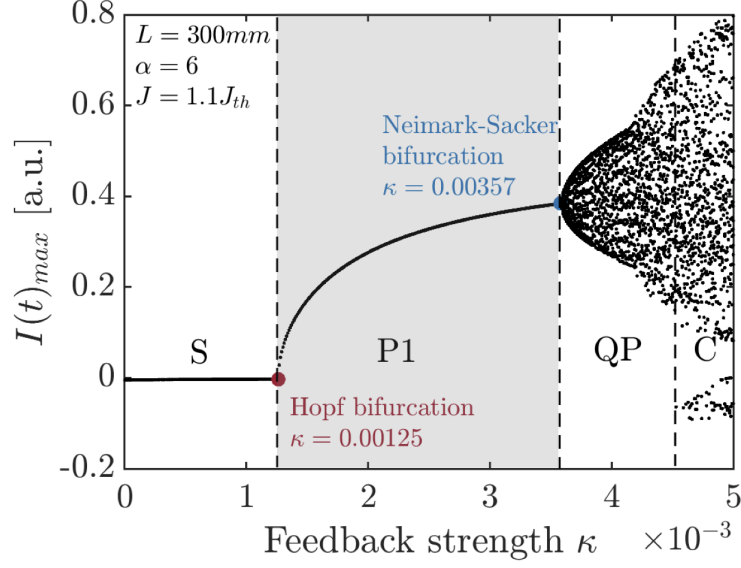


Figure 3.8: Bifurcation diagram for an SL with OF system, $J = 1.1J_{th}$, $\alpha = 6$, and $L = 300mm$.

the sensing performance for this system, we set $J = 1.1J_{th}$, $\alpha = 6$, $L = 300mm$, $\kappa = 2.5 \times 10^{-3}$ assume the external target has a linear displacement $\Delta L = 0.8\lambda_0 t$, through numerically solving the L-K equations, the MWP sensing signal in P1 state and external target movement ΔL are shown in Figure 3.9. From Figure 3.9, we found the $I(t)$ contains rich information related to the target displacement. The MWP sensing signal operating in the P1 region has a high frequency oscillation locating at $1.3GHz$ with its amplitude modulated by a slow varying Doppler displacement signal. This oscillate frequency is called as relaxation oscillation frequency with optical feedback (denoted by f_R). The envelop of $I(t)$ is periodically repeated with a period corresponding to $\lambda_0/2$, the corresponding Doppler frequency is $1.6MHz$, equivalent to a time period of $0.625\mu s$. We call each period $\lambda_0/2$ as an integer fringe. By counting the integer number of fringes (denoted by M), we can achieve a coarse measurement (denoted by ΔL_i) by Equation (3.9).

$$\Delta L_i = \frac{\lambda_0}{2} M \quad (3.9)$$

3.3. Proposed New Method for Displacement Measurement

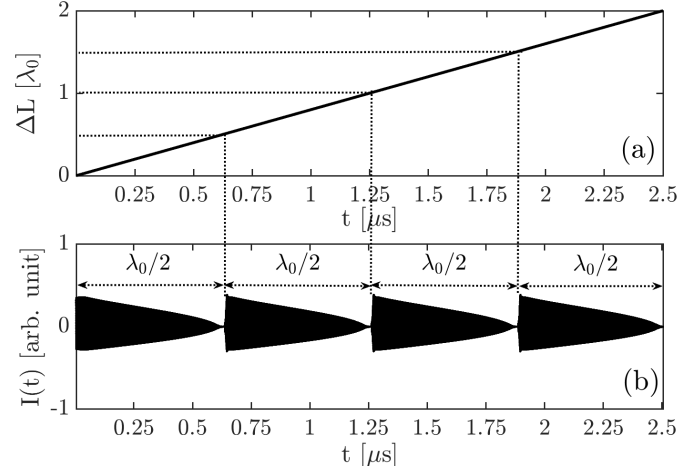


Figure 3.9: Utilizing P1 region for sensing. (a) Displacement of external target. (b) Corresponding MWP sensing signal in P1 region.

We further study the characteristics for the high frequency oscillation component of $I(t)$. Given ΔL changes from 0 to $1.5\lambda_0$ with a step of $0.01\lambda_0$. For each given ΔL , $E^2(t)$ is generated through solving L-K equations and then perform FFT on the $E^2(t)$ to determine its f_R , the relationship between f_R and ΔL shown in Figure 3.10.

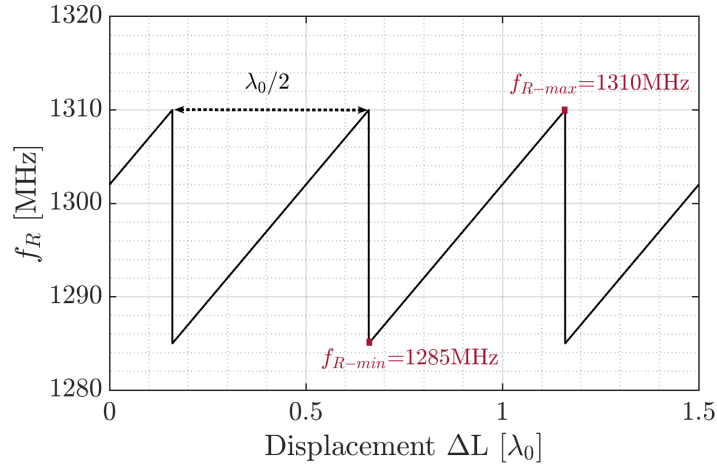


Figure 3.10: Relationship between f_R and ΔL .

From Figure 3.10, we found that the oscillation frequency is also time varying with a periodically change period of $\lambda_0/2$, within each period ($0 < \Delta L < \lambda_0/2$), there is a linear relationship between f_R and ΔL with a conversion slope $k_s = (f_{R-\max} -$

3.3. Proposed New Method for Displacement Measurement

$f_{R-\min})/(\lambda_0/2)$. This linear relationship enables us to develop a sensing method to measure the fractional fringe (denoted by ΔL_f) by using f_R . Therefore, a fine measurement for target displacement less the $\lambda_0/2$ can be made by Equation (3.10), where, $f_{R-start}$ is the f_R corresponding to the $E_{start}^2(t)$ recorded at the initial position of the target, and f_{R-end} is the f_R corresponding to the $E_{end}^2(t)$ recorded at the end position of the target. The displacement resolution for the fractional fringe measurement depends on frequency analysis device. For example, the Tektronix RSA5000 series spectrum analyzer can set resolution bandwidth (RBW) from $100Hz$ to $5MHz$, if we adopt an spectrum analyzer with spectrum resolution of $1MHz$ to record f_R , in the case of Figure 3.10, conversion slope $k_s = 0.064MHz/nm$, therefore, we can get a sensing resolution of $15.6nm(\lambda_0/50$, where $\lambda_0 = 780nm$). For further improving the sensing resolution, if a spectrum analyzer with spectrum resolution of $62.5kHz$ is employed. With the same conversion slope $k_s = 0.064MHz/nm$, the resolution can reach up to $0.98nm(\lambda_0/799$, where $\lambda_0 = 780nm$).

$$\Delta L_f = \frac{f_{R-end} - f_{R-start}}{k_s} \quad (3.10)$$

As indicated in Figure 3.8, the feedback strength κ can be adjusted to different values within P1 region. Figure 3.11(a) shows the extracted envelopes of MWP sensing signals $I(t)$ [denoted by $I(t)_{P1-Envelope}$] corresponding to different feedback strength with $\kappa = 2.0 \times 10^{-3}$, $\kappa = 2.5 \times 10^{-3}$, and $\kappa = 3.0 \times 10^{-3}$, respectively. It can be seen that a high feedback strength is recommended since its corresponding MWP sensing signal $I(t)$ can achieve a larger magnitude, this means a higher sensitive sensing can be achieved. Then, in the following section, starting from the L-K equations, we aim to get an approximate analytical expression for laser intensity in P1 dynamics, as shown in Figure 3.11(b) with dash line in red color, the detailed and specific mathematical derivation, please refer the following section.

3.3. Proposed New Method for Displacement Measurement

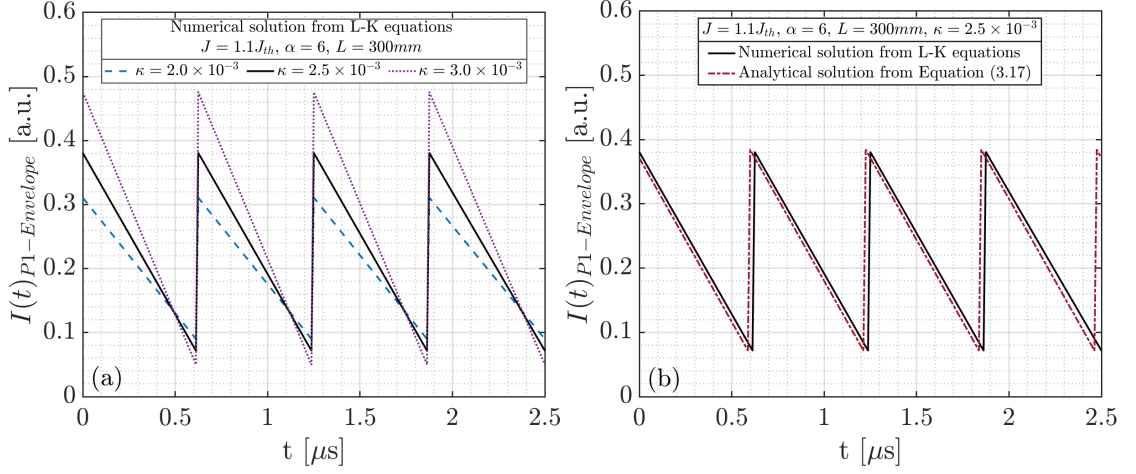


Figure 3.11: (a) Numerical solution of $I(t)_{P1-Envelope}$ under different feedback strength κ . (b) Comparison between the analytical solution from Equations (3.17) and the numerical solution from the L-K equations.

3.3.3 Model of laser intensity in P1 dynamics

In this chapter, we propose a brand new high-performance sensing implementation scheme. This scheme requires simultaneous recording of amplitude and frequency information in MWP signals. Interesting results are found in Figure 3.9(b), which is, the P1 high-frequency signal is modulated by the sawtooth-like slowly changing signal. This is similar to the sawtooth-like signal produced by SMI with moderate feedback. In the following, we take mathematical derivation and investigated it through the L-K rate equations model for making a analysis on laser intensity of P1 dynamics.

Starting from L-K equations and their corresponding stationary solutions as shown in Equations (2.14)-(2.16) in Chapter 2. And based on the numerical work of L-K model in [136], when an SL operates in period-one oscillation with unstable region, the expression of $E(t)$, $N(t)$, and $\phi(t)$ can be written as Equations (3.11)-(3.13), where, E_s , N_s , and ϕ_s are stationary solutions of $E(t)$, $N(t)$, and $\phi(t)$; δE , δN , and $\delta \phi$ are the modulation amplitudes; ϕ_E , ϕ_N are the initial phase of $E(t)$ and $N(t)$; $\omega_R = 2\pi f_R$, ω_R is the relaxation oscillation angular frequency and f_R is the relaxation oscillation

3.3. Proposed New Method for Displacement Measurement

frequency. Other involved parameters and physical meanings can be found in Table 2.1.

$$E(t) = E_s + \delta E \cos(\omega_R t + \phi_E) \quad (3.11)$$

$$N(t) = N_s + \delta N \cos(\omega_R t + \phi_N) \quad (3.12)$$

$$\phi(t) = (\omega_s - \omega_0)t + \frac{\delta\phi}{2} \cos(\omega_R t) \quad (3.13)$$

Bring Equations (3.11)-(3.13) into L-K Equations (2.11)-(2.13) respectively, and Equations (3.14)-(3.15) can be obtained by using Bessel function and Taylor expansion, where, $\omega_s \tau = (2n + 1)\pi$, n is an integer, which is used to guarantee the system in P1 dynamic state [137]. When the product of relaxation oscillation frequency and delay time equals an integer, the laser intensity is damped and suppressed [137].

$$\delta E = \frac{\omega_R^2}{\alpha E_s (N_s - N_0) G_N^2 \sin(\phi_N)} \sqrt{\frac{\omega_R \tau_{in} \cot(\phi_N) - 2\kappa \cos(\omega_s \tau)}{\omega_R \tau_{in} \cot(\phi_N) - \kappa \cos(\omega_s \tau)}} \quad (3.14)$$

$$\cot(\phi_N) = (\omega_R^2 - \omega_0^2) \frac{\tau_s}{\omega_R} - \cos(\omega_s \tau) \frac{\kappa}{\tau_{in} \omega_R} \quad (3.15)$$

Laser intensity can be written as $E^2(t)$, then, we bring Equation (3.14) and Equation (3.15) into Equations (3.11), when the external target has a displacement $\Delta L(t)$, keep the same setting with Section 3.3.2 [$\Delta L(t) = 0.8\lambda_0 t$], it will cause a varying feedback phase $\omega_s \tau(\Delta L) = \phi_F(\Delta L)$, we can get:

$$E^2(\Delta L) = I(\Delta L)_{SMI} + I(\Delta L)_{P1} \quad (3.16)$$

3.3. Proposed New Method for Displacement Measurement

Where,

$$\begin{cases} I(\Delta L)_{SMI} = E_0^2 + 2(E_0^2 + \frac{1}{G_N \tau_s}) \frac{\kappa \tau_p}{\tau_{in}} \cos[\phi_F(\Delta L)] \\ I(\Delta L)_{P1} = \frac{2\tau_p \omega_R(\Delta L)}{\alpha G_N} \sqrt{\omega_R(\Delta L)^2 + \left\{ \tau_s [\omega_R(\Delta L)^2 - \omega_0^2] - \kappa \frac{\cos[\phi_F(L)]}{\tau_{in}} \right\}^2} \cos[\omega_R(\Delta L)t + \phi_E] \end{cases} \quad (3.17)$$

From Equation (3.16) and Equation (3.17), it can be seen that, in P1 dynamic state, if external target has a moving or displacement, laser intensity contains two parts. One part is a low-frequency varying signal $I(\Delta L)_{SMI}$ with kHz , and another part is a high-frequency carrying signal $I(\Delta L)_{P1}$ with GHz . $I(\Delta L)_{SMI}$ is the conventional SMI signal reported in the many works of literature which have been fully reviewed in Chapter 2. This signal is in the form of sinusoidal with weak feedback case as shown in Figure 2.3(b) or sawtooth-like waveform with moderate or strong feedback level as shown in Figure 2.6(b) and Figure 2.8(b) when the external target has a displacement. Each periodical variation (called a fringe) corresponds to a displacement with half laser wavelength ($\lambda_0/2$). The second part $I(\Delta L)_{P1}$ is our main concern here because it also carries external target displacement information similar to SMI. Regarding $\omega_R(\Delta L)$ contained in Equations (3.17), $\omega_R = 2\pi f_R$, f_R changes with displacement ΔL in the form of a saw-tooth waveform with a period of $\lambda_0/2$ when the SL with OF system is in P1 dynamic state. Within one period, it can be described as Equation (3.18), where n is integer number, $f_{R-offset}$ is the offset value which is determined by the L and κ , and it is fixed when the operation conditions of SL are set. Then, to verify the envelope of the P1 signal describe in Equations (3.17), we set $J = 1.1J_{th}$, $\alpha = 6$, $L = 300mm$, $\kappa = 2.5 \times 10^{-3}$, which are keep unchanged with Section 3.3.2. Figure 3.11(b) shows a comparison between the result of the analytical solution from Equations (3.17) and the results of the numerical solution from the L-K equations. The analytical solution results are consistent with the numerical solution results, it proves that our result is correct and the laser intensity envelope of MWP signals in the P1 state can be

3.4. Experiments

used for sensing, one fringe corresponding to half laser wavelength. Further, we have verified in the experiments and observed the P1 high-frequency signal is modulated by a slowly changing signal when an external target is moving as shown in Figure 3.23. In addition, we also take experimental verification on the displacement sensing method proposed in this chapter, the implementation details are in the following section.

$$\begin{cases} \omega_R(\Delta L + n\frac{\lambda_0}{2}) = k_s \Delta L + \omega_{R-offset} \\ k_s = 2(f_{R-max} - f_{R-min})/\lambda_0 \end{cases} \quad (3.18)$$

3.4 Experiments

3.4.1 Implementation of experimental system

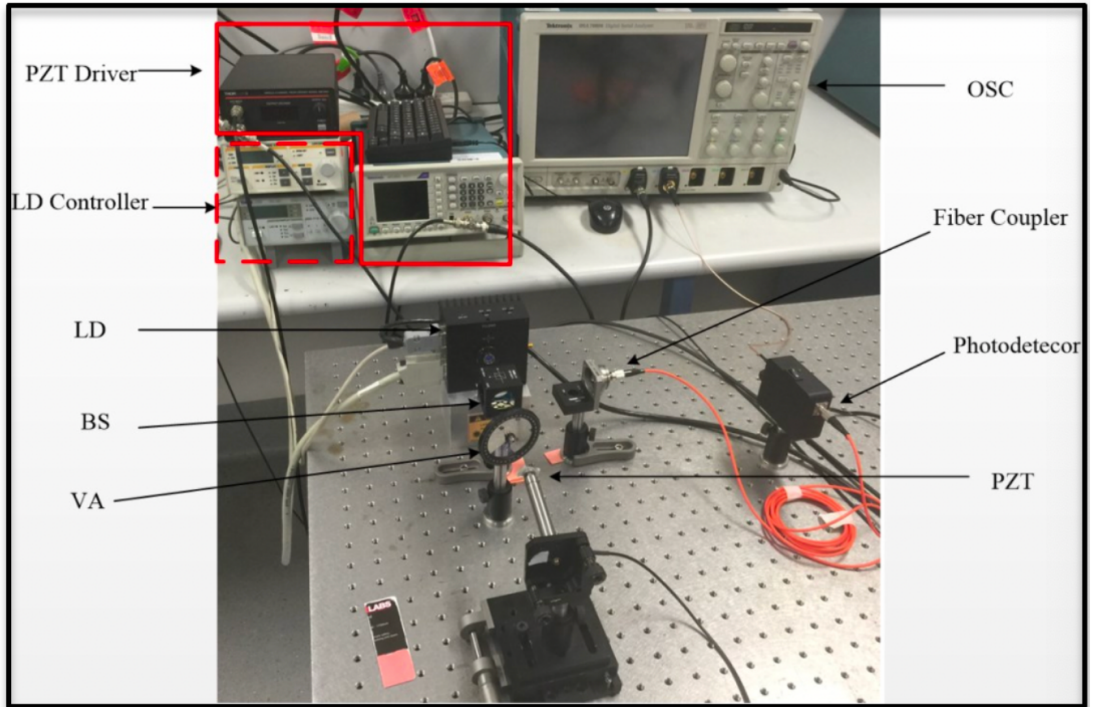


Figure 3.12: The experiment set-up of MWP sensing system. LD: laser diode; BS: beam splitter; VA: variable attenuator; OSC: oscilloscope; PZT: piezoelectric transducer actuator.

3.4. Experiments

To verify the proposed approach above, the experiment set-up of MWP sensing system is depicted in Figure 3.12. The laser diode (LD) is a single-mode (Hitachi, HL8325G, $\lambda_0 = 830nm$), and is driven by a laser controller (Thorlabs, ITC4001) with an injection threshold current of $J = 42mA$ and operating temperature at $T = 25 \pm 0.01^\circ C$. An external target (mirror) is attached to a piezoelectric transducer (PZT) actuator (PAS-009). The target is driven by a PZT actuator to have a small displacement range up to $20\mu m$. A variable attenuator (VA) is used to adjust optical feedback amount to enter the LD. A beam splitter (BS) with a splitting ratio of 50 : 50 is employed to direct a part of light into an external PD (Thorlabs, PDA8GS) with a bandwidth of $9.5GHz$. A high speed digital oscilloscope (Tektronix, DSA70804) with a maximum sampling rate of $25GHz$ and analog bandwidth of $8GHz$ is used. The oscilloscope can be utilized to observe output waveform of the MWP sensing signal $I(t)$ in time-domain and perform FFT on the sensing signal to get spectrum in frequency-domain.

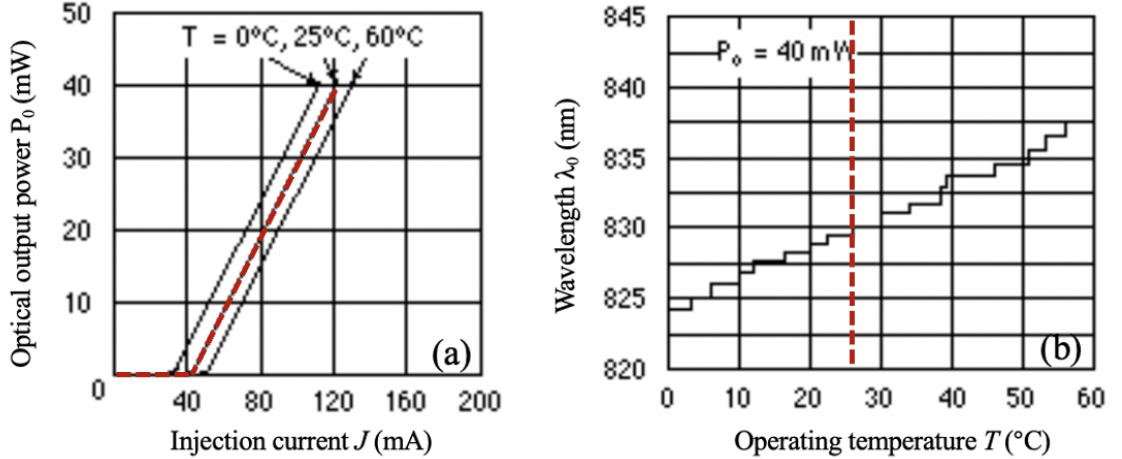


Figure 3.13: Typical characteristic curves of the laser diode Hitachi HL8325G. (The red dotted line is the case adopted in the following experimental operations.) (a) Optical output power versus injection current. (b) Laser wavelength versus operating temperature.

The details of the key components in experimental set-up are introduced in the

3.4. Experiments

following:

In the following, a single-mode LD is used as the laser source, which is HL8325G from Thorlabs. The detailed optical and electrical characteristics of this LD is shown in Table 3.1, and typical characteristic curves of the LD are shown in Figure 3.13. The LD is assembled in a temperature-controlled laser diode mount (Thorlabs, TCLDM9, characteristics shown in Table 3.2) as shown in Figure 3.14. During the experiments, the LD is driven by a laser controller (Thorlabs, ITC4001) with the injection current being above the threshold. The laser controller can operate with anode- or cathode-grounded LDs and PDs with a maximum driving current of 2A. With the ITC4001, LDs can be driven in constant current or constant power mode. The temperature of the LD is stabilized at the room temperature by the temperature controller (Thorlabs, TED 200).

Table 3.1: Specifications of the Laser Diode HL8325G.

| SPECIFICATIONS | VALUES |
|-----------------------|------------|
| Laser wavelength | 830nm |
| Output power | 40mW |
| Threshold current | 42mA |
| Operating temperature | -10 ~ 60°C |
| Operating current | ≤ 120mA |

Table 3.2: Specifications of the Laser Diode Mount TCLDM9.

| SPECIFICATIONS | VALUES |
|-------------------------|---------------|
| Laser package | Ø5.6mm & Ø9mm |
| Max laser current | 2A |
| RF modulation frequency | 0.1~500MHz |
| RF input impedance | 50Ω |
| Max RF power | 200mW |
| Temperature range | 5 ~ 70°C |

Since the PD packaged in the LD does not have a sufficiently fast rising time for detecting the MWP signal, an external fast photodetector PDA8GS from Thorlabs is employed. It is an InGaAs fiber-coupled amplified photodetector, and its specifications

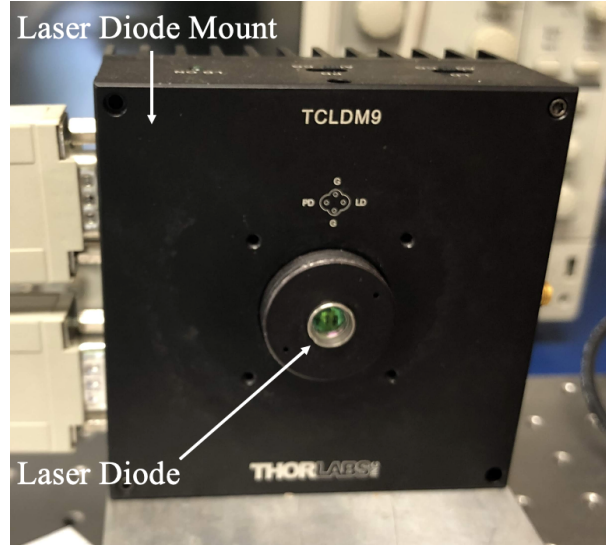


Figure 3.14: Laser diode and laser diode mount.

are shown in Table 3.3. PDA8GS has a bandwidth of $9.5GHz$, which is sufficient for most of the cases as the relaxation oscillation frequency of the typical commercial LD is usually several GHz . In order to couple the laser from the beam splitter into the fiber-coupler photodetector, a fiber-port coupler (Thorlabs, PAF2P-11B) is applied. Figure 3.15 shows the physical set-up for the coupler and photodetector. The laser coupled by the fiber-port coupler transmits through a multi-mode fiber into the photodetector.

Table 3.3: Specifications of the Photodetector PDA8GS.

| SPECIFICATIONS | VALUES |
|----------------------------|--------------------|
| Wavelength range | $750\sim 1650nm$ |
| Peak response | $0.95A/W@1550nm$ |
| Max optical input power | $1.0mW$ |
| Trans-impedance gain (V/A) | 46 into 50Ω |
| Bandwidth | DC- $9.5GHz$ |

In order to apply a continuous displacement on the external target. A PZT (PAS-009) from Thorlabs is used. It has a maximum travel length of $40\mu m$ and a displacement resolution of $40nm$, which is driven by a PZT driver (Thorlabs, MDT694B) with maximum driving output current of $60mA$. The detailed specification of the PZT is shown in Table 3.4. During the experiments, the PZT is assembled on a linear trans-

3.4. Experiments

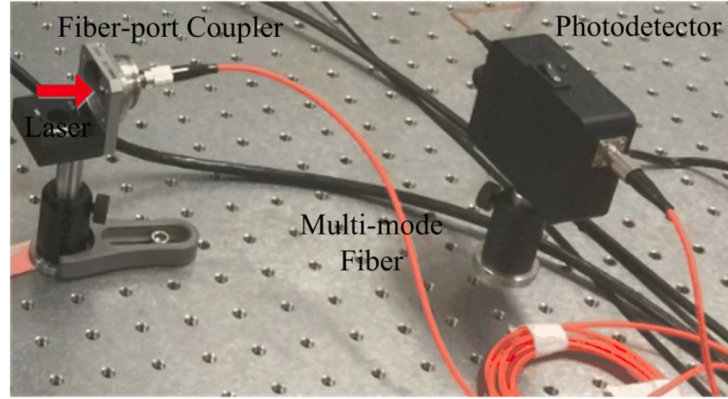


Figure 3.15: Fiber coupler, multi-mode fiber, and photodetector.

Table 3.4: Specifications of the PZT PAS-009.

| SPECIFICATIONS | VALUES |
|---------------------|------------|
| Travel length | $40\mu m$ |
| Length | $57mm$ |
| Resolution | $40nm$ |
| Capacitance | $7.2\mu F$ |
| Input voltage range | $0-75V$ |

lation stage as shown in Figure 3.16. The operating frequency range of the PZT is determined by three factors, i.e. the required PZT voltage for a certain displacement, the capacitance of the PZT and the maximum output current of the PZT controller, which is $7.2\mu F$ and $60mA$ respectively for the latter two.

As the MWP contains high-frequency oscillation, the common data acquisition card is not able to capture and record the MWP signals. In this work, a fast digital oscilloscope (DSA7804) from Tektronix is employed. The key specifications of the DSA7804 are summarized in Table 3.5. This oscilloscope has an analog bandwidth of $8GHz$, a

Table 3.5: Specifications of the Oscilloscope DSA7804.

| SPECIFICATIONS | VALUES |
|------------------|-------------|
| Bandwidth | $DC-8GHz$ |
| Analog channels | 4 |
| Sampling rate | $25GS/s$ |
| Recording length | 200M points |

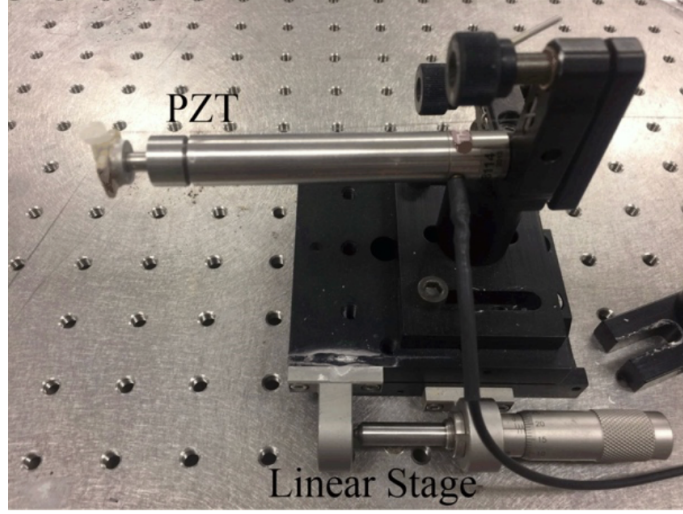


Figure 3.16: Assembled PZT and linear stage.

real-time sampling rate of $25GS/s$, a maximum recording length of $200M$ sampling points. Additionally, the function of spectrum analyzing is integrated. Therefore, it is capable to be used investigate the MWP signals in both time and frequency domain.

According to the set-up in Figure 3.12, in the following, we experimentally determine the P1 region for our physical system. Based on the theoretical study in previous sections, we give a low injection current $J = 1.1J_{th}$ (46.2 mA), and tested a few LDs, the α factor in the LDs can be calculated by utilizing the methods that our research group proposed in Refs. [138–140] previously, and choose the LD with $\alpha = 4$, the external cavity length $L = 410mm$. We adjust the VA to obtain a suitable feedback strength to ensure sensing system can maintain at P1 state. An example result in experiments can be seen in Figure 3.17, the MWP signal is captured by oscilloscope, and corresponding spectrum of MWP signal show a high frequency oscillation at $2608MHz$. Then, adjust J/J_{th} and L separately, keeping other experiment settings fixed. A two-dimensional map of the dynamical evolution of the LD with OF in the parameter space of J/J_{th} and L is integrated into Figure 3.18, where the injection current ratio is varied from 1.1 to 1.4 and the external cavity length is varied from $100mm$ to $500mm$. Form Figure 3.18, it can be seen that the system has a plentiful P1

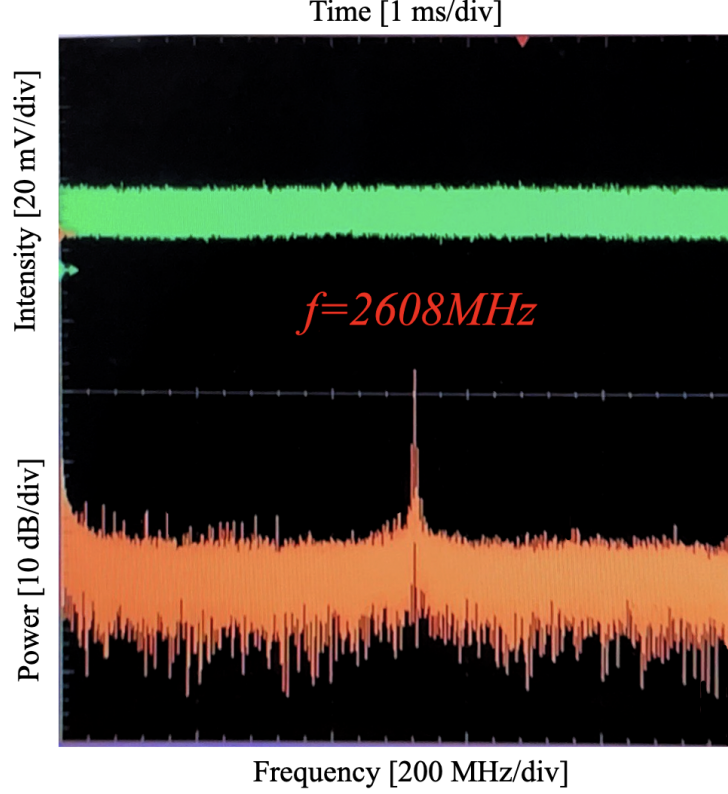


Figure 3.17: A typical example in experiments, which captured by the oscilloscope. Green: time domain MWP signal generated from P1 state. Orange: the corresponding spectrum of frequency domain MWP signal.

dynamic area span, which provides fertile ground for MWP signal generation, and a relatively low injection current facilitates operation in the P1 dynamic state. Further developments and investigations on MWP signals are in the following sections.

The nonlinear dynamics of the SL are excited into the P1 dynamic state by external perturbations of the OF, and the resulting MWP signal has the following attractive advantages. Firstly, the generated MWP signal has low phase noise, due to the phase of the OF induced P1 oscillation state being phase-locked by adding cavity feedback back to the SL. Secondly, since the feedback laser of the OF method is phase-locked with the light of the original laser, the OF method obtained microwave signal is also more stable. Thirdly, another reason of the microwave frequency is more stable is that the P1 oscillation caused by the optical feedback is related to the relaxation oscilla-

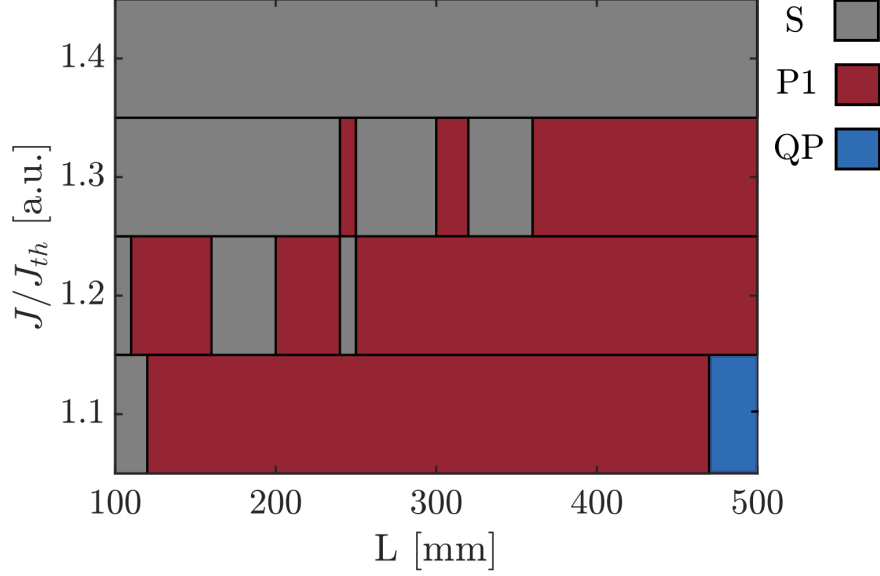


Figure 3.18: Mapping of dynamical states in the OF system with the parameter space of J/J_{th} and L . S: steady state; P1: period-one state; QP: quasi-period state.

tion frequency, the frequency of the generated microwave signal is near the relaxation oscillation frequency, the tuning purpose can be achieved through modulating the bias current and round-trip time. In the next section, keep the similar system set-up, we conduct and demonstrate detailed experimental performance of displacement sensing system.

3.4.2 Experiment results

The above numerical and experimental analysis shows the SL with OF operate in P1 state can be used in displacement sensing, we are able to achieve both integer and fractional fringe measurements. To verify the proposed approach, the complete physical structure of the experimental system is shown in Figure 3.12, and the core components of the system are depicted in Figure 3.19, respectively. The SL is a single-mode (Hitachi, HL8325G, $\lambda_0 = 830nm$, maximum output power $P_0 = 40mW$) and is driven by a laser controller (Thorlabs, ITC4001) with an injection threshold current

3.4. Experiments

of $J = 42mA$ and operating temperature at $T = 25 \pm 0.01^\circ C$. An external target (mirror) is attached to a piezoelectric transducer (PZT) actuator (PI, P-841.2). The target is driven by a PZT actuator to have a displacement range up to $30\mu m$. A variable attenuator (VA) is used to adjust optical feedback amount to enter the SL. A beam splitter (BS) with a splitting ratio of 50 : 50 is employed to direct a part of light into an external PD (Thorlabs, PDA8GS) with a bandwidth of $9.5GHz$. A high speed digital oscilloscope (Tektronix, DSA70804) with a maximum sampling rate of $25GS/s$ and analog bandwidth of $8GHz$ is used. The oscilloscope can be utilized to observe output waveform of the MWP sensing signal $E^2(t)$ and perform FFT on the sensing signal.

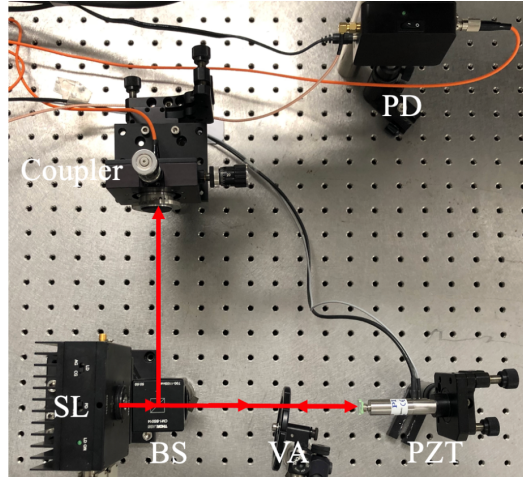


Figure 3.19: The core components of experiment set-up for displacement sensing. SL: semiconductor laser; BS: beam splitter; VA: variable attenuator; PD: photodetector. (The complete physical structure of the experimental system is shown in Figure 3.12.)

The measurement procedure is presented by the flowchart shown in Figure 3.20. The details of the main steps in measurement procedure are described as following:

First, we need experimentally determine the P1 region for our physical system. Based on the theoretical study in previous sections, we give a low injection current $J = 1.1J_{th}$ ($46.2mA$), and tested a few SLs, the α factor in the SLs can be calculated by utilizing the methods that our research group proposed in Refs. [138–140], and

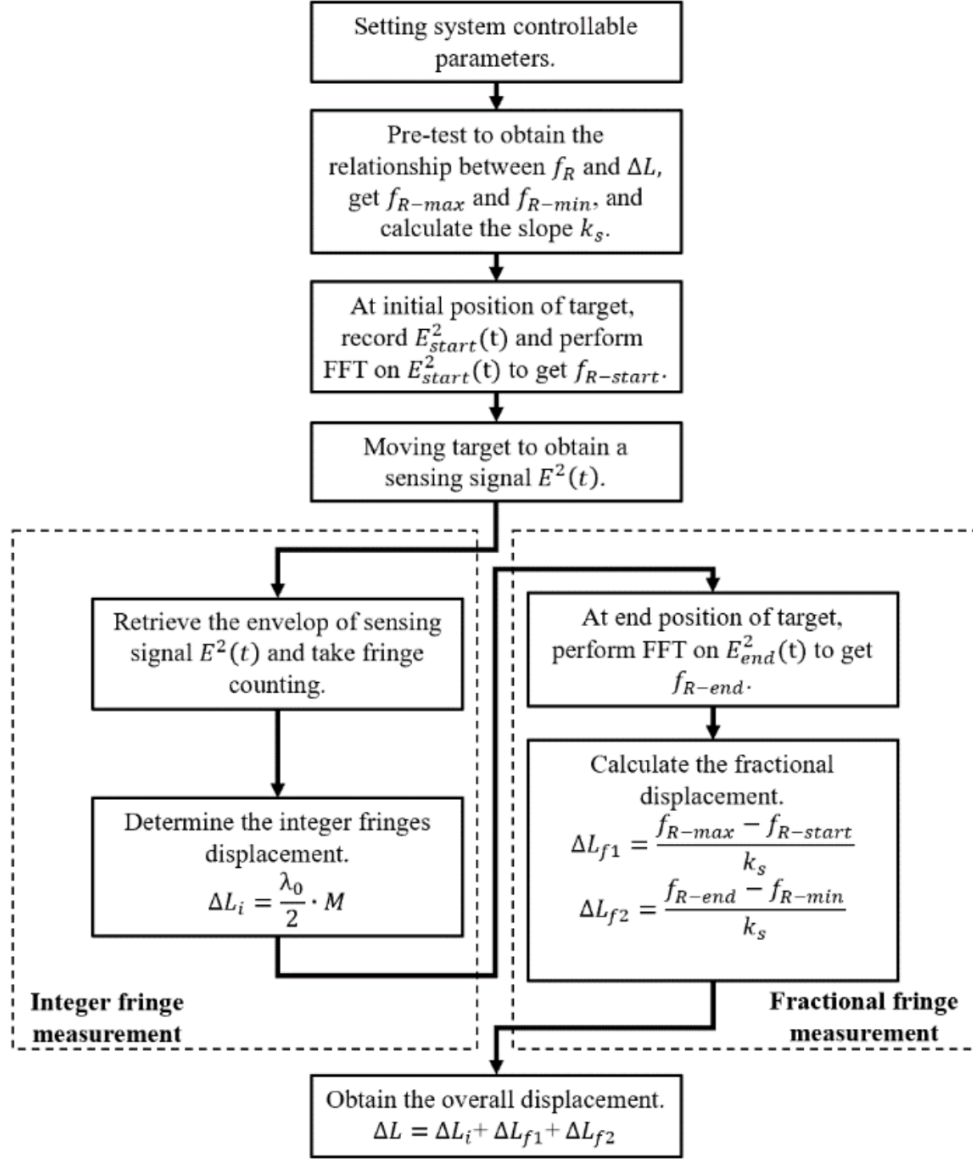


Figure 3.20: Measurement procedure of the proposed approach.

choose the SL with $\alpha = 4$, the external cavity length $L = 300\text{mm}$. We adjust the VA to obtain a suitable feedback strength to ensure sensing system can maintain at P1 state over the whole measurement range.

Second, apply 20nm displacement as step size on the PZT (PI, P-841.2) each time. For each step, observe the MWP sensing signal $E^2(t)$ from oscilloscope and ensure system operates in the P1 oscillation, then record its displacement ΔL and

3.4. Experiments

the corresponding relaxation oscillation frequency f_R through FFT function provided by the oscilloscope, we establish the relationship between f_R and ΔL as the pre-test. The pre-test experimental results are shown in Figure 3.21. It elucidates a linear relationship between f_R and ΔL with a conversion slope of $0.174MHz$, and we also record the value of f_{R-max} and f_{R-min} in Figure 3.21.

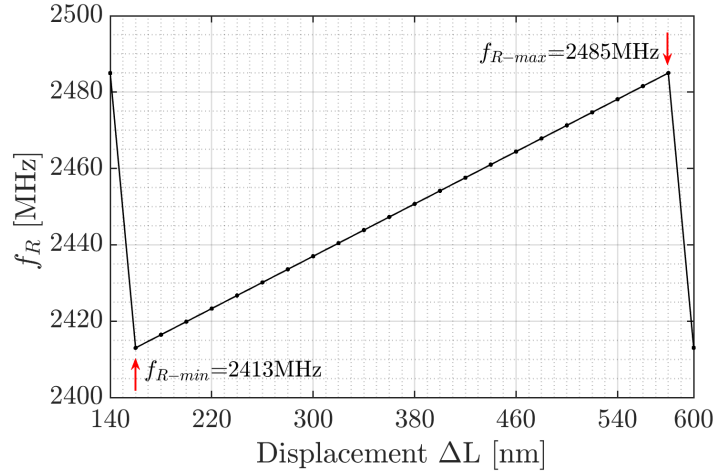


Figure 3.21: Pre-test results for the relationship between f_R and ΔL with $J = 1.1J_{th}$ (46.2mA), $L = 300mm$, and $\alpha = 4$.

Third, at the target initial position, we record the MWP sensing signal $E_{start}^2(t)$, then perform FFT on $E_{start}^2(t)$ to get $f_{R-start} = 2461MHz$, the MWP sensing signal $E_{start}^2(t)$ in P1 oscillation and its corresponding spectrum are given in Figure 3.22(a)-(b). A PZT controller is used to drive the target in a linear movement with $2072nm$ displacement and the linearity of the signal up to 0.15%, by generating a ramp driving voltage signal of $7V$ and apply it on PZT, shown in Figure 3.23(a), and Figure 3.23(b) gives the corresponding MWP sensing signal $E^2(t)$ in P1 region, which experimentally recorded by the oscilloscope. It can be seen that there are total four integer fringes in time domain signal of Figure 3.23(b), which corresponding to $\Delta L_i = \frac{\lambda_0}{2} \cdot 4 = 1660nm$, where $\lambda_0 = 830nm$.

When the target stop displacement at the end position, record the MWP sens-

3.4. Experiments

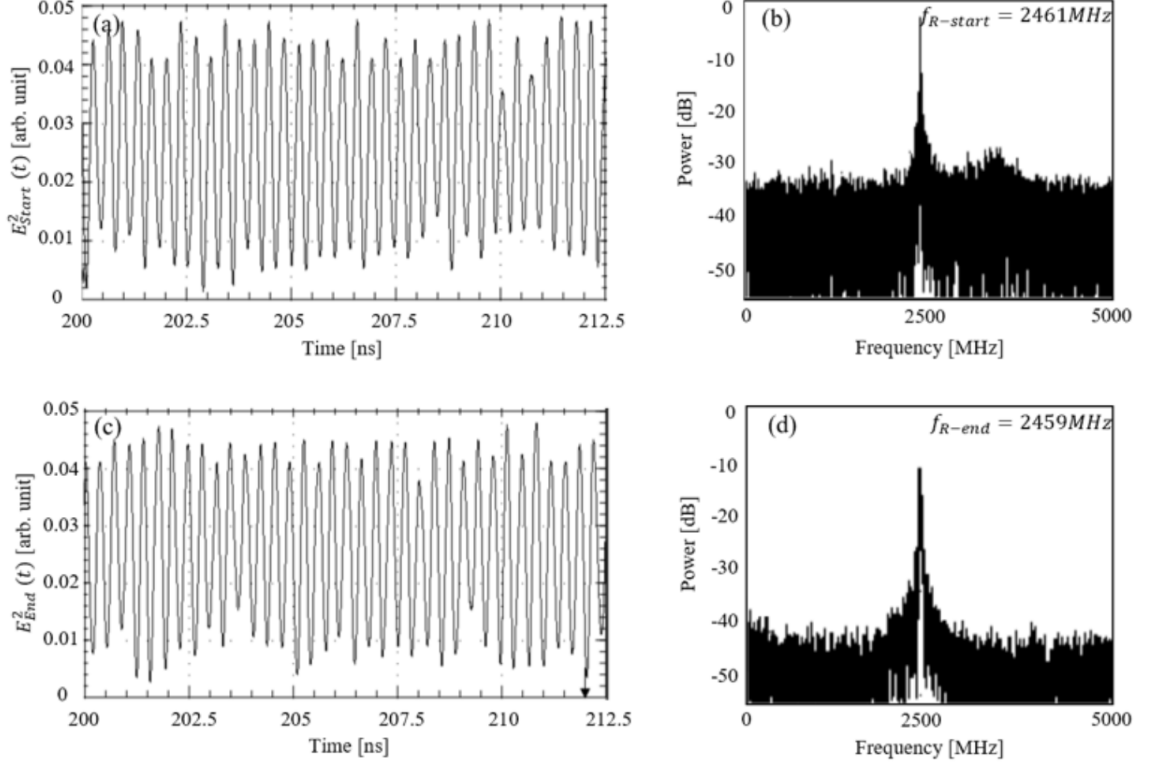


Figure 3.22: Experiment results. (a) MWP sensing signal $E_{start}^2(t)$ at initial position. (b) Spectrum corresponding to the $E_{start}^2(t)$. (c) MWP sensing signal $E_{end}^2(t)$ at end position. (d) Spectrum corresponding to the $E_{end}^2(t)$.

ing signal $E_{end}^2(t)$ shown in Figure 3.22(c), by performing FFT on the $E_{end}^2(t)$ to determine $f_{R-end} = 2459 MHz$, the MWP sensing signal $E_{end}^2(t)$ in P1 oscillation and its corresponding spectrum are given in Figure 3.22(c)-(d). Then we start fractional measurement. For example, in order to determine the displacement of ΔL_{f1} , the starting frequency $f_{R-start} = 2461 MHz$ can be get from Figure 3.22(b), and $f_{R-end} = f_{R-max} = 2485 MHz$, according Equation 3.10, we can easily get $\Delta L_{f1} = 137.93 nm$. Similarly, for ΔL_{f2} , $f_{R-end} = 2459 MHz$ can be seen from Figure 3.22(d), and $f_{R-start} = f_{R-min} = 2413 MHz$, we can calculate $\Delta L_{f2} = 264.37 nm$. Therefore, the overall displacement is $\Delta L = \Delta L_i + \Delta L_{f1} + \Delta L_{f2} = 2062.30 nm$, which is closed to the pre-set displacement value of PZT. We then repeat the experiments under the same laser operation conditions for different displacements by seting PZT controller.

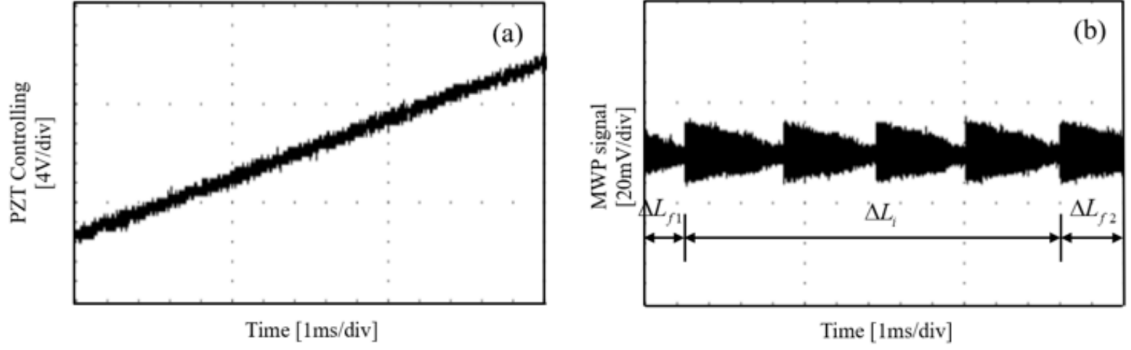


Figure 3.23: (a) A linear displacement applied on target by PZT. (b) The corresponding MWP sensing signal.

The results are shown in Table 3.6, from which, it can be found that the results from these two methods are consistent and the average difference is about $8nm$. The RBW of the high speed digital oscilloscope in this experiment is $62.5kHz$, which is adopted to record relaxation oscillation frequency f_R . The variation of f_R within a fringe is $72MHz$. If we can guarantee a perfect linear slope shown in Figure 3.21, a resolution of $0.36nm$ ($\lambda_0/2304$, where $\lambda_0 = 830nm$) for position sensing can be achieved. It can be seen that the obtained resolution by employing the SL with OF system operates at the P1 state, which provides a much higher resolution compared to the typical SMI.

Table 3.6: Displacement Results by PZT Controller and Proposed Algorithm.

| | | | | | |
|--------------------|----------|-----------|-----------|-----------|-----------|
| PZT controller | 650nm | 1100nm | 2072nm | 3100nm | 4204nm |
| Proposed algorithm | 643.74nm | 1112.27nm | 2062.30nm | 3091.52nm | 4207.89nm |

3.5 Chapter Summary

In this chapter, we studied the dynamic state boundaries of the P1 state in an SL with OF system. The effect of external cavity length L , feedback strength κ , injection current J , and line-width enhancement factor α on the boundary of the P1 state are investigated. Our study found that a low J , a relatively large α , and a suitable κ contribute SL with OF to operate more robust in the P1 state. In this case,

the SL generate a microwave photonic signal which can be used for achieving high performance sensing. As an application example, we built a displacement sensing experimental system. Both waveform and frequency of the MWP sensing signal contain the displacement information to be measured. Hence, we can achieve both integer and fractional fringe measurements. The work in this chapter contributes to designing a prototype of a compact displacement sensor by using MWP in cooperate with SMI configuration to achieve high sensing sensitivity, and high resolution.

Chapter 4

New Approach for Enhanced Displacement Measurement with Relaxation Oscillation

4.1 Chapter Introduction

Semiconductor laser (SL) with external optical feedback (OF) has drawn much attention in recent decades as it is one of the most interesting nonlinear systems to generate rich dynamic states [6, 46]. An SL and its external cavity form a compound cavity in the optical feedback system, which consists of an SL, a photodetector (PD), and an external target. The attraction of an SL with OF system is its merits of low cost in implementation, minimum part-count scheme, and ease in optical alignment for sensing and instrumentation. When the light backscattered from an external target and re-enters the laser cavity, the system produces a modulation of the laser optical output power for the generation of a number of microwave photonic (MWP) signals [121]. With the changes of the SL associated parameters such as injection current, feedback strength, and external cavity length, an SL with OF may exhibit a wide range of

nonlinear dynamical states including steady (S) state, period-one (P1) state, quasi-period (QP) state and chaos (C) state [129, 141]. Various practical applications have been developed for different dynamic states, e.g., displacement/velocity/vibration sensors [103, 142–145], absolute distance measurement [146], random bit generation [147], and secure communication [75]. Among them, SLs accompanied by external perturbation of optical feedback, which enables a stable locked SL to enter P1 dynamics through Hopf-bifurcation. The P1 state produces an intensity-modulated optical wave and gives regular pulsation at microwave frequencies [34, 148]. MWP signal generation based on P1 state has unique characteristics, including the elimination of high-speed electrons, almost single-sideband spectrum, and wideband microwave frequency tunability [106]. By taking advantage of such unique properties, P1 dynamic state has been proposed for microwave/millimeter-wave generation [84], MWP sensing/radar [19, 123], radio-over-fiber system [73], and other optical signal processing applications [32, 125].

For an SL with OF system under proper external operating conditions, P1 oscillation can be invoked through the undamped relaxation oscillation. The relaxation oscillation frequency can be determined by Lang and Kobayashi (L-K) equations [50], where the modulation is explained in terms of electric field and carrier density. Based on the well-known L-K rate equations, the effect of OF on the relaxation oscillation in SLs has been studied in Refs. [31, 33, 67, 69, 79, 81, 128, 144, 149]. For instance, the work in Ref. [149] studied the dynamics and the relaxation oscillation frequency in an SL with OF. It shows that the relaxation oscillation frequency decreases with the increase of external cavity length. Particularly, mode-hopping of frequency can occur after a fixed period. In the work of Ref. [128], a periodic sawtooth-like linear variation relationship between relaxation oscillation frequency and external cavity displacement is discovered with the period corresponding to half of the laser wavelength. The sens-

ing relationship is then applied for displacement sensing with a $53nm$ resolution and $2.12 \times 10^{-3}mm$ measurement range. In the work in Ref. [144] applied this sensing relationship for achieving nanometric sensing with a $12nm$ minimum detectible displacement and $5 \times 10^{-4}mm$ measurement range. In the work of Ref. [33], a similar SL with OF system but the SL is particularly set at P1 oscillation state to generate MWP signal for sensing. Through utilizing both time domain and frequency domain information, a measurement algorithm for recovering the displacement from an MWP sensing signal is developed, and it can achieve sensing with a $9.7nm$ resolution in a $1.5mm$ measurement range. In the work of Ref. [31], an SL with feedback produced by fiber Bragg grating is investigated. The work shows that with the increase of feedback delay time, an abrupt blueshift after a continuously redshift of relaxation oscillation frequency can occur.

The existing research works indicate that the relaxation oscillation frequency is highly influenced by the external cavity length of the SL. In this chapter, we propose to utilize comprehensive information including mode-hopping, frequency-hopping, and sawtooth-like phenomena relevant to the relaxation oscillation, generated by an SL with OF for displacement sensing. Through investigating these relationships, the measurement range can be significantly broadened to $240mm$, an increase of at least 160-fold when compared to Refs. [33, 128, 144]. These relationships can also enhance the measurement range in the SL with OF system proposed in the previous chapter. The proposed approach has great potential to achieve non-contact displacement measurement with large range and high resolution.

This chapter is organized as follows. In Section 4.2, the schematic diagram of the MWP displacement sensing system is presented, determination of displacement sensing range and features of MWP sensing signal are concluded. In Section 4.3, we deeply study the relationship between the relaxation oscillation frequency and the

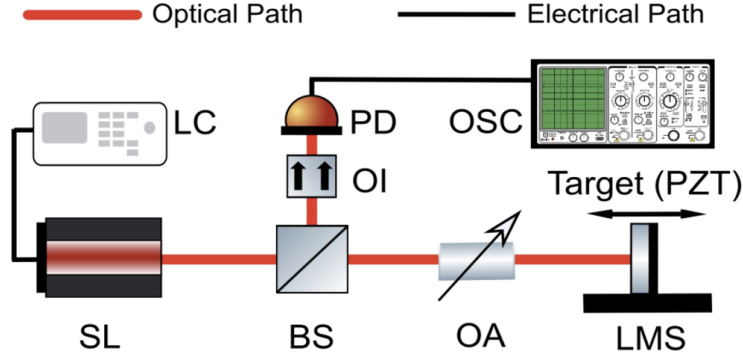


Figure 4.1: The schematic diagram of MWP displacement sensing system. SL: semiconductor laser; LC: laser controller; BS: beam splitter; OI: optical isolator; PD: photodetector; OA: optical attenuator; OSC: oscilloscope; LMS: linear motor stage; PZT: piezoelectric transducer actuator.

external cavity length, besides, mathematical expressions for this relationship have also been presented, from which sensing algorithm is developed. The numerical result reveals that with the unique relationship between relaxation oscillation frequency and displacement, the proposed system can achieve a wide measurement range with nanometric sensing. In Section 4.4, experiments are conducted to verify the proposed MWP system can achieve a high resolution for displacement sensing by only use relaxation oscillation frequency. Then, we make the discussion on sensing range and sensing resolution of the proposed method and analyze the impact of the controllable parameters on relaxation oscillation frequency.

4.2 The Behavior of Relaxation Oscillation Frequency

The schematic diagram of the proposed MWP displacement sensing system is shown Figure 4.1. The SL is driven by a laser controller (LC) with appropriate injection current and working temperature. The emitted light from the SL passes through a beam splitter (BS) and an optical attenuator (OA) and then hits on an external target, the light backscattered from the target and re-enters to the SL. We use a piece of the

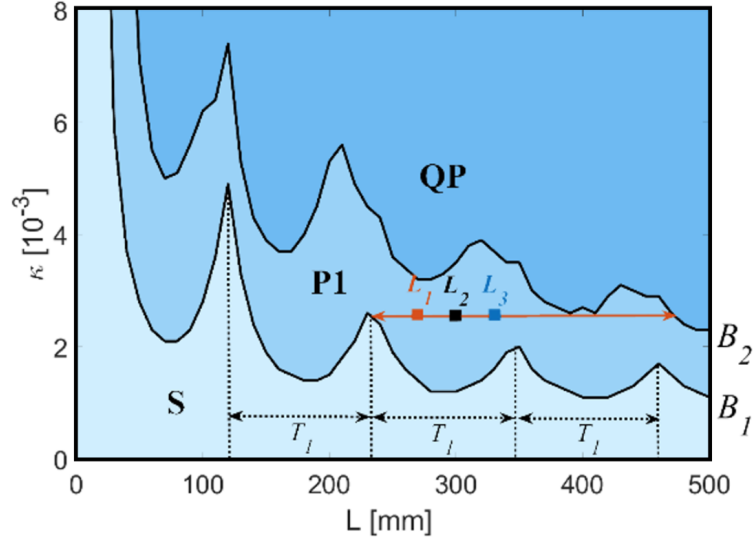


Figure 4.2: State diagram in the coordinate plane of (κ, L) for the MWP displacement sensing system with $J = 1.1J_{th}$. S: steady state; P1: period-one state; QP: quasi-period state. B_1 : boundary between S and P1; B_2 : boundary between P1 and QP.

mirror as the target that is attached to a piezoelectric transducer (PZT) actuator and then installed on a linear motor stage (LMS) to move the target located in different positions. The OA can adjust the feedback strength to the SL. By adjusting the system controllable parameters, the SL crosses the Hopf-bifurcation point and enter the P1 state to generate the MWP signal. The BS is employed to direct a part of light into an external PD, then, after optic-electro transform, the MWP signal can be recorded by an oscilloscope (OSC). After that, through performing fast Fourier transform (FFT) in OSC, we can obtain the frequency information corresponding to the MWP signal.

The L-K rate equations shown in are numerically solved by the fourth-order Runge-Kutta integration method, and the parameters adopted from Table 2.1, and fixed $\alpha = 6$ for the following study. State diagram is delimited as demonstrated in Figure 4.2, which shows the boundaries between different laser dynamic states in a (κ, L) plane with $J = 1.1J_{th}$, where J_{th} is the threshold of the injection current. State diagram is a 2-D map, the system can be operated under different nonlinear dynamic states by adjusting the values of κ and L . State boundaries B_1 and B_2 cover the area of P1,

4.2. The Behavior of Relaxation Oscillation Frequency

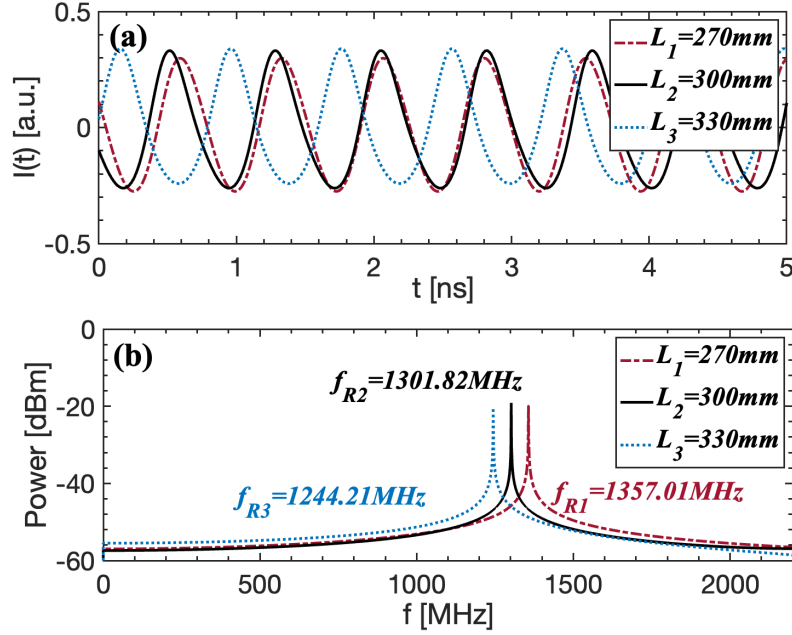


Figure 4.3: (a) Typical MWP signals generated from P1 state with $\kappa = 2.5 \times 10^{-3}$, $J = 1.1J_{th}$. (b) Corresponding spectrums of typical MWP signals.

which indicates the periodic fluctuated along L direction with a period of $T_1 = 115\text{mm}$. We aim to make full use of P1 area to achieve a sensing with large range, therefore, $\kappa = 2.5 \times 10^{-3}$ are selected to achieve the widest measurement range in the P1 area with $L \in [240\text{mm}, 480\text{mm}]$, as shown by the red arrow in Figure 4.2.

Focus on operating SL with OF to generate MWP signal in P1 state. A relative normalized laser intensity $I(t)$ is used to represent the MWP sensing signal, defined $I(t) = [E^2(t) - \overline{E^2(t)}]/E_0^2$, where $\overline{E^2(t)}$ is the mean of $E^2(t)$, and $E_0^2(t)$ is the laser intensity without optical feedback. As comparative examples, different values of L are applied with $L_1 = 270\text{mm}$, $L_2 = 300\text{mm}$, and $L_3 = 330\text{mm}$, other SL external controllable parameters are fixed at $J = 1.1J_{th}$, $\kappa = 2.5 \times 10^{-3}$. Typical MWP signals generated in the P1 state obtained from solving L-K equations are shown in Figure 4.3(a), and the corresponding spectrums of MWP signals are shown in Figure 4.3(b). The system enters P1 dynamics through Hopf-bifurcation with undamped relaxation

4.2. The Behavior of Relaxation Oscillation Frequency

resonance of the SL, P1 dynamics undergo self-sustained oscillation, from which relaxation oscillation frequencies reach up to $f_{R1} = 1357.01MHz$, $f_{R2} = 1301.82MHz$, and $f_{R3} = 1244.21MHz$ respectively, with different values of L . It can be clearly seen that f_R decreases gradually with the increase of L , the value of f_R associated with the L . Consequently, in the following, the detailed relationship between the external cavity length and the relaxation oscillation frequency is investigated both numerically and experimentally, and aim to explore a new MWP sensing method with a large range and high resolution.

The relaxation oscillation frequency f_R in P1 state is sensitive to the external cavity length. In following, we make an in-depth investigation on this relationship over a large range L . We propose to use the relaxation oscillation frequency f_R of the MWP signal $I(t)$ to measure the change in L . As shown in Figure 4.4, in order to clearly indicate the relationship between f_R and L , we choose a nano step size of $0.1\lambda_0$ ($78nm$) starting from $L = 240mm$ to $L = 480mm$ with $\kappa = 2.5 \times 10^{-3}$, $J = 1.1J_{th}$. For each L within the range $L \in [240mm, 480mm]$, we generate the MWP signal $I(t)$ through solving L-K rate equations and then FFT is applied on the MWP signal to determine its relaxation oscillation frequency.

The relationship between f_R and L is established, and the result is presented in Figure 4.4(a). It can be manifested that with the increase of external cavity length L , f_R first exhibits a continuous redshift before a sudden blueshift, and then repeats. In other words, the f_R decreases with the increase of L , and mode-hopping phenomenon occurs at the peaks of B_1 boundary (refer Figure 4.2). Relaxation oscillation frequency f_R is found to be bounded around solitary laser frequency f_s ($f_s = c/2T_1 = 1.3043GHz$) and exhibits periodic change with a period of T_1 ($T_1 = 115mm$), which is the same as the period of boundary B_1 shown in Figure 4.2. In particular, Figure 4.4(b) is the enlarge area 'M', it shows a frequency-hopping phenomenon with a fix period T_2

4.2. The Behavior of Relaxation Oscillation Frequency

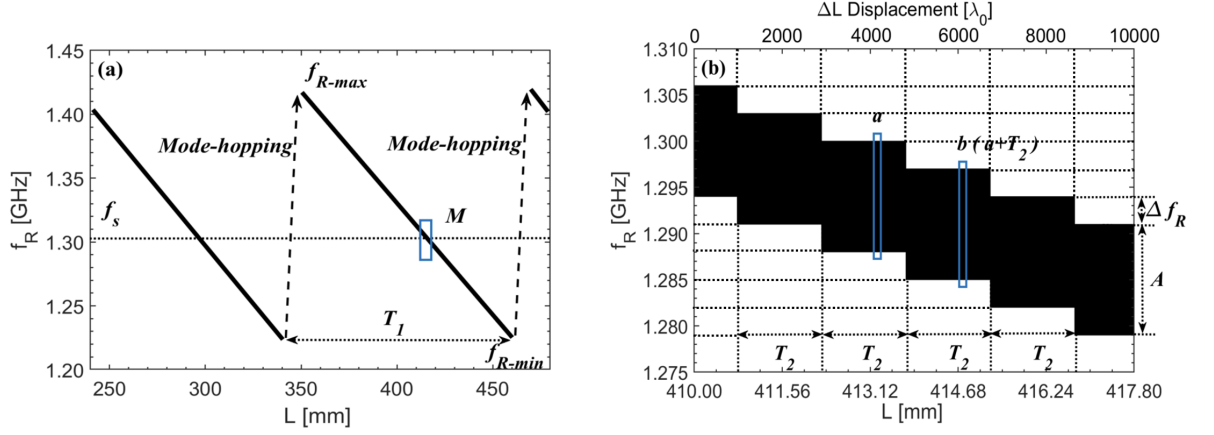


Figure 4.4: (a) Relationship between f_R and L with $\kappa = 2.5 \times 10^{-3}$, $J = 1.1J_{th}$. (b) Enlargement of rectangular area 'M' with $L \in [410.00mm, 417.80mm]$.

($T_2 = 1923\lambda_0 = 1.5mm$). The envelope of f_R decreases by $\Delta f_R = 3MHz$ per T_2 . In each T_2 , the difference between the maximum and minimum values of f_R constants at $A = 12MHz$. It can be seen this system contains a wide frequency-hopping bandwidth, and it can reach a wide frequency-hopping range by adjusting the location of the external target. In the top axis, displacement ΔL is introduced in Figure 4.4(b) with λ_0 as the unit, and Figure 4.4(b) shows the displacement after $L = 410mm$.

Then, we enlarge area 'a' and area 'b' of Figure 4.4(b), the interval between area 'a' and area 'b' is T_2 , and the enlarged area 'a' and area 'b' are shown in Figure 4.5(a) and Figure 4.5(b), respectively. It can be seen that f_R and ΔL exhibit sawtooth-like behavior with a period of T_3 ($T_3 = \lambda_0/2$), which has the same sensing resolution with the self-mixing interferometric signal where an SL is operated at a steady state. By counting the number of the sawtooth-like fringes T_3 , the integer fringe measurement can be achieved. Interestingly, by utilizing the periodicity of T_1 , T_2 , and T_3 in relaxation oscillation frequency, the measurement range can be greatly enhanced. Besides, the variation of f_R within one period is $A = 12MHz$ for both Figure 4.5(a) and Figure 4.5(b), thence, the conversion slope ($k_s = A/T_3$) between f_R and ΔL can be calculated

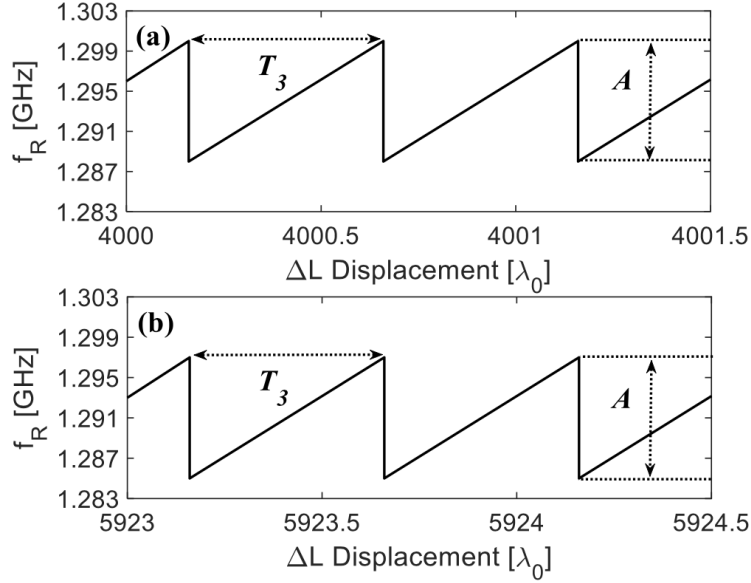


Figure 4.5: Relationship between f_R and ΔL . (a) Enlargement of area 'a' with $\Delta L \in [4000\lambda_0, 4001.5\lambda_0]$. (b) Enlargement of area 'b' with $\Delta L \in [5923\lambda_0, 5924.5\lambda_0]$.

as $k_s = 0.0308 \text{ MHz/nm}$. Hence, a very high sensing resolution can be achieved, by using this linear relationship for fractional part of a displacement measurement.

4.3 Sensing Signal Processing Algorithm

Taking full advantage of the unique relationship between f_R and L , we develop a sensing signal processing algorithm to retrieve displacement from MWP signals, especially for integer fringe measurement to broaden measurement range. Figure 4.4(a) contains a full T_1 period when L changes from 345 mm to 460 mm , the maximum point of f_R start at $(L^{\wedge}, f_{R-\max})$, and continue to redshift until the minimum relaxation oscillation frequency $f_{R-\min}$. In Figure 4.4(b), we denote the upper and lower envelopes of f_R as f_{up-en} and f_{low-en} , respectively. Utilizing unit step function to define the mathematical expressions of f_{up-en} and f_{low-en} , which can be written as Equation (4.1) and Equation (4.3).

For integer fringe displacement measurement, from Figure 4.4 and Figure 4.5, it

4.3. Sensing Signal Processing Algorithm

can be seen that we can get integer fringe displacement measurement by counting accumulation T_3 . For the case of a wider measurement range larger than T_2 , for convenience, the T_2 can be taken as the resolution to count the number of frequency-hopping fringes. It can greatly increase the measuring range for SL with OF system. For fractional fringe displacement measurement, in Figure 4.5, the relaxation oscillation frequency f_R is periodically changing within a certain range, the expression of f_R can be summarized as Equation (4.4), where, $n \in [0, T_2/T_3]$, $f_{R-offset}$ is the offset value which is determined by the L and κ , and it is fixed when the operation conditions of SL are set. The linear relationship between f_R and ΔL enables us to develop a sensing method to measure the target fractional displacement ΔL_f as shown in Equation (4.5). The target fractional displacement ΔL_f can be recovered via exploiting the conversion slope k_s together with the difference between the relaxation oscillation frequency at the initial position ($f_{R-start}$) and the relaxation oscillation frequency at the end position (f_{R-end}).

$$f_{up-en}(L - \hat{L}) = X_1^* + X_2^* + X_3^* + \dots + X_{end}^* \quad (4.1)$$

Where,

$$\left\{ \begin{array}{l} X_1^* = f_{R-max}[u(L) - u(L - T_2)] \\ X_2^* = (f_{R-max} - \Delta f_R)[u(L - T_2) - u(L - 2T_2)] \\ X_3^* = (f_{R-max} - 2\Delta f_R)[u(L - 2T_2) - u(L - 3T_2)] \\ \dots\dots \\ X_{end}^* = (f_{R-min} + A)[u(L - \frac{f_{R-max} - f_{R-min} - A}{\Delta f_R} T_2) - u(L - (\frac{f_{R-max} - f_{R-min} - A}{\Delta f_R} + 1)T_2)] \end{array} \right. \quad (4.2)$$

$$f_{low-en} = f_{up-en}(L - \hat{L}) - A \quad (4.3)$$

4.3. Sensing Signal Processing Algorithm

$$f_R(\Delta L + nT_3) = k_s \Delta L + f_{R-offset} \quad (4.4)$$

$$\Delta L_f = \frac{f_{R-end} - f_{R-start}}{k_s} \quad (4.5)$$

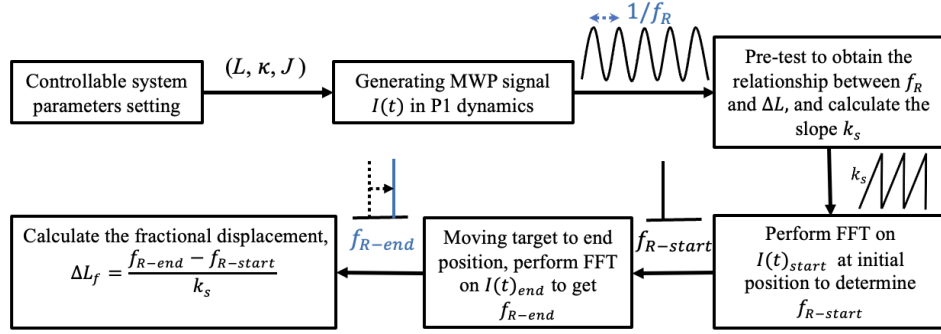


Figure 4.6: Measurement procedure of proposed algorithm.

Based on these features of MWP sensing signals in f_R and ΔL , we present an algorithm for achieving a wide range and high resolution sensing in this chapter. The Fractional displacement procedure algorithm is shown in Figure 4.6. The details of each step are described as following.

Step 1: Set controllable parameters according to P1 boundary conditions, including external cavity length L , feedback strength κ , and injection current J . Based on the previous theoretical analysis, we set $L = 410mm$, $\kappa = 2.5 \times 10^{-3}$, $J = 1.1J_{th}$.

Step 2: Under the appropriate controllable system parameter settings, the SL subjects to OF can operate in the P1 state and generate the MWP signal $I(t)$, which can be captured by the OSC.

Step 3: Set the movement step size of the external target and perform FFT on the MWP signal at each position to obtain the relationship between f_R and ΔL , then calculate the conversion slope k_s , under the controllable parameters set in Step 1, $k_s = 0.0308MHz/nm$.

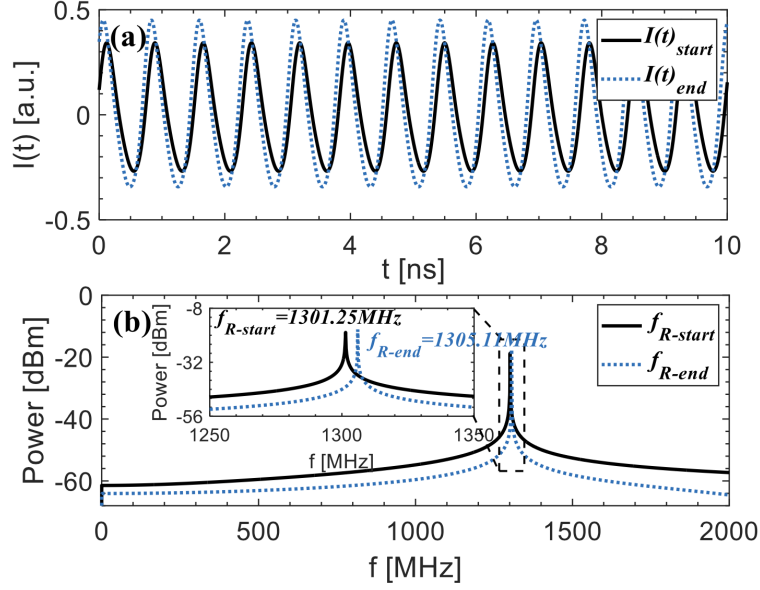


Figure 4.7: (a) MWP signals at initial position and end position. (b) The relaxation oscillation frequencies corresponding to the initial position and the end position.

Step 4: Fractional displacement measurement starts from this step. Utilizing the P1 state of laser dynamics to generate the MWP signal at the initial position $I(t)_{start}$, as shown in Figure 4.7(a). Perform FFT on the MWP signal $I(t)_{start}$ to obtain the relaxation oscillation frequency $f_{R-start}$ of the initial position, it can be seen from Figure 4.7(b), the corresponding $f_{R-start} = 1301.25 \text{ MHz}$.

Step 5: Move the external target with a fractional displacement of $0.16\lambda_0$ (124.80 nm), until the target stops at the end position, perform FFT on the MWP signal $I(t)_{end}$, to obtain the relaxation oscillation frequency f_{R-end} of the end position. As shown in Figure 4.7(b), $f_{R-end} = 1305.11 \text{ MHz}$.

Step 6: Calculate the difference between $f_{R-start}$ and f_{R-end} , the fractional displacement can be recovered by Equation (4.5). It can be calculated that $\Delta L_f = 125.32 \text{ nm}$, which is closed to the pre-set displacement and verified the feasibility of the proposed method.

4.4 Experiments

4.4.1 Experiment results

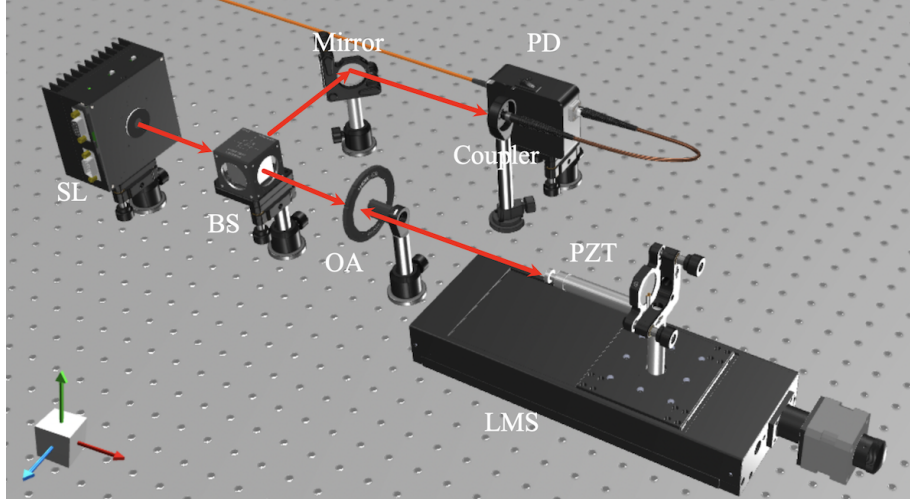


Figure 4.8: Experimental set-up. SL: semiconductor laser; BS: beam splitter; PD: photodetector; OA: optical attenuator; LMS: linear motor stage; PZT: piezoelectric transducer actuator.

We built a displacement sensing experiment to further verify the proposed MWP sensing system. The set-up is depicted in Figure 4.8. The laser source is a single-mode SL (Hitachi, HL8325) and emits at a wavelength of $830nm$. This SL is derived by the LC (Thorlabs, ITC4001). The working temperature is stabilized at $T = 25^{\circ}C \pm 0.01^{\circ}C$, and the injection threshold current is $J_{th} = 42mA$. A mirror is attached to a PZT (PI, P-841.2) as the external target, and the PZT is installed on a LMS (Thorlabs, NRT100/M), which enables the target to move up to $100mm$. The OA is used to adjust optical feedback amount that enter to the SL. The light is split via a 50/50 BS and direct apart of light pass through coupler into the external PD (Thorlabs, PDA8GS). A high speed OSC (Tektronix, DSA70804) with a maximum sampling rate of $25GS/s$, analog bandwidth of $8GHz$ is used, and the resolution bandwidth (RBW) is set at $62.5kHz$ to observed MWP sensing signals and performing FFT on the sensing

4.4. Experiments

signals. To make the MWP sensing system working at the P1 region, the OA should be adjusted to obtain a suitable feedback strength that ensure sensing system can maintain at P1 state over the whole measurement range. The injection current and initial external cavity length are chosen at $J = 46.2mA$ and $L = 300mm$. Then, we apply $30nm$ displacement as step size on the PZT each time. For each step, OSC is used to observe the MWP sensing signals and using FFT function in the OSC, we can obtain the corresponding relaxation oscillation frequency f_R as shown in Figure 4.9(a).

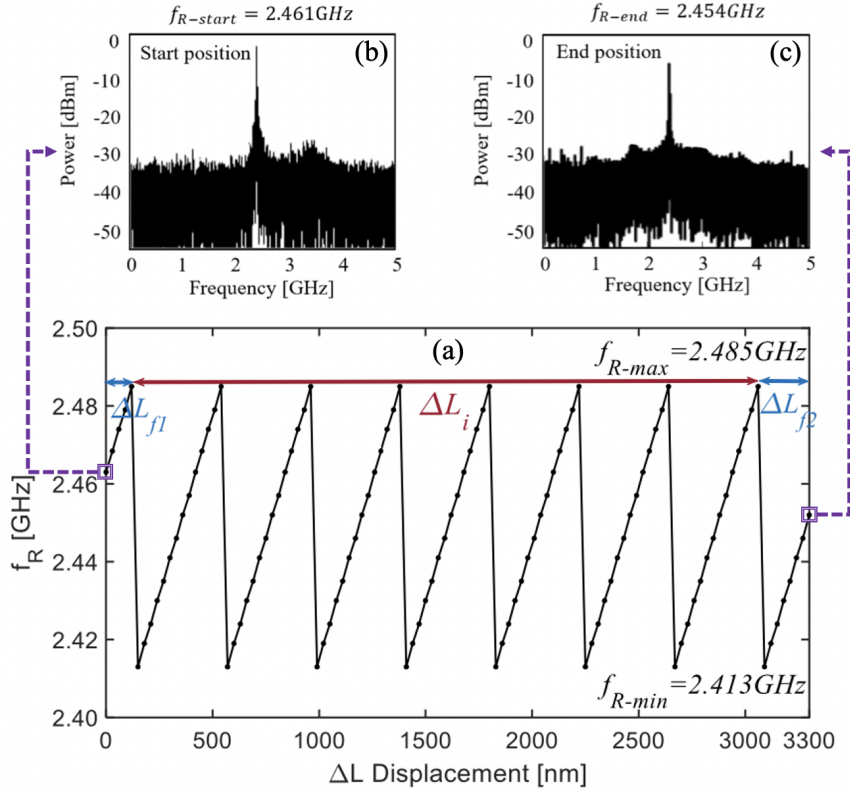


Figure 4.9: Experiment results. (a) Relaxation oscillation frequency variation with displacements. (b) Spectrum for MWP sensing signal at start position. (c) Spectrum for MWP sensing signal at end position.

Figure 4.9(a) illustrates the experimental results for the relationship between f_R and displacement ΔL in a $3300nm$ displacement with a linear conversion slope $k_s = 0.171MHz/nm$, it also indicates $f_{R-max} = 2.485GHz$ and $f_{R-min} = 2.413GHz$. Fig-

4.4. Experiments

Figure 4.9(b) and Figure 4.9(c) show the corresponding spectrums of MWP signals at start position and end position with $f_{R-start} = 2.461GHz$ and $f_{R-end} = 2.454GHz$. Based on the theoretical study and the measurement algorithm in previous sections, we retrieved a displacement information applied on the PZT through measurement for both integer and fractional fringes. In Figure 4.9(a), it can be seen that there are seven integer fringes in frequency domain information, which correspond to the integer displacement of $\Delta L_i = 7 \cdot T_3 = 2905nm$, where $T_3 = \lambda_0/2$. With the further increase of the displacement range, frequency-hopping and mode-hopping will occur, the integer fringe resolution can be replaced by T_2 and T_1 , respectively. Then, we can recover the total displacement by determining the fractional displacements ΔL_{f1} and ΔL_{f2} according to Equation (4.5). ΔL_{f1} can be calculated by $(f_{R-max} - f_{R-start})/k_s = 142nm$, similarly, ΔL_{f2} can be calculated by $(f_{R-end} - f_{R-min})/k_s = 240nm$. The overall recovered displacement is $3287nm(\Delta L_{f1} + \Delta L_{f2} + \Delta L_i)$, which is very close to the pre-set displacement in the PZT. We have repeated experiments for different displacements under the same experimental operating conditions. The results agree with the pre-set values. The measurement error may come from the laser wavelength shift caused by the influence of jitter in injection current, the accuracy of the relaxation oscillation frequency measured by the OSC, and the displacement error of the PZT actuator. Then, the following analyzes the assumptions made for the obtained resolution and the limitations due to not fully satisfying the assumptions. First, for the integer fringe part, the resolution relies on the accuracy of the T_3 ($\lambda_0/2$) measurement. Our experiments used a single-mode SL (Hitachi, HL8325) as the laser source. It emits at a wavelength of $\lambda_0 = 830nm$ in free running, but when working in P1 dynamics, the laser wavelength has a slightly shift induced by feedback. Second, for the fractional fringe part, the resolution depends on RBW/k_s , it needs to consider the error between the assumption of each control step size and the actual PZT integrated sensor, therefore,

when using the proposed system, it needs pre-calibration to guarantee high linearity for k_s .

4.4.2 Discussion

The proposed displacement method includes two measurement parts, which are integer fringe measurement and fractional fringe measurement. For the integer fringe measurement, in the experiments, we used $T_3 = \lambda_0/2$ as the resolution to count the number of sawtooth-like fringes. In the case of a wider measurement range (i.e., displacement larger than T_2), for convenience, the T_2 can be taken as the resolution to count the number of frequency-hopping fringes, one T_2 fringe pattern corresponds $1923\lambda_0$ [refer Figure 4.4(b)]. Therefore, a measuring range of $240mm$ as shown in Figure 4.4(a) can be achieved.

For the fractional fringe measurement, at the condition of the same conversion slope k_s , the sensing resolution for the target displacement depends on the frequency analysis device. The RBW of a commercial oscilloscope is usually from several Hz to several MHz . For instance, the Tektronix RSA5000 series spectrum analyzer can set RBW from $100Hz$ to $5MHz$, if the reference RBW of spectrum analyzer set at $62.5kHz$ and a perfect linear conversion slope is guaranteed as shown in Figure 4.5 with $\lambda_0 = 780nm$, where $k_s = 0.0308MHz/nm$, therefore, theoretically we can get a measurement resolution of $RBW/k_s = 2.03nm(\lambda_0/384)$. For further improving the sensing resolution, setting the spectrum analyzer at a more accurate RBW at $10kHz$. With the same conversion slope, the resolution can reach up to $0.32nm$ ($\lambda_0/2402$). However, a finer RBW leads to an increase in processing time and reduces the real-time processing of the sensing system.

Based on the discussion in the above sections, these controllable parameters have impact on f_R indeed. In order to investigate the robustness of MWP displacement

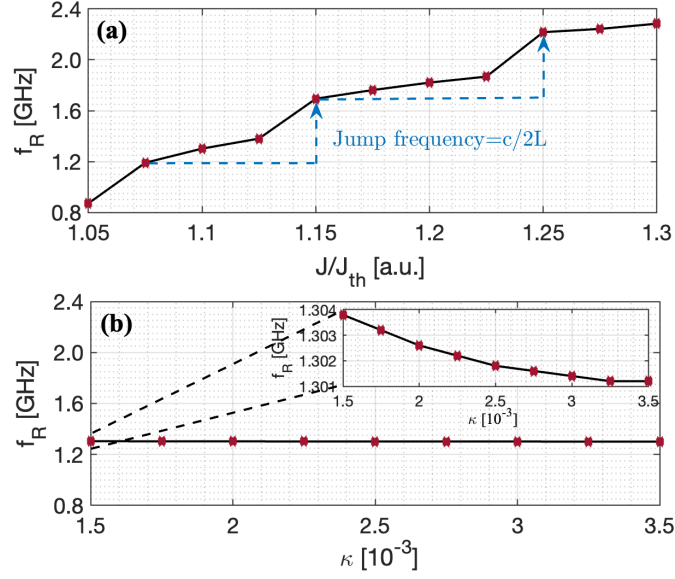


Figure 4.10: (a) The relationship between J and f_R . (b) The relationship between κ and f_R .

sensing system, the influence of controllable parameters on relaxation oscillation frequency f_R are analyzed. Firstly, we studied the influence of J . The sensing system works at P1 state from $J/J_{th} = 1.05$ to $J/J_{th} = 1.3$. We set step size of J/J_{th} at 0.025, and other controllable parameter unchanged ($\kappa = 2.5 \times 10^{-3}$, $L = 300mm$). For each J/J_{th} , we determine the f_R via solving the L-K equations. The relationship of J/J_{th} and f_R as shown in Figure 4.10(a). With the increase of the J , the value of f_R increases sharply with several jumps, which indicates f_R is highly sensitive to the change of J . The amount of the jump frequency 0.5GHz is consistent with the frequency of external cavity mode ($c/2L$, where $L = 300mm$). The jump of the frequency is originated from the alternation of the highest mode for the increase of the injection current. The resolution of commercial accurate current source can reach several pA to several μA , depending on maximum output current, e.g., Tektronix 6430 series current source can operate minimum current resolution at $1\mu A$ with a maximum $100mA$ output current. Then, we set two different current control accuracy values with $0.01mA$ and

4.4. Experiments

Table 4.1: The Influence of J 's Control Accuracy on Measurement Error with $\kappa = 2.5 \times 10^{-3}$, $L = 300mm$.

| Controllable accuracy | J | f_R | $ f_{R-error} $ | Measurement error |
|-----------------------|------------|--------------|-----------------|-------------------|
| $0.01mA$ | $46.21mA$ | $1302.80MHz$ | $0.98MHz$ | $31.82nm$ |
| $0.001mA$ | $46.201mA$ | $1301.91MHz$ | $0.09MHz$ | $2.92nm$ |

$0.001mA$, respectively, compared to the initial parameters setting: $J = 1.1J_{th}$ (where $J_{th} = 46.2mA$), $\kappa = 2.5 \times 10^{-3}$, and $L = 300mm$, in this case, $f_R = 1301.82MHz$ and conversion slope $k_s = 0.0308MHz$ as shown in Section 4.2. The influence of different current control accuracy on the f_R are shown in Table 4.1. It can be manifested that, at $0.001mA$ controllable accuracy, there is only $2.92nm$ measurement error. In order to keep the high resolution of MWP displacement sensing system, we need use an accurate current source to control SL, the controllable current accuracy at least reach up to $1\mu A$.

Then, we investigated the effect of injection current on the P1 boundary. Combining the results of Figure 4.2 and Figure 4.11 with injection current $J/J_{th} = 1.1, 1.3, 1.5$ set at different values, respectively. For the P1 region in the state diagram, with the increase of J/J_{th} , it shows an upward trend and maintains the characteristics of periodic fluctuation, while the fluctuation period becomes narrow, and the smaller fluctuation period will limit the available sensing area. Therefore, a relatively low injection current should be selected to increase the fluctuation period of the P1 region as much as possible, from which results in obtaining a flat usable sensing area.

The influence of feedback strength κ on the f_R is investigated as well. Based on the same parameter setting ($J = 1.1J_{th}$, $L = 300mm$), the MWP displacement sensing system can operate at P1 region from $\kappa = 1.25 \times 10^{-3}$ to $\kappa = 3.57 \times 10^{-3}$. We investigate the relationship between κ and f_R , by varying κ from 1.5×10^{-3} to 3.5×10^{-3} with a step size of 0.25×10^{-3} , for each κ , we determine the f_R via solving the L-K equations. The relationship of κ and f_R can be obtained and shown in Figure 4.10(b). With

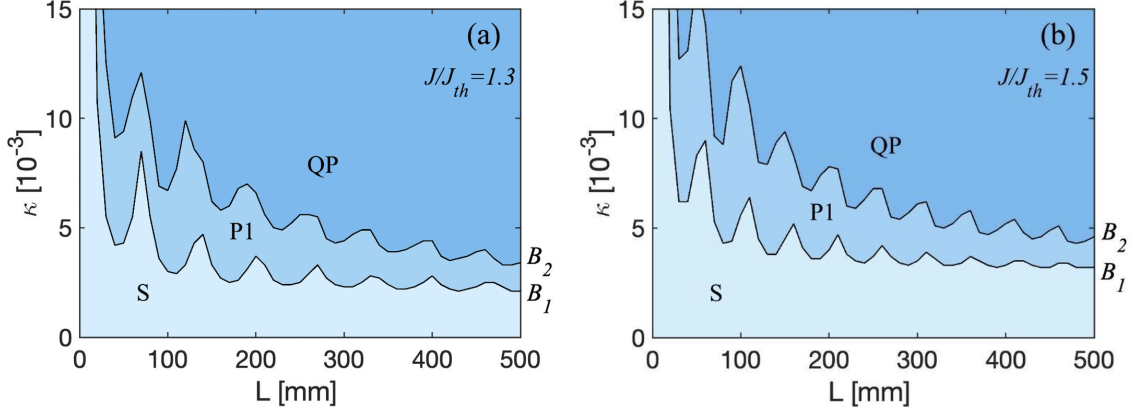


Figure 4.11: The effect of injection current on the state diagram. (a) $J/J_{th} = 1.3$. (b) $J/J_{th} = 1.5$.

Table 4.2: The Influence of κ 's Control Accuracy on Measurement Error with $J/J_{th} = 1.1$, $L = 300mm$.

| Controllable accuracy | κ | f_R | $ f_{R-error} $ | Measurement error |
|-----------------------|-----------------------|------------|-----------------|-------------------|
| 0.1×10^{-3} | 2.6×10^{-3} | 1301.72MHz | 0.10MHz | 3.25nm |
| 0.01×10^{-3} | 2.51×10^{-3} | 1301.82MHz | 0MHz | 0nm |

the increase of κ , f_R displays a slightly decreasing trend with an inverse proportional relationship. We further make a close look at the influence of slight disturbance of κ on f_R by setting $\kappa = 2.51 \times 10^{-3}$ and $\kappa = 2.6 \times 10^{-3}$, respectively, to compare with initial parameters setting in Section 4.2: $\kappa = 2.5 \times 10^{-3}$, $J = 1.1J_{th}$, $L = 300mm$. The results are shown in Table 4.2, under these different values of κ , the f_R has less changed. Accordingly, f_R is not sensitive to slight changes in κ , this characteristic also guarantees the measurement accuracy of the proposed sensing method.

4.5 Chapter Summary

Under proper selection of the controllable system parameters for an SL with OF, such a system can generate rich nonlinear dynamics with attractive sensing applications. In this chapter, we propose to operate an SL with OF at P1 state to generate MWP

signals for displacement measurement. It is found that the relaxation oscillation frequency carried in MWP signals is very sensitive to the displacement of an external cavity of the SL. The mathematical expressions of the relaxation oscillation for measuring displacement are developed. The proposed measurement method enables a very high conversion slope between relaxation oscillation frequency and displacement. By considering the unique characteristics of mode-hopping, frequency-hopping, and sawtooth-like periodic manners that occurs in the relationship of relaxation oscillation frequency and displacement, a nano-scale resolution for displacement sensing is able to achieve over a wide measurement range. The influence of system controllable parameters on relaxation oscillation frequency is also analysed in the discussion section. The verification results illustrate that the relaxation oscillation frequency is sensitive to the value of the injection current rather than the feedback strength. This proposed method promotes achieving a new non-contact displacement sensor with wide measurement range and high resolution.

Chapter 5

New Approach for Absolute Distance Measurement near Hopf-bifurcation Boundary

5.1 Chapter Introduction

A semiconductor laser (SL) with optical feedback (OF) has drawn much attention in recent decades as it is one of the most interesting nonlinear systems to generate rich nonlinear dynamic states [6, 46]. The attraction of an SL with OF (SLOF) scheme is its merits of low cost in implementation, minimum part-count scheme, ease in optical alignment, and high dimensionality [121, 145]. The external OF perturbation enables a stable locked SL to enter period-one (P1) dynamic through Hopf-bifurcation. For an SL in the stable state, the OF light is coupled with the light in its internal cavity, the coupled light modulates the frequency and intensity of the SL output light. This has led to the discovery of a class of laser interferometry, named self-mixing interferometry (SMI), also known as optical feedback interferometry [49]. Under certain external settings (e.g., increasing the OF strength), the system leaves the stable

state, then P1 oscillation can be invoked through the Hopf-bifurcation and accompanied by an undamped relaxation oscillation [106]. The P1 oscillation produces an intensity-modulated optical wave and gives regular pulsation at microwave frequencies [33, 34, 148, 150]. P1 oscillation has been found in many significant applications, such as the generation of microwave/millimeter-waves [84], photonic microwave sensing/radar [31, 123], radio-over-fiber systems [8, 73], and other optical signal processing applications [32, 125].

An interesting phenomenon called “switching” in an SL with external perturbation has drawn much attention for exploring its applications. In 2012, the work in Ref. [151] reported that the switching happened in the laser mutual coupled SLs and generated a laser intensity signal in square waveform with its time period equal to the time delay (or twice of the time delay). In 2017, the work in Ref. [121] reported that a tunable switching between the stable state and P1 state in an SL with OF can be achieved in a long-cavity region with about $10m$, it gives a potential application for square wave modulated photonic microwave generation. A very recent work Ref. [152] in 2021, demonstrated regular and irregular dynamics switching in a discrete-mode SL, also in a long-cavity region with about $32m$. The switching is found between stable state and P1 oscillation, as well as stable state and quasi-period/chaotic oscillation. Such switching status-induced square wave signals provide a new way for generating clock signals required by high-speed signal processing and communication systems. Various applications by making use of such switching-induced tunable square wave laser signals can be found, such as laser micromachining, and physical random number generations [153–155].

In this chapter, we propose to use an SLOF system operating at a switching status that happened between stable state and the P1 state for distance sensing. The system configuration of the proposed SLOF is similar to a conventional SMI that consists of

an SL and external target. Regarding the SMI-based distance measurement, the work in Ref. [146] adopts a triangular modulated injection current to an SL by using an SL driver with frequency of $200Hz$ and maximum depth of $0.01mA$ (peak-to-peak). Within each triangular period, the fluctuation frequency of the laser power is related to the distance to be measured. This work achieved distance measurement with a range of $23cm$ and resolution of $2.7mm$. The triangular modulation frequency and depth limit the measurement range and resolution. The work in Ref. [59] proposed to modulate the injection current in the form of sinusoidal waveform and, meanwhile, use an electro-optic crystal in the external cavity for the light phase modulation. A double-modulation technique was introduced to improve the measurement resolution. This work can measure up to $47.7cm$ distance with $0.3mm$ resolution. Another work reported in Ref. [156] achieved a $2m$ range and $1.5mm$ resolution, also by using a triangular modulated injection current with a frequency of $700Hz$ and an amplitude of $1.5mA$. By using the pulse-counting method within each triangular period, the distance could be obtained. Modulating the SL with a stronger current can obviously increase the resolution. However, the modulation is limited by the electro-optical characteristic of SL. In a very recent work Ref. [157], an all-fiber laser SMI range finder with $15m$ range and $47mm$ relative error was reported. This work used a tunable fiber Fabry–Perot filter as a frequency selection device and requires applying a triangular modulated voltage signal onto the Fabry-Perot filter. The modulation frequency of $50Hz$ and modulation voltage of $50mV$. This system has a wide sweep range of frequency and, thus, improved measurement range. Above reported SMI-based distance sensing systems require the use of an external electrical or optical modulation. The proposed approach using an SL with OF in this chapter can remove those requirements. Besides, unlike above, SMI-based methods that require a feedback light from a target must located within half of the SL coherent length, the method

presented in this chapter can eliminate the coherent length restriction by operating an SL at switching status for distance sensing. Furthermore, the proposed sensing system can greatly improve the sensing performance in terms of range, and resolution compared to SMI-based sensing. In this chapter, we also investigated the influence of the system controllable parameters on the duty cycle of the switching period and studied how to maintain the system robustly working at the proposed working status. Through utilizing the relationship developed between switching period and external cavity round trip time, the external target distance information could be detected.

Following this introduction, the SLOF system structure and its Hopf-bifurcation boundary between stable state and P1 state are presented in Section 5.2. Then, in Section 5.3, the generation of a square wave signal is demonstrated and the measurement algorithm for distance recovery is developed. In Section 5.4, experiments are conducted to verify the proposed distance sensing method. A conclusion is drawn in Section 5.5.

5.2 Operating SL with OF at Switching Status

The experimental set-up of the proposed SLOF distance sensing system is shown in Figure 5.1. The emitted light from the SL passed through beam splitter (BS), optical attenuator (OA), and optical fiber, and then touched on an external target. Then, the light backscattered from the target and re-entered the SL. The SL was driven by a laser controller (LC) with an appropriate injection current and temperature. We used a piece of the mirror as the target to provide sufficient optical feedback to the SL. We defined external cavity length $L = L_0 + \Delta L$, where L_0 is the initial external cavity length from the SL facet to the optical fiber coupler 2 (C_2), and ΔL is the distance to be measured from the coupler C_2 to the external target. The feedback strength of system could be adjusted by varying the OA. The BS was employed to direct a

5.2. Operating SL with OF at Switching Status

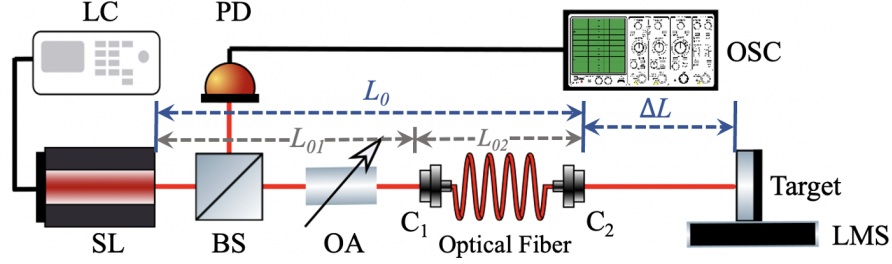


Figure 5.1: The experimental set-up of SL with OF distance sensing system. SL: semiconductor laser; LC: laser controller; BS: beam splitter; C: optical fiber coupler; PD: photodetector; OA: optical attenuator; OSC: oscilloscope; L_0 : initial external cavity; L_{01} : free space distance; L_{02} : optical fiber distance; ΔL : distance to be measured.

part of light into an external photodetector (PD), then, the microwave signal could be recorded by a high-speed digital oscilloscope (OSC). Comparing to the conventional SMI configuration, the main modifications were to replace the internal low speed PD with a fast speed external PD and to use a long optical fiber to form the external cavity.

Based on the Lang-Kobayashi (L-K) rate equations demonstrated in Equation 2.11- Equation 2.13, which are solved numerically by the fourth-order Runge-Kutta integration method. We set the controllable parameters $\alpha = 6$ and $J = 1.1J_{th}$, where J_{th} is threshold injection current. Varying the L from $0m$ to $1.2m$ with a step of $10mm$. For each L value, we gradually increase κ from 0 to 0.015 with step of 0.0001 , then observe the waveform of time-series signals $I(t)$ (normalized $I(t) = [E^2(t) - \overline{E^2(t)}]/E_0^2$, where E_0^2 is the laser intensity without optical feedback), and record the corresponding dynamic state. Subsequently, a state diagram for the SL with OF distance sensing system can be plotted, shown in Figure 5.2. The Hopf-bifurcation boundary between stable state and P1 state is demonstrated as red color in Figure 5.2, indicating a fluctuation feature when L was in a short-cavity region, the short-cavity region corresponded to the Hopf-bifurcation boundary with obvious fluctuation (e.g., $L < 0.9m$). However, with the increase of L , the fluctuation of the Hopf-bifurcation boundary was gradually

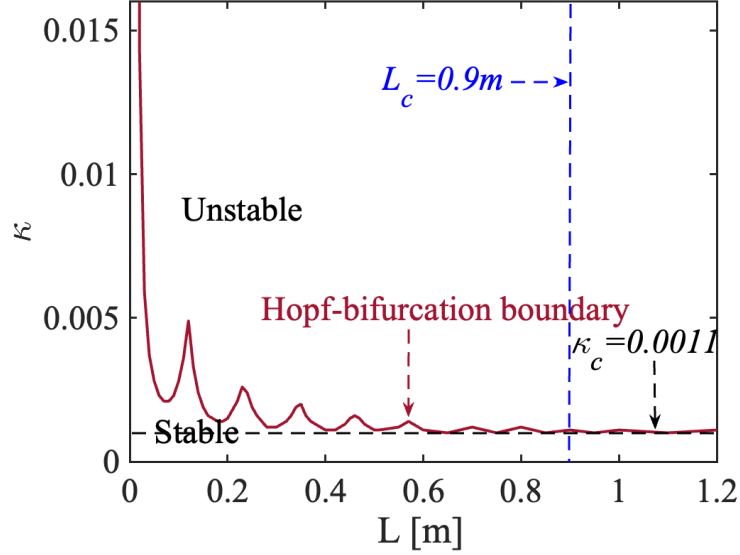


Figure 5.2: State diagram for an SLOF sensing system. Red line: Hopf-bifurcation boundary, where period-one state is above the boundary and stable state is below the boundary. Blue vertical dash line: critical external cavity length L_c . Black horizontal dash line: constant feedback strength κ_c .

stabilized [31,66,67,158] and tended to a constant feedback strength (e.g., $\kappa_c = 0.0011$ for current system parameter settings) when L was larger than the critical external cavity length denoted by L_c (e.g., $0.9m$ shown in Figure 5.2). We, hence, set the switching status for this SLOF with L larger than L_c , and κ near the Hopf-bifurcation boundary as the system operating condition. In this case, the laser intensity from the SLOF was modulated in a square waveform with its period linked to the external cavity length. In following simulations, we set the initial external cavity length L_0 as $1.5m$.

The phase space plots of Figure 5.3(a)-(c) by corresponding to the three typical nonlinear dynamic states in Figure 5.2: point A is near the Hopf-bifurcation boundary with $\kappa = 0.0011$; point B is in the P1 state with $\kappa = 0.0015$; and point C is in the chaotic state with $\kappa = 0.0065$. The square wave generated near Hopf-bifurcation with a switching period equal to time delay is intriguing, since this is shown in Figure 5.3(a)

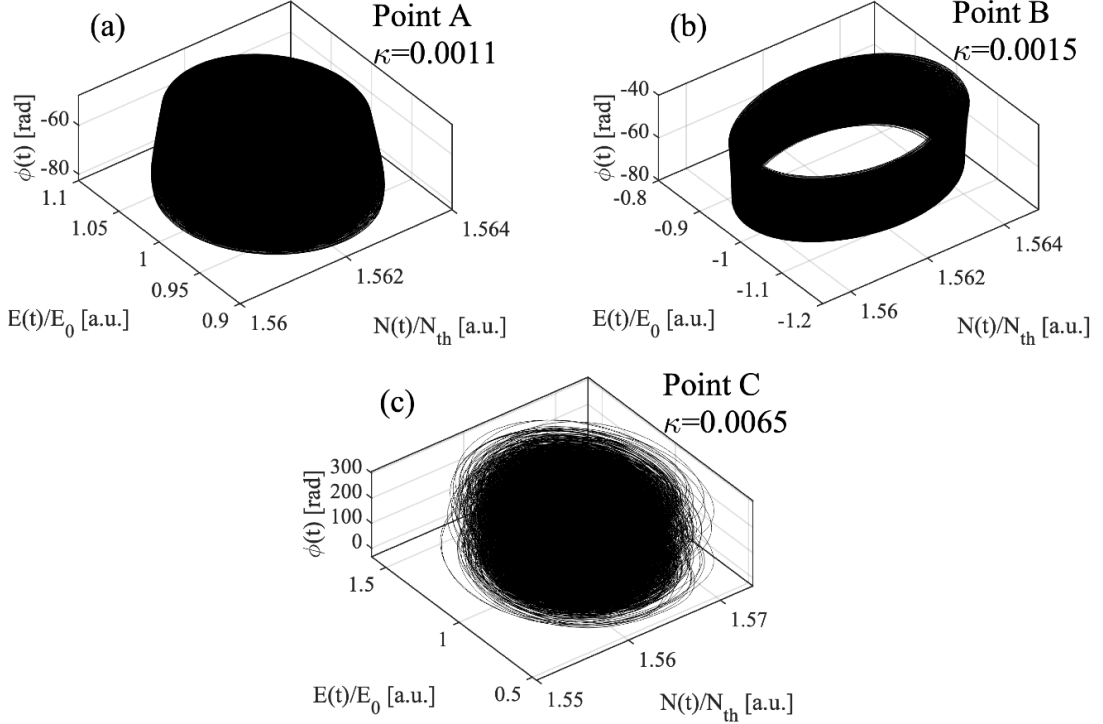


Figure 5.3: Phase space images of point A, point B, and point C, with $\tau = 200ns$ (corresponding $L = 30m$). (a) $\kappa = 0.0011$. (b) $\kappa = 0.0015$. (c) $\kappa = 0.0065$.

to be a coexisting stable limit cycle attractor. As for comparisons, Figure 5.3(b) the attractor forms a circle, which evidences the periodic nature of the output signal that generates from P1 state. The chaotic attractor of Figure 5.3(c) is referred to as a strange attractor and the chaotic trajectory goes around in a multidimensional space.

5.3 Absolute Distance Measurement Principle at Switching Status

To further examine the switching period feature between the stable state and the P1 state in a long-cavity region, we kept the initial external cavity length L_0 fix at $1.5m$, as well as $\alpha = 6$ and $J = 1.1J_{th}$. The total external cavity length L was set at $30m$, $37.5m$, and $45m$ respectively, and their corresponding external cavity round trip times

5.3. Absolute Distance Measurement Principle at Switching Status

τ are $200ns$, $250ns$, and $300ns$, respectively. The relevant bifurcation diagrams were drawn and are shown in Figure 5.4(a). As we are interested in the influence of feedback strength κ on the SL states. We varied κ from 0 to 0.007 with a step size of 0.0001.

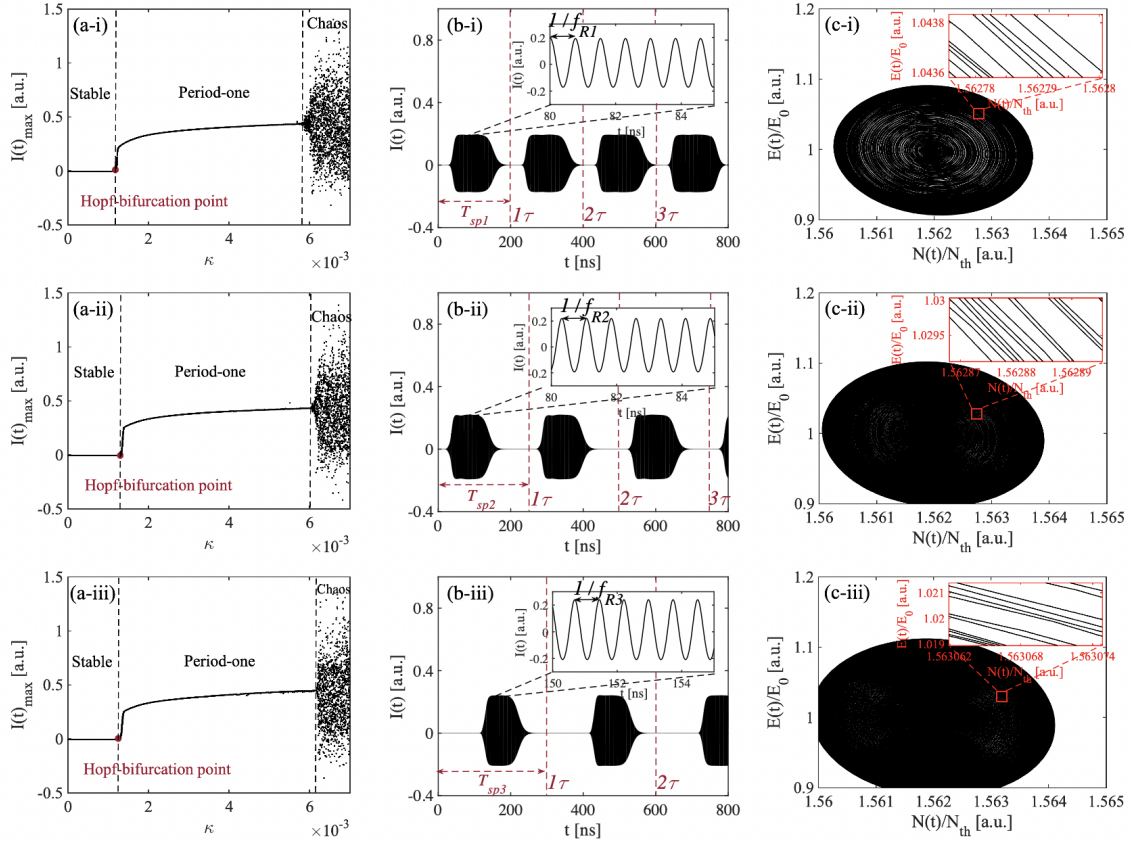


Figure 5.4: (a) Bifurcation diagrams. (b) Time-series signals $I(t)$ near hopf-bifurcation point (that is the switching status). (c) Phase space images near Hopf-bifurcation point. (i) $\tau_1 = 200ns$ (corresponding $L_1 = 30m$). (ii) $\tau_2 = 250ns$ (corresponding $L_2 = 37.5m$). (iii) $\tau_3 = 300ns$ (corresponding $L_3 = 45m$). The inset figures show the enlarged details.

At each κ , we obtained the corresponding maximum intensity $I(t)_{max}$, and present it on the bifurcation diagram in $[I(t)_{max}, \kappa]$ plane, different states are indicated with their corresponded κ ranges. The bifurcation diagrams shown in Figure 5.4(a) clearly indicate the evolution route of the nonlinear dynamics in the SL with OF system, which undergoes from a stable state, P1 state, to chaos state. With the increase of feedback strength κ , undamped relaxation oscillation will occur after the Hopf-

bifurcation point, which causes the system to enter the P1 oscillation state. The time-series signals $I(t)$ can be seen in Figure 5.4(b) with $\kappa_c = 0.0011$, which are near the Hopf-bifurcation boundary. It can be seen that the time-series signal at the Hopf-bifurcation point shows a switching period between the stable state and the P1 state, and the P1 state part displays a high frequency of relaxation oscillation (f_R). Without using any high-speed electronic devices, microwave signals with square wave envelopes are generated by utilizing the inherent dynamics of the laser. The duty cycle is defined as the P1 state part divided by the entire switching period in a time-series signal. The duty cycle of time-series signals show in Figure 5.4(b-i), Figure 5.4(b-ii), and Figure 5.4(b-iii) are 75%, 63%, and 47%, respectively. These resultant photonic microwave signals with the square wave envelope are applicable to radio-over-fiber delivery of timing signals. Additionally, the SL with OF system provides the possibility of realizing a tunable square wave modulated photonic microwave signal generation. In particular, the time-series signals shown in Figure 5.4(b), it clearly reveals that the switching between the stable and P1 states continues with a switching period T_{sp} that is equal to the external cavity round trip time τ . Regarding switching behavior, it have been investigated in Refs. [121, 158]. In following, we make a further study on dynamic behavior by using short-time Fourier transform (STFT) to reveal switching behavior. In addition, Figure 5.5(a)-(c) display the spectrograms corresponding to time-series signals shown in Figure 5.4(b-i)-(b-iii) by performing the STFT on $I(t)$. It reveals the real-time evolution of the spectrum through the Hopf-bifurcation point. From the top view of Figure 5.5, the time-frequency characteristic exhibits a switching between stable and P1 states, accompanied by a period of τ . From side view of Figure 5.5, except for emitting the relaxation oscillation frequencies f_R at $1317.8MHz$, $1322.2MHz$, and $1328.4MHz$, the P1 state also emits other harmonic frequencies, which are integer multiples of the relaxation oscillation frequency including $2f_R$ and

5.3. Absolute Distance Measurement Principle at Switching Status

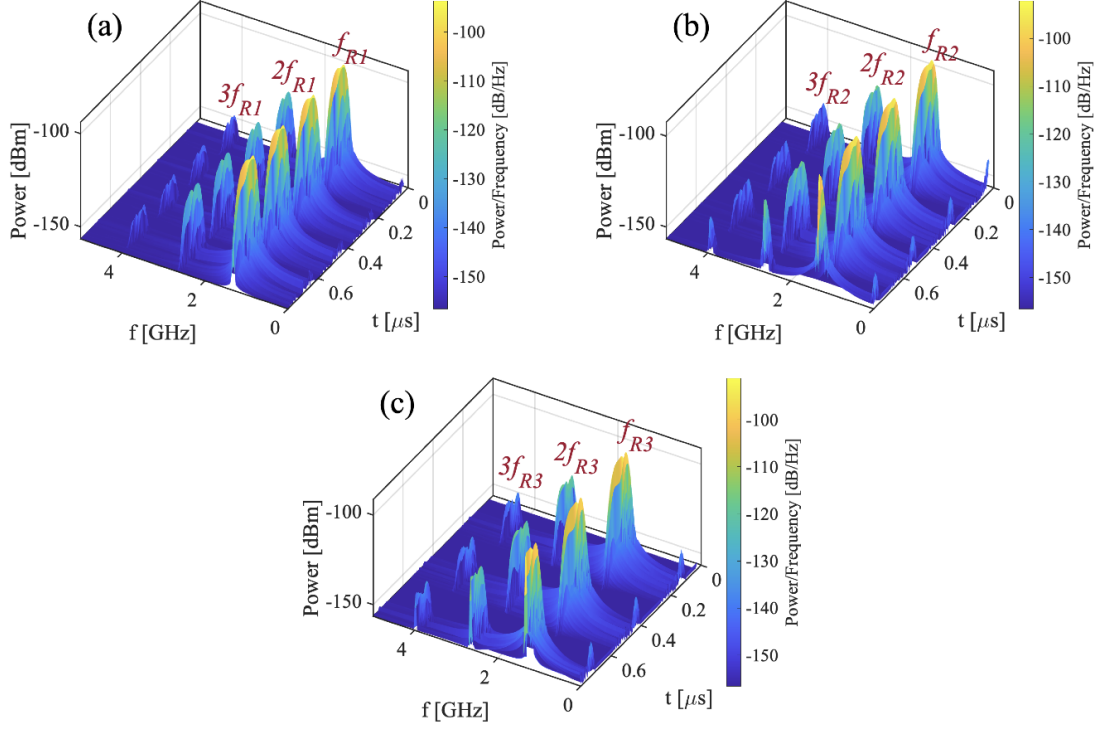


Figure 5.5: STFT spectrograms corresponding to (a) $\tau_1 = 200ns$ (corresponding $L_1 = 30m$). (b) $\tau_2 = 250ns$ (corresponding $L_2 = 37.5m$). (c) $\tau_3 = 300ns$ (corresponding $L_3 = 45m$).

$3f_R$. This is consistent with the typical square wave signal that has equally spaced harmonic frequencies with a concomitant reduction in power. Besides, the time-series signals $I(t)$ shown in Figure 5.4(b) can be better understood by using the phase space diagrams shown in Figure 5.4(c). It can be seen that in each phase space diagram, there are mickle concentric annular circles and each phase space diagram is also a coexisting stable limit cycle attractor, which indicates that the amplitude of the P1 oscillation gradually increases during the transition of the time-series signal $I(t)$ from the stable state to the P1 state, furthermore, the oscillation frequency f_R remain unchanged in each period of P1 oscillation part. All these features realize the regular conversion between two nonlinear dynamic states at the Hopf-bifurcation boundary.

Based on the above studies, an algorithm for utilizing the switching period T_{sp} to

5.3. Absolute Distance Measurement Principle at Switching Status

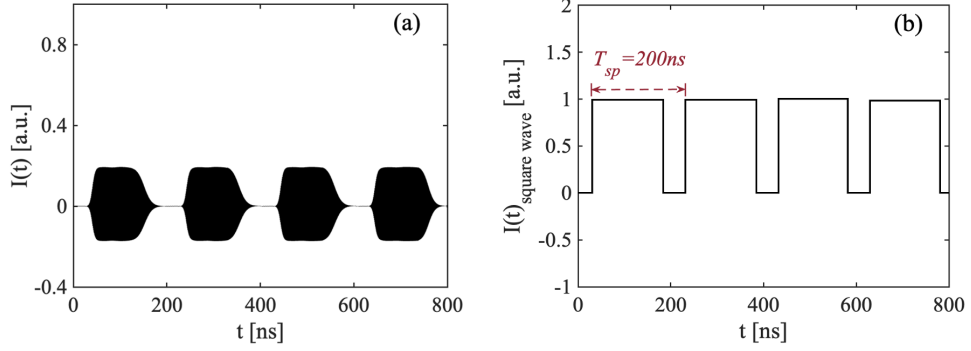


Figure 5.6: (a) Time-series signals $I(t)$ obtained at the switching status with $\tau = 200\text{ns}$ and corresponding $L = 30\text{m}$. (b) Normalized square wave signal $I(t)_{\text{square-wave}}$ obtained from $I(t)$.

measure distance was proposed. Taking the switching signal shown in Figure 5.4(b-i) as an example, the pre-set parameters were $L = 30\text{m}$, $L_0 = 1.5\text{m}$, and $\Delta L = 28.5\text{m}$ unchanged. The $I(t)$ is shown in Figure 5.6(a), we extracted its upper envelope, then, performing normalization and zero-crossing detection, the resultant square wave of $I(t)$ is shown in Figure 5.6(b). The switching period is the time between two raising edges and defined as T_{sp} . In this example, T_{sp} is determined as 200ns . Hence, we can obtain the corresponding recovered distance \hat{L} is 30m by utilizing the relationship of $\hat{L} = cT_{sp}/2$.

As for distance measurements using the proposed square wave generated in an SL with OF, it is critical to maintain the system to robustly operate at the switching status. Hence, it is important to study the impact of the system parameters (κ , J , and α) on the duty cycle and their characteristics. The influence of these parameters is shown in Figure 5.7(a)-(c) with a different varying system parameter, respectively. It can be seen that the duty cycle between 0% to 100% can be obtained for varying each system parameter within a certain range. Figure 5.7(a) shows an available κ from 0.92×10^{-3} to 1.20×10^{-3} , corresponding to the duty cycle between 0% to 100 %, and the SLOF system can be used for distance sensing by measuring the square wave

5.3. Absolute Distance Measurement Principle at Switching Status

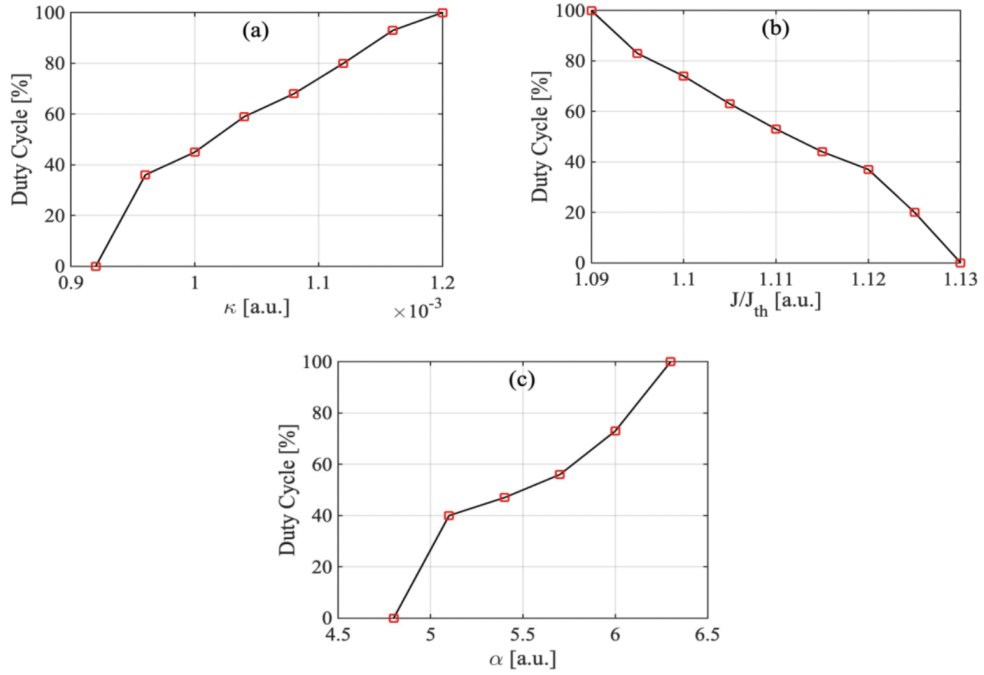


Figure 5.7: (a) The relationship between κ versus duty cycle. (b) The relationship between J versus duty cycle. (c) The relationship between α versus duty cycle.

period. Outside this range, the SLOF system would fully enter into stable state or P1 state and the laser intensity signal will lose its periodicity, therefore, the square wave no longer existed in the system. In Figure 5.7(b), starting from $J/J_{th} = 1.09$ and gradually increasing injection current, the duty cycle tended to decline until it dropped to zero. This means that the SLOF system went from P1 state to stable state by crossing the Hopf-bifurcation boundary. Please note, in the SLOF system, the injection current J is a constant value; the adjustable duty cycle shown in Figure 5.7(b) illustrates the robustness of the SLOF system in terms of injection current and indicates that the SLOF system will not be affected by the current jitter. In Figure 5.7(c), with the increase of α , the duty cycle of the square wave signal gradually increased from 0 % to 100 % within the α range of 4.8 to 6.3. For most SLs, their value of α is around 3~7 [67], therefore, the switching presented in the proposed SLOF system is suitable for most SLs. In summary, with appropriate settings for

these controllable parameters, it can be guaranteed that the switching phenomenon between stable and P1 state can occur, and that these parameters are able to control the duty cycle between $0\% \sim 100\%$. These findings ensure the robustness of the proposed SLOF operating at the switching status for distance measurement.

5.4 Experiments

5.4.1 Experiment results

We conducted a series of experiments and generated $I(t)$ under different L to verify the proposed SLOF sensing system. An experimental set-up is implemented according to the schematic diagram depicted in Figure 5.1. The laser source used in the experiments is a single-mode SL (Hitachi, HL8325) with a wavelength of $830nm$. This SL is driven by the laser controller (Thorlabs, ITC4001). The working temperature was $T = 25^{\circ}C \pm 0.01^{\circ}C$, the injection threshold current was $J_{th} = 42mA$, and the injection current was chosen at $J = 46.2mA$. A small piece of mirror was used as the external target to provide sufficient optical feedback. The OA in Figure 5.1 is used to adjust optical feedback amount in the experiment. The light is split via a 50/50 BS and a direct part of light went into the external PD (Thorlabs, PDA8GS). A high speed OSC (Tektronix, DSA70804) with a maximum sampling rate of $25GS/s$ and analog bandwidth of $8GHz$ was used to observe square wave signals.

As examples, we performed two different experiments to test our proposed SLOF system. In experiment 1, we denoted the total distance as $L_1 = 22.500m$, in experiment 2, we denoted the total distance as $L_2 = 25.000m$. For the convenience of the experiments, with the aid of fiber, we experimentally implement a long-distance sensing system that has the initial external cavity length $L_0 = 20.000m$. Then, the target was placed away from the fiber end with $\Delta L_1 = 2.500m$ and $\Delta L_2 = 5.000m$, respec-

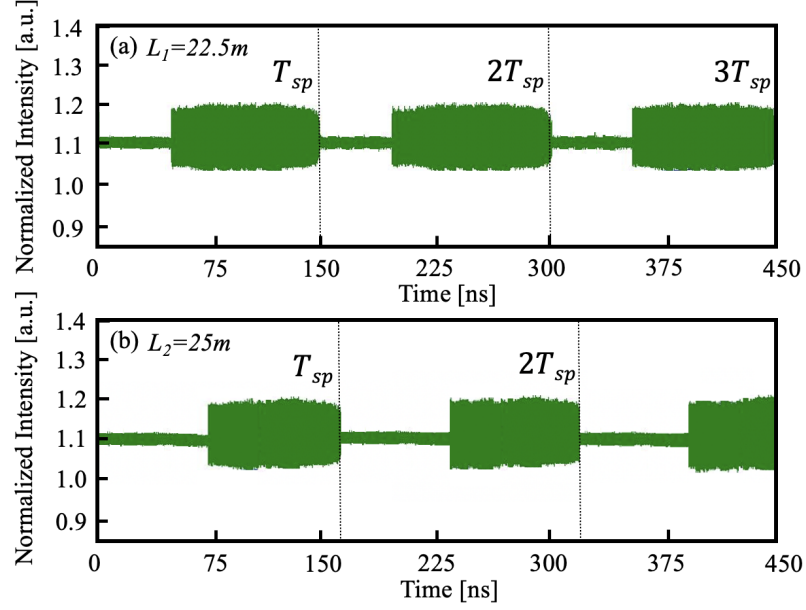


Figure 5.8: (a) Experimental square wave signal $I(t)$ with $L_1 = 22.500m$. (b) Experimental square wave signal $I(t)$ with $L_2 = 25.000m$.

tively. The related experimental square wave signals can be observed and recorded by the OSC and shown in Figure 5.8(a)-(b). From the experimental signals, we can determine the T_{sp} are 150.04ns and 166.68ns, respectively. Therefore, by using the relationship of $\hat{L} = cT_{sp}/2$, the corresponding recovered \hat{L} are 22.506m and 25.002m, which are both very close to the pre-set values 22.500m and 25.000m. As shown in Figure 5.9, in this real-time measurement prototype, we have repeated experiments for different distances under the same experimental operating conditions and keep good optical reflection, the results agree with the pre-set values.

Regarding the measurement accuracy, the switching period T_{sp} depends on the total optical length, which includes free space, fiber, BS, etc. However, in the proposed approach, there is no need to know the length of each part. We only need to set the SL operates at switching status by adjusting the feedback strength. The switching status can be recognized by observing laser intensity signals in the square waveform. Once switching status is achieved, from measuring T_{sp} , the total length which covered

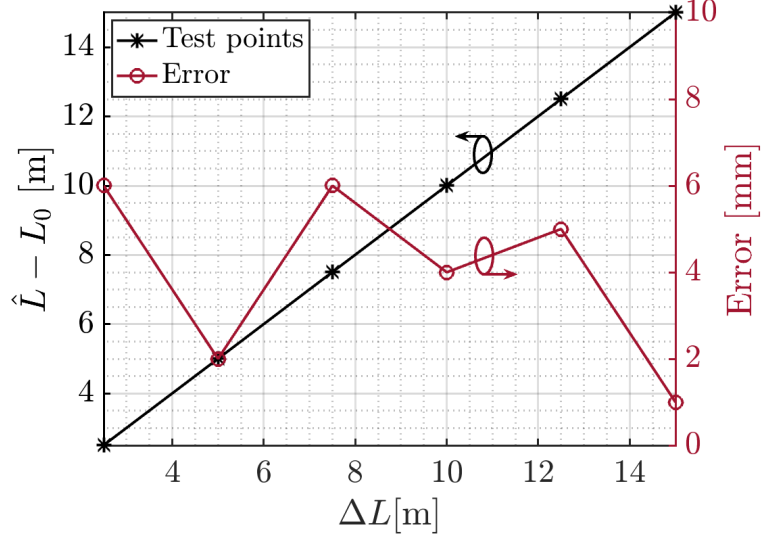


Figure 5.9: Absolute distance measurements results.

all parts can, thus, be obtained. And theoretically, there is no measurement range limitation in proposed SLOF system. Besides, as shown in Figure 5.7, as long as the SLOF system operates in the switching status between stable state and P1 state, the duty cycle is between 0% and 100% and the laser intensity signal will have its periodicity square wave character. Then, the proposed approach can be used to perform the distance measurement. Therefore, the change of the feedback strength by using an OA within a certain range will not affect the distance measurement results. Additionally, regarding measurement uncertainty, we will make a further study in next section. The measurement uncertainty mainly depends on whether the fixed-length section can be fully protected from other disturbances, maintain the original fixed value, and avoid the time measurement uncertainty.

5.4.2 Measurement uncertainty

As shown in Figure 5.1, to clear make the analysis of measurement uncertainty, we further defined $L_0 = L_{01} + L_{02}$, where L_0 is the initial external cavity length from the

5.4. Experiments

SL facet to the optical hollow fiber coupler C_2 , L_{01} is the free space distance between SL facet to coupler C_1 , and L_{02} is the optical fiber between coupler C_1 to coupler C_2 . Considering the air medium index of refraction in free space is n_1 , the active medium index of refraction in hollow fiber is n_2 , and the group index of refraction is n_g . Then, total external cavity length can be described as:

$$\begin{cases} n_g L = n_1 L_{01} + n_2 L_{02} + n_1 \Delta L \\ n_g L = cT_{sp}/2 \end{cases} \quad (5.1)$$

Therefore, we combine two equations in Equation (5.1), we can get ΔL can be described as:

$$\Delta L = \frac{cT_{sp}}{2n_1} - \frac{n_2}{n_1}L_{02} - L_{01} \quad (5.2)$$

From Equation (5.2), we can see that the system uncertainty budget includes $u(T_{sp})$, $u(n_1)$, $u(n_2)$, $u(L_{01})$, and $u(L_{02})$. Then according to the measurement uncertainty synthesis rule and applied on Equation (5.2), we can get Equations (5.3)-(5.4).

$$\begin{aligned} u^2(\Delta L) = & \left[\frac{\partial \Delta L}{\partial n_1}u(n_1)\right]^2 + \left[\frac{\partial \Delta L}{\partial n_2}u(n_2)\right]^2 + \left[\frac{\partial \Delta L}{\partial L_{01}}u(L_{01})\right]^2 \\ & + \left[\frac{\partial \Delta L}{\partial L_{02}}u(L_{02})\right]^2 + \left[\frac{\partial \Delta L}{\partial T_{sp}}u(T_{sp})\right]^2 \end{aligned} \quad (5.3)$$

$$\begin{aligned} u^2(\Delta L) = & \left[\left(\frac{n_2}{n_1^2}L_{02} - \frac{c}{2n_1^2}T_{sp}\right)u(n_1)\right]^2 + \left[\frac{L_{02}}{n_1}u(n_2)\right]^2 + [u(L_{01})]^2 \\ & + \left[\frac{n_2}{n_1}u(L_{02})\right]^2 + \left[\frac{c}{2n_1}u(T_{sp})\right]^2 \end{aligned} \quad (5.4)$$

In free space, the refractive index of ideal air is $n_1 = 1$, and for the refractive index of hollow fiber is $n_2 \approx 1$, therefore, Equation (5.2) can be rewrite as below Equation (5.5), and the corresponding uncertainty is shown in Equation (5.6).

$$\Delta L = \frac{cT_{sp}}{2} - n_2 L_{02} - L_{01} \quad (5.5)$$

$$u(\Delta L) = \sqrt{[n_2 u(L_{02})]^2 + [L_{02} u(n_2)]^2 + [u(L_{01})]^2 + [\frac{c}{2} u(T_{sp})]^2} \quad (5.6)$$

From Equation (5.6), it can be seen that the total uncertainty budget of our proposed SLOF system comes from: $u(n_2)$, $u(L_{02})$, $u(L_{01})$ and $u(T_{sp})$. The corresponding uncertainty analysis for $u(L_{02})$ and $u(n_2)$ can be seen in Figure 5.10(a)-(b).

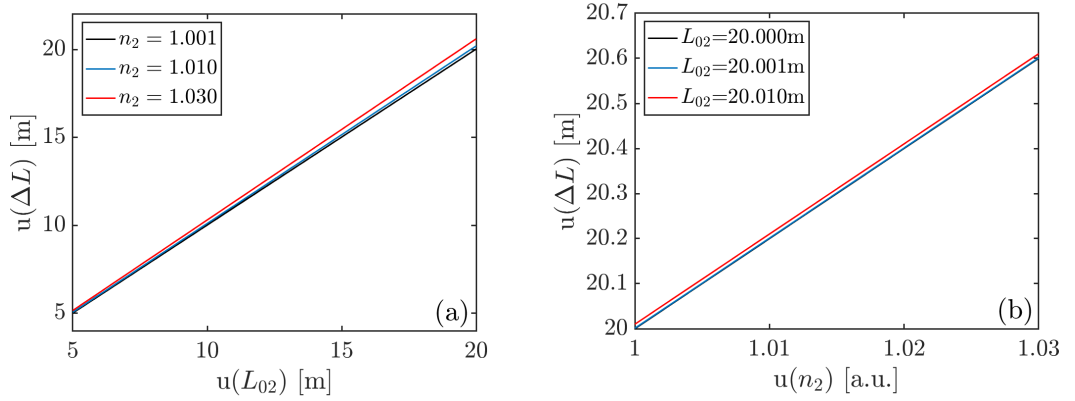


Figure 5.10: (a) The distance measurement uncertainty of L_{02} by introducing different hollow fiber refractive indexes n_2 . (b) The hollow fiber refractive index measurement uncertainty of n_2 by introducing different distances of L_{02} .

For $u(L_{02})$, Figure 5.10(a) shows the distance measurement uncertainty of L_{02} by introducing different hollow fiber refractive indexes n_2 . It can be seen that our proposed SLOF sensing system has great accuracy for most hollow fibers with a refractive index is $n_2 \approx 1$. In addition, it can be seen that the shorter L_{02} is more benefit to realize high precision measurement. L_{02} sets at 5m to achieve the best measurement performance. For $u(n_2)$, Figure 5.10(b) shows the influence of hollow fiber refractive index n_2 on measurement uncertainty. It can be seen that the measurement uncertainty increase with the increase of n_2 . Therefore, accuracy measurement relies on the use of a hollow fiber with an index of refraction close to 1, simultaneously, the accuracy of the length of the hollow fiber used should be guaranteed. For $u(L_{01})$, measurement uncertainty depends on whether the fixed-length section can be sufficiently immune

from external disturbances, retain its original fixed value. For $u(T_{sp})$, the measurement uncertainty of T_{sp} mainly comes from the time resolution of the oscilloscope used. The oscilloscope we used in the experiments had time resolution (T_r) as $0.04ns$, which may cause uncertainty in obtained T_{sp} , it corresponds a resolution of distance measurement (L_r) as $6mm$ by $L_r = cT_r/2$. The measurement resolution depends on the time resolution of the oscilloscope used in the experiment.

5.5 Chapter Summary

We propose a sensing system that realizes distance measurement by operating an SL with OF near the Hopf-bifurcation boundary to generate a switching between stable state and P1 state. To the best of our knowledge, this is the first work proposed to use the switching period near Hopf-bifurcation boundary for long-distance measurements. In this work, with the same system configuration as a conventional SMI system, but operating an SL at a different status, the proposed sensing system was able to achieve longer distance and relatively high resolution and to lift the restrictions in SMI that require electrical/optical modulation. In addition, the proposed sensing approach can achieve distance sensing beyond half coherent length. Furthermore, the influence of system controllable parameters on the duty cycle of the generated square wave sensing signals is also investigated. The result shows that each system controllable parameter has a wide available range. This has ensured that the proposed SL with OF system at switching can work robustly for long-distance sensing.

Chapter 6

Conclusion

6.1 Research Contributions

In conclusion, optical feedback (OF) is a widely developed perturbation to semiconductor lasers (SLs). SL dynamics based on OF scheme are investigated in the numerical, theoretical, and experimental study in this thesis. The SL with OF system reflects the minimum parts count scheme, which has high practical value for engineering implementation. In this thesis, differentiating prior works in the community, we operate SL with OF scheme generating diverse and novel laser dynamics with unique applications demonstrated for sensing applications, and found that the proposed system has the great capability to achieve both displacement and absolute distance sensing applications with high resolution and wide measurement range, by using time-frequency information, relaxation oscillation information, and nonlinear dynamic characteristics carried in SLs emit signals.

Under stable operating conditions, the SL biased by a constant current usually emits a constant intensity laser. However, with the perturbation of external optical feedback, the laser becomes unstable. SL will oscillate from steady state to the period-one (P1) state by crossing the Hopf-bifurcation, which cannot be described by

the existing analytical self-mixing interferometry (SMI) model in stable state. The laser output signal of the system shows some new characteristics. It is worth noting that in the P1 state, the system modulates the laser light output power to generate microwave photonic (MWP) signals. In this thesis, external OF are utilized to operate SL in the P1 state and find that the proposed system has the advantages of realizing high resolution and wide measurement range in sensing applications by using the amplitude, frequency, and envelope information carried in the MWP signals. Based on the extensive theoretical simulation and experimental results in this thesis, the following contributions can be illustrated:

First, we proposed a measurement algorithm for recovering the displacement based on the MWP generation scheme in SL and OF systems. The highlight of this system is that it can directly generate wide-tunable narrow linewidth microwave signals without using any microwave input, electronic circuits or any filters. Different from the traditional MWP generation method, the designed nonlinear dynamics use external OF to perturb the SL source to make the system work in the P1 dynamic state, thereby generating regular microwave oscillation. The fourth-order Runge-Kutta method is used to solve the Lang-Kobayashi differential equation, delimit the boundary of different nonlinear dynamic states, and make the system generate stable and sustainable MWP signals. The availability and ease use of SL in various configurations make this scheme more flexible and stable. After determining the P1 state boundary of SL with OF system, the influence of SL controllable parameters on the boundary is studied. Obtained a set of parameter selection rules for designing SL based MWP displacement sensing system. In particular, a measurement algorithm for recovering the displacement from the MWP sensing signal has also been developed. By making full use of the sensing information carried by the MWP signal amplitude and frequency, high resolution and high sensitivity displacement sensing can be realized. Both simulation and experiment

verify the proposed method and show that it can achieve high measurement sensitivity and high resolution sensing. [**Publication involved: J1, C1**]

Second, SL with OF has rich nonlinear dynamic states. Under the influence of appropriate system controllable parameters, the system will pass through the Hopf-bifurcation and enter the P1 oscillation, accompanied by an undamping relaxation oscillation frequency. By solving the Lang-Kobayashi delay differential equation, then studying the detailed relationship between the relaxation oscillation frequency of the MWP signal and the length of the external cavity. The displacement measurement formula is thus obtained. In addition, the mode-hopping, frequency-hopping, and sawtooth-like phenomena in the relaxation oscillation are fully considered, and the relevant signal processing algorithm is developed for enhancing the sensing range. The experimental verification results show that the proposed MWP displacement sensing system, by only using relaxation oscillation information, is helpful for designing a prototype of a compact displacement sensor with wide measurement range and high resolution. [**Publication involved: J2**]

Third, without using any high-speed electronic and optical equipment, the inherent dynamics of the laser is used to generate a square wave signal in switching status. By operating the SL with the OF system near the Hopf-bifurcation boundary, then, propose a long-distance measurement method in the SL with OF system. In this system, a square wave modulated photonic microwave signal will be generated, accompanied by a switching period between the steady state and the P1 state. The relationship between the switching period and the round-trip time of the external cavity is studied. It is found that the square wave switching period is equal to the round-trip time of the external cavity, which allows us to develop a new long-distance measurement method. Further, the influence of the system's controllable parameters on the duty cycle of square wave signals is also studied. And a wide tuning range of the duty cycle

from 0% \sim 100% is realized. The long-distance measurement achieved by this SL with OF system has strong robustness and is accompanied by a small average error.

[Publication involved: J3]

6.2 Future Works

Though a lot of research work have been done in the field of this thesis, still many interesting topics are need to be further investigated for improving SL with OF sensing system. The following topics are recommended for future research:

(1) Reduce system implementation costs. Due to the internal photodetector (PD) bandwidth of the Fabry-Perot laser diode (FP-LD) could not meet the requirement to capture P1 microwave high-frequency signals. In this thesis work, the internal PD is replaced by external fast PD to capture high-frequency oscillation in the microwave wave region for the convenience of research analysis. In order to reduced system burden, it should take consideration in adopting acquisition system and digital signal processing in the future work and focus on reducing the costs. A possible approach could be that mixing the P1 microwave frequency signal and a reference sinusoidal signal with the frequency around laser solitary frequency, and then applying a low-pass filter with cutoff frequency to down-convert to the low-frequency region around several MHz . Therefore, the sampler burden can be relieved, and thus the cost can be reduced. The future work will focus on this point to design the system so that to find more potential practical applications.

(2) Improve system frequency stability. The frequency stability of the LD used in the sensing system is a quite important parameter, which can induce the frequency jitter of the generated P1 microwave signal. In this thesis work, we have investigated the influence of controllable parameters on P1 microwave frequency, and the results show that P1 microwave frequency is sensitive to injection current, but not to feed-

back strength, an accurate current source for controlling the LD should be employed, thereby, good stability of microwave frequency can be achieved. In future work, other modulation methods should be tried to further improve the signal-to-noise ratio and reduce frequency jitter for achieving a further frequency stability, so as to improve the performance of the sensing system.

(3) Further refinement of the theoretical model. Considering the effect of spontaneous emission and statistical Langevin noises. Langevin sources are random noises induced by the quantum effects of spontaneous emission of light and by a noise originating from random carrier generation and recombination, they originate from random shot noise effects [67]. Therefore, adding Langevin noise to the theoretical model allows the model to be closer to the actual environment.

(4) Outlook and potential applications. With the appreciation grew for the universality of rich nonlinear dynamics and laser instabilities, it is clear that the SL with OF system provides an ideal test bed for studying novel dynamical behaviors. This has attracted many mathematicians, physicists, and optical engineers, who have increased the arsenal of insights and techniques available to explore SL dynamics and applications. The rich dynamics readily available in various SL configurations augurs well that the field will remain a fertile area for exploration and exploitation for many years to come. In the future, the proposed optical system can be miniaturized and low-cost to generate microwave signals by applying the photonic integrated circuit to the chip. Opens the door to numerous promising applications in high-precision sensing, microwave photonics, internet of things, etc.

References

- [1] A. L. Schawlow and C. H. Townes, “Infrared and optical masers,” *Physical Review*, vol. 112, no. 6, p. 1940, 1958.
- [2] T. H. Maiman, “Stimulated optical radiation in ruby,” *Nature*, vol. 187, no. 4736, pp. 493–494, 1960.
- [3] A. Javan, W. R. Bennett Jr, and D. R. Herriott, “Population inversion and continuous optical maser oscillation in a gas discharge containing a he-ne mixture,” *Physical Review Letters*, vol. 6, no. 3, pp. 106–110, 1961.
- [4] R. Lang, “Injection locking properties of a semiconductor laser,” *IEEE Journal of Quantum Electronics*, vol. 18, no. 6, pp. 976–983, 1982.
- [5] G. Yabre and J. Le Bihan, “Reduction of nonlinear distortion in directly modulated semiconductor lasers by coherent light injection,” *IEEE Journal of Quantum Electronics*, vol. 33, no. 7, pp. 1132–1140, 1997.
- [6] M. Sciamanna and K. A. Shore, “Physics and applications of laser diode chaos,” *Nature Photonics*, vol. 9, no. 3, pp. 151–162, 2015.
- [7] H. C. and K. P. G. R, “Some demonstrations of the properties of optical masers,” *Contemporary Physics*, vol. 4, no. 6, pp. 435–444, 1963.

- [8] S.-C. Chan, S.-K. Hwang, and J.-M. Liu, “Period-one oscillation for photonic microwave transmission using an optically injected semiconductor laser,” *Optics Express*, vol. 15, no. 22, pp. 14921–14935, 2007.
- [9] B. Nie, Y. Ruan, Y. Yu, Q. Guo, C. Fang, J. Xi, J. Tong, and H. Du, “Achieving long distance sensing using semiconductor laser with optical feedback by operating at switching status,” *Sensors*, vol. 22, no. 3, p. 963, 2022.
- [10] I. Gatare, M. Sciamanna, J. Buesa, H. Thienpont, and K. Panajotov, “Non-linear dynamics accompanying polarization switching in vertical-cavity surface-emitting lasers with orthogonal optical injection,” *Applied Physics Letters*, vol. 88, no. 10, p. 101106, 2006.
- [11] D. S. Wu, R. Slavík, G. Marra, and D. J. Richardson, “Direct selection and amplification of individual narrowly spaced optical comb modes via injection locking: design and characterization,” *Journal of Lightwave Technology*, vol. 31, no. 14, pp. 2287–2295, 2013.
- [12] Y. Chen, H. Winful, and J. Liu, “Subharmonic bifurcations and irregular pulsing behavior of modulated semiconductor lasers,” *Applied Physics Letters*, vol. 47, no. 3, pp. 208–210, 1985.
- [13] H.-F. Liu and W. F. Ngai, “Nonlinear dynamics of a directly modulated 1.55 μm ingaasp distributed feedback semiconductor laser,” *IEEE journal of quantum electronics*, vol. 29, no. 6, pp. 1668–1675, 1993.
- [14] R. H. Blumenthal, “Design of a microwave-frequency light modulator,” *Proceedings of the IRE*, vol. 50, no. 4, pp. 452–456, 1962.

- [15] N. Dagli, “Wide-bandwidth lasers and modulators for rf photonics,” *IEEE Transactions on Microwave Theory and Techniques*, vol. 47, no. 7, pp. 1151–1171, 1999.
- [16] S. C. Chan and J. M. Liu, “Tunable narrow-linewidth photonic microwave generation using semiconductor laser dynamics,” *IEEE Journal of Selected Topics in Quantum Electronics*, vol. 10, no. 5, pp. 1025–1032, 2004.
- [17] J. Capmany and D. Novak, “Microwave photonics combines two worlds,” *Nature Photonics*, vol. 1, no. 6, pp. 319–330, 2007.
- [18] Y.-S. Juan and F.-Y. Lin, “Photonic generation of broadly tunable microwave signals utilizing a dual-beam optically injected semiconductor laser,” *IEEE Photonics Journal*, vol. 3, no. 4, pp. 644–650, 2011.
- [19] S. Pan and Y. Zhang, “Microwave photonic radars,” *Journal of Lightwave Technology*, vol. 38, no. 19, pp. 5450–5484, 2020.
- [20] L. F. Lester, N. A. Naderi, F. Grillot, R. Raghunathan, and V. Kovanis, “Strong optical injection and the differential gain in a quantum dash laser,” *Optics Express*, vol. 22, no. 6, pp. 7222–7228, 2014.
- [21] B. Bortnik, Y. C. Hung, H. Tazawa, B. J. Seo, J. Luo, K. Y. Jen, W. H. Steier, and H. R. Fetterman, “Electrooptic polymer ring resonator modulation up to 165 ghz,” *IEEE Journal of Selected Topics in Quantum Electronics*, vol. 13, no. 1, pp. 104–110, 2007.
- [22] R. J. Steed, L. Ponnampalam, M. J. Fice, C. C. Renaud, D. C. Rogers, D. G. Moodie, G. D. Maxwell, I. F. Lealman, M. J. Robertson, L. Pavlovic, L. Naglic, M. Vidmar, and A. J. Seeds, “Hybrid integrated optical phase-lock loops for

- photonic terahertz sources,” *IEEE Journal of Selected Topics in Quantum Electronics*, vol. 17, no. 1, pp. 210–217, 2011.
- [23] Y.-H. Hung and S.-K. Hwang, “Photonic microwave stabilization for period-one nonlinear dynamics of semiconductor lasers using optical modulation sideband injection locking,” *Optics Express*, vol. 23, no. 5, pp. 6520–6532, 2015.
- [24] Z. Tang, Y. Li, J. Yao, and S. Pan, “Photonics-based microwave frequency mixing: Methodology and applications,” *Laser & Photonics Reviews*, vol. 14, no. 1, 2020.
- [25] X. Wang and G. Li, “Subcarrier frequency enhancement of two-section fabry-perot laser diodes using external optical injection,” *Optics Communications*, vol. 6060, no. 1-3, p. 113–118, 1999.
- [26] F. Li and A. S. Helmy, “Gigahertz to terahertz tunable all-optical single-sideband microwave generation via semiconductor optical amplifier gain engineering,” *Optics Letters*, vol. 38, no. 22, pp. 4542–4545, 2013.
- [27] B. Romeira, J. Javaloyes, J. M. L. Figueiredo, C. N. Ironside, H. I. Cantu, and A. E. Kelly, “Delayed feedback dynamics of liénard-type resonant tunneling-photo-detector optoelectronic oscillators,” *IEEE Journal of Quantum Electronics*, vol. 49, no. 1, pp. 31–42, 2013.
- [28] M. G. Thompson, A. R. Rae, M. Xia, R. V. Penty, and I. H. White, “Ingaas quantum-dot mode-locked laser diodes,” *IEEE Journal of Selected Topics in Quantum Electronics*, vol. 15, no. 3, pp. 661–672, 2009.
- [29] Rosales, R., Merghem, K., Martinez, A., Akrou, T., Turrenc, J.-P., and Accard, “Inas/inp quantum-dot passively mode-locked lasers for 1.55 μm applica-

- tions,” *IEEE Journal of Selected Topics in Quantum Electronics*, vol. 17, no. 5, pp. 1292–1301, 2011.
- [30] C. Y. Lin, F. Grillot, Y. Li, R. Raghunathan, and L. F. Lester, “Characterization of timing jitter in a 5 ghz quantum dot passively mode-locked laser,” *Optics Express*, vol. 18, no. 21, pp. 21932–21937, 2010.
- [31] S.-S. Li, X. Zou, L. Wang, A. Wang, W. Pan, and L. Yan, “Stable period-one oscillations in a semiconductor laser under optical feedback from a narrowband fiber bragg grating,” *Optics Express*, vol. 28, no. 14, pp. 21286–21299, 2020.
- [32] P. Zhou, N. Li, and S. Pan, “Photonic microwave harmonic down-converter based on stabilized period-one nonlinear dynamics of semiconductor lasers,” *Optics Letters*, vol. 44, no. 19, pp. 4869–4872, 2019.
- [33] B. Nie, Y. Ruan, Y. Yu, Q. Guo, J. Xi, and J. Tong, “Period-one microwave photonic sensing by a laser diode with optical feedback,” *Journal of Lightwave Technology*, vol. 38, no. 19, pp. 5423–5429, 2020.
- [34] J. P. Zhuang, X. Z. Li, S. S. Li, and S. C. Chan, “Frequency-modulated microwave generation with feedback stabilization using an optically injected semiconductor laser,” *Optics Letters*, vol. 41, no. 24, pp. 5764–5767, 2016.
- [35] J.-P. Zhuang and S.-C. Chan, “Phase noise characteristics of microwave signals generated by semiconductor laser dynamics,” *Optics Express*, vol. 23, no. 3, pp. 2777–2797, 2015.
- [36] J. Zhuang and S. Chan, “Tunable photonic microwave generation using optically injected semiconductor laser dynamics with optical feedback stabilization,” *Optics Letters*, vol. 38, no. 3, pp. 344–346, 2013.

- [37] S. C. Chan, “Analysis of an optically injected semiconductor laser for microwave generation,” *IEEE Journal of Quantum Electronics*, vol. 46, no. 3, pp. 421–428, 2010.
- [38] S. Donati and S.-K. Hwang, “Chaos and high-level dynamics in coupled lasers and their applications,” *Progress in Quantum Electronics*, vol. 36, no. 2-3, pp. 293–341, 2012.
- [39] T. B. Simpson, J. M. Liu, M. Almulla, N. G. Usechak, and V. Kovanis, “Limit-cycle dynamics with reduced sensitivity to perturbations,” *Physical Review Letters*, vol. 112, no. 2, p. 023901, 2014.
- [40] M. C. Pochet, N. A. Naderi, V. Kovanis, and L. F. Lester, “Modeling the dynamic response of an optically-injected nanostructure diode laser,” *IEEE Journal of Quantum Electronics*, vol. 47, no. 6, pp. 827–833, 2011.
- [41] Hurtado, A., Henning, D. I., Adams, J. M., Lester, and F. L., “Generation of tunable millimeter-wave and thz signals with an optically injected quantum dot distributed feedback laser,” *IEEE Photonics Journal*, vol. 5, no. 4, p. 5900107, 2013.
- [42] T. B. Simpson, J. M. Liu, M. Almulla, and N. G. Usechak, “Linewidth sharpening via polarization-rotated feedback in optically injected semiconductor laser oscillators,” *IEEE Journal of Selected Topics in Quantum Electronics*, vol. 19, no. 4, pp. 1500807–1500807, 2013.
- [43] Y.-H. Hung and S.-K. Hwang, “Photonic microwave amplification for radio-over-fiber links using period-one nonlinear dynamics of semiconductor lasers,” *Optics Letters*, vol. 38, no. 17, pp. 3355–3358, 2013.

- [44] M. Pochet, T. Locke, and N. G. Usechak, “Generation and modulation of a millimeter-wave subcarrier on an optical frequency generated via optical injection,” *IEEE Photonics Journal*, vol. 4, no. 5, pp. 1881–1891, 2012.
- [45] K. Petermann, *Laser diode modulation and noise*, vol. 3. Springer, 1988.
- [46] T. Taimre, M. Nikolić, K. Bertling, Y. L. Lim, T. Bosch, and A. D. Rakić, “Laser feedback interferometry: a tutorial on the self-mixing effect for coherent sensing,” *Advances in Optics and Photonics*, vol. 7, no. 3, pp. 570–631, 2015.
- [47] W. Wang, K. Grattan, A. Palmer, and W. Boyle, “Self-mixing interference inside a single-mode diode laser for optical sensing applications,” *Journal of Lightwave Technology*, vol. 12, no. 9, pp. 1577–1587, 1994.
- [48] G. Van Tartwijk and D. Lenstra, “Semiconductor lasers with optical injection and feedback,” *Quantum and Semiclassical Optics: Journal of the European Optical Society Part B*, vol. 7, no. 2, p. 87, 1995.
- [49] S. Donati, “Developing self-mixing interferometry for instrumentation and measurements,” *Laser & Photonics Reviews*, vol. 6, no. 3, pp. 393–417, 2012.
- [50] R. Lang and K. Kobayashi, “External optical feedback effects on semiconductor injection laser properties,” *IEEE Journal of Quantum Electronics*, vol. 16, no. 3, pp. 347–355, 1980.
- [51] J. Mork, B. Tromborg, and J. Mark, “Chaos in semiconductor lasers with optical feedback: theory and experiment,” *IEEE Journal of Quantum Electronics*, vol. 28, no. 1, pp. 93–108, 1992.
- [52] S. Donati, G. Giuliani, and S. Merlo, “Laser diode feedback interferometer for measurement of displacements without ambiguity,” *IEEE Journal of Quantum Electronics*, vol. 31, no. 1, pp. 113–119, 1995.

- [53] S. Merlo and S. Donati, “Reconstruction of displacement waveforms with a single-channel laser-diode feedback interferometer,” *IEEE Journal of Quantum Electronics*, vol. 33, no. 4, pp. 527–531, 1997.
- [54] Y. Yu, J. Xi, J. F. Chicharo, and T. Bosch, “Toward automatic measurement of the linewidth-enhancement factor using optical feedback self-mixing interferometry with weak optical feedback,” *IEEE Journal of Quantum Electronics*, vol. 43, no. 7, pp. 527–534, 2007.
- [55] Y. Fan, Y. Yu, J. Xi, and J. F. Chicharo, “Improving the measurement performance for a self-mixing interferometry-based displacement sensing system,” *Applied Optics*, vol. 50, no. 26, pp. 5064–5072, 2011.
- [56] Acket, G., Lenstra, D., D. Boef, A., Verbeek, and B., “The influence of feedback intensity on longitudinal mode properties and optical noise in index-guided semiconductor lasers,” *IEEE Journal of Quantum Electronics*, vol. 20, no. 10, pp. 1163–1169, 1984.
- [57] R. W. Tkach and A. R. Chraplyvy, “Regimes of feedback effects in 1.5-m distributed feedback lasers,” *Journal of Lightwave Technology*, vol. 4, no. 11, pp. 1655–1661, 1986.
- [58] D. Guo, M. Wang, and S. Tan, “Self-mixing interferometer based on sinusoidal phase modulating technique,” *Optics Express*, vol. 13, no. 5, pp. 1537–1543, 2005.
- [59] D. Guo and M. Wang, “Self-mixing interferometry based on a double-modulation technique for absolute distance measurement,” *Applied Optics*, vol. 46, no. 9, pp. 1486–1491, 2007.

- [60] M. Wang, “Fourier transform method for self-mixing interference signal analysis,” *Optics & Laser Technology*, vol. 33, no. 6, pp. 409–416, 2001.
- [61] M. Wang and G. Lai, “A self-mixing interferometer using an external dual cavity,” *Measurement Science and Technology*, vol. 14, no. 7, p. 1025, 2003.
- [62] C. Bes, G. Plantier, and T. Bosch, “Displacement measurements using a self-mixing laser diode under moderate feedback,” *IEEE Transactions on Instrumentation and Measurement*, vol. 55, no. 4, pp. 1101–1105, 2006.
- [63] L. Scalise, Y. Yu, G. Giuliani, G. Plantier, and T. Bosch, “Self-mixing laser diode velocimetry: application to vibration and velocity measurement,” *IEEE Transactions on Instrumentation and Measurement*, vol. 53, no. 1, pp. 223–232, 2004.
- [64] U. Zabit, F. Bony, T. Bosch, and A. D. Rakic, “A self-mixing displacement sensor with fringe-loss compensation for harmonic vibrations,” *IEEE Photonics Technology Letters*, vol. 22, no. 6, pp. 410–412, 2010.
- [65] Y. Yu, J. Xi, J. F. Chicharo, and T. Bosch, “Optical feedback self-mixing interferometry with a large feedback factor c : Behavior studies,” *IEEE Journal of Quantum Electronics*, vol. 45, no. 7, pp. 840–848, 2009.
- [66] A. Murakami, J. Ohtsubo, and Y. Liu, “Stability analysis of semiconductor laser with phase-conjugate feedback,” *IEEE Journal of Quantum Electronics*, vol. 33, no. 10, pp. 1825–1831, 1997.
- [67] J. Ohtsubo, *Semiconductor lasers: stability, instability and chaos*, vol. 111. Springer, 2012.
- [68] A. Uchida, *Optical communication with chaotic lasers: applications of nonlinear dynamics and synchronization*. John Wiley & Sons, 2012.

- [69] L.-C. Lin, S.-H. Liu, and F.-Y. Lin, “Stability of period-one (p1) oscillations generated by semiconductor lasers subject to optical injection or optical feedback,” *Optics Express*, vol. 25, no. 21, pp. 25523–25532, 2017.
- [70] M. Zhang, Y. Ji, Y. Zhang, Y. Wu, H. Xu, and W. Xu, “Remote radar based on chaos generation and radio over fiber,” *IEEE Photonics Journal*, vol. 6, no. 5, pp. 1–12, 2014.
- [71] A. Locquet, “Routes to chaos of a semiconductor laser subjected to external optical feedback: A review,” *Photonics*, vol. 7, no. 1, p. 22, 2022.
- [72] Y. Ruan, B. Liu, Y. Yu, J. Xi, Q. Guo, and J. Tong, “Improving measurement sensitivity for a displacement sensor based on self-mixing effect,” *IEEE Photonics Journal*, vol. 10, no. 6, pp. 1–10, 2018.
- [73] C. Cui and S.-C. Chan, “Performance analysis on using period-one oscillation of optically injected semiconductor lasers for radio-over-fiber uplinks,” *IEEE Journal of Quantum Electronics*, vol. 48, no. 4, pp. 490–499, 2012.
- [74] S. D. Cohen, A. Aragonese, D. Rontani, M. Torrent, C. Masoller, and D. J. Gauthier, “Multidimensional subwavelength position sensing using a semiconductor laser with optical feedback,” *Optics Letters*, vol. 38, no. 21, pp. 4331–4334, 2013.
- [75] A. Argyris, D. Syvridis, L. Larger, V. Annovazzi-Lodi, P. Colet, I. Fischer, J. Garcia-Ojalvo, C. R. Mirasso, L. Pesquera, and K. A. Shore, “Chaos-based communications at high bit rates using commercial fibre-optic links,” *Nature*, vol. 438, no. 7066, pp. 343–346, 2005.
- [76] V. Annovazzi-Lodi, M. Benedetti, S. Merlo, T. Perez, P. Colet, and C. R. Mirasso, “Message encryption by phase modulation of a chaotic optical carrier,” *IEEE Photonics Technology Letters*, vol. 19, no. 2, pp. 76–78, 2007.

- [77] V. Annovazzi-Lodi, S. Merlo, M. Norgia, and A. Scirè, “Characterization of a chaotic telecommunication laser for different fiber cavity lengths,” *IEEE Journal of Quantum Electronics*, vol. 38, no. 9, pp. 1171–1177, 2002.
- [78] S. Turovets, J. Dellunde, and K. Shore, “Nonlinear dynamics of a laser diode subjected to both optical and electronic feedback,” *Journal of the Optical Society of America B*, vol. 14, no. 1, pp. 200–208, 1997.
- [79] S. YE and J. Ohtsubo, “Experimental investigation of stability enhancement in semiconductor lasers with optical feedback,” *Optical Review*, vol. 5, no. 5, pp. 280–284, 1998.
- [80] K. A. Shore and D. M. Kane, *Unlocking dynamical diversity: optical feedback effects on semiconductor lasers*. John Wiley & Sons, 2005.
- [81] B. Tromborg, J. Osmundsen, and H. Olesen, “Stability analysis for a semiconductor laser in an external cavity,” *IEEE Journal of Quantum Electronics*, vol. 20, no. 9, pp. 1023–1032, 1984.
- [82] H. Olesen, J. Osmundsen, and B. Tromborg, “Nonlinear dynamics and spectral behavior for an external cavity laser,” *IEEE Journal of Quantum Electronic*, vol. 22, no. 6, pp. 762–773, 1986.
- [83] Y. Fan, Y. Yu, J. Xi, and Q. Guo, “Stability limit of a semiconductor laser with optical feedback,” *IEEE Journal of Quantum Electronics*, vol. 51, no. 2, pp. 1–9, 2014.
- [84] X. Q. Qi and J. M. Liu, “Photonic microwave applications of the dynamics of semiconductor lasers,” *IEEE Journal of Selected Topics in Quantum Electronics*, vol. 17, no. 5, pp. 1198–1211, 2011.

- [85] S. Wieczorek, W. W. Chow, L. Chrostowski, and C. J. Chang-Hasnain, “Improved semiconductor-laser dynamics from induced population pulsation,” *IEEE Journal of Quantum Electronics*, vol. 42, no. 6, pp. 552–562, 2005.
- [86] F. Grillot, C. Wang, N. A. Naderi, and J. Even, “Modulation properties of self-injected quantum-dot semiconductor diode lasers,” *IEEE Journal of Selected Topics in Quantum Electronics*, vol. 19, no. 4, p. 1900812, 2013.
- [87] K. Noguchi, O. Mitomi, and H. Miyazawa, “Millimeter-wave ti:linbo3 optical modulators,” *Journal of Lightwave Technology*, vol. 16, no. 4, pp. 615–619, 1998.
- [88] B. Bortnik, Y. C. Hung, H. Tazawa, B. J. Seo, J. Luo, K. Y. Jen, W. H. Steier, and H. R. Fetterman, “Electrooptic polymer ring resonator modulation up to 165 ghz,” *IEEE Journal of Selected Topics in Quantum Electronics*, vol. 13, no. 1, pp. 104–110, 2007.
- [89] Y. Enami, C. T. Deroose, D. Mathine, C. Loychik, C. Greenlee, R. A. Norwood, T. D. Kim, J. Luo, Y. Tian, and K. Y. Jen, “Hybrid polymer/sol-gel waveguide modulators with exceptionally large electro-optic coefficients,” *Nature Photonics*, vol. 1, no. 3, pp. 180–185, 2007.
- [90] T. Ido and S. Tanaka, “Ultra-high-speed multiple-quantum-well electro-absorption optical modulators with integrated waveguides,” *Journal of Lightwave Technology*, vol. 14, no. 9, pp. 2026–2034, 1996.
- [91] D. Chang, Z. Zhong, A. Valle, W. Jin, S. Jiang, J. Tang, and Y. Hong, “Microwave photonic signal generation in an optically injected discrete mode semiconductor laser,” *Photonics*, vol. 9, no. 3, p. 171, 2022.
- [92] Bordonalli, C. A., Walton, C., Seeds, and J. A., “High-performance phase locking of wide linewidth semiconductor lasers by combined use of optical injection

- locking and optical phase-lock loop,” *Journal of Lightwave Technology*, vol. 17, no. 2, pp. 328–342, 1999.
- [93] K. Balakier, M. J. Fice, L. Ponnampalam, A. J. Seeds, and C. C. Renaud, “Monolithically integrated optical phase lock loop for microwave photonics,” *Journal of Lightwave Technology*, vol. 32, no. 20, pp. 3893–3900, 2014.
- [94] X. Wang and G. Li, “Microwave/millimeter-wave frequency subcarrier lightwave modulations based on self-sustained pulsation of laser diode,” *Journal of Lightwave Technology*, vol. 11, no. 2, pp. 309–315, 1993.
- [95] M. Tang, H. Minamide, Y. Wang, T. Notake, and H. Ito, “Tunable terahertz-wave generation from dast crystal pumped by a monolithic dual-wavelength fiber laser,” *Optics Express*, vol. 19, no. 2, pp. 779–786, 2011.
- [96] Y. N. Tan, L. Jin, L. Cheng, Z. Quan, M. Li, and B. O. Guan, “Multi-octave tunable rf signal generation based on a dual-polarization fiber grating laser,” *Optics Express*, vol. 20, no. 7, pp. 6961–6967, 2012.
- [97] X. S. Yao and L. Maleki, “Multiloop optoelectronic oscillator,” *IEEE Journal of Quantum Electronics*, vol. 36, no. 1, pp. 79–84, 2000.
- [98] X. S. Yao and L. Maleki, “Optoelectronic microwave oscillator,” *Journal of The Optical Society of America*, vol. 13, no. 12, pp. 1725–1735, 1996.
- [99] P. J. Yao, “Wideband and frequency-tunable microwave generation using an optoelectronic oscillator incorporating a fabry–perot laser diode with external optical injection,” *Optics Letters*, vol. 35, no. 11, pp. 1911–1913, 2010.
- [100] J. Y. Kim, J. H. Jo, W. Y. Choi, and H. K. Sung, “Dual-loop dual-modulation optoelectronic oscillators with highly suppressed spurious tones,” *IEEE Photonics Technology Letters*, vol. 24, no. 8, pp. 706–708, 2012.

- [101] Romeira, B., Seunarine, K., Ironside, N. C., Kelly, E. A., Figueiredo, and M. L. J., “A self-synchronized optoelectronic oscillator based on an rtd photodetector and a laser diode,” *IEEE Photonics Technology Letters*, vol. 23, no. 16, pp. 1148–1150, 2011.
- [102] R. Rosales, K. Merghem, A. Martinez, A. A. Akrou, J. J. Turrenc, A. Accard, F. Lelarge, and A. Ramdane, “Inas/inp quantum-dot passively mode-locked lasers for 1.55- μ m applications,” *IEEE Journal of Selected Topics in Quantum Electronics*, vol. 17, no. 5, pp. 1292–1301, 2011.
- [103] J. Chen, H. Zhu, W. Xia, D. Guo, H. Hao, and M. Wang, “Self-mixing birefringent dual-frequency laser doppler velocimeter,” *Optics Express*, vol. 25, no. 2, pp. 560–572, 2017.
- [104] P. Perez, A. Quirce, A. Valle, A. Consoli, I. Noriega, L. Pesquera, and I. Esquivias, “Photonic generation of microwave signals using a single-mode vcsel subject to dual-beam orthogonal optical injection,” *IEEE Photonics Journal*, vol. 7, no. 1, pp. 1–14, 2015.
- [105] H. Lin, D. W. Pierce, A. J. Basnet, A. Quirce, Y. Zhang, and A. Valle, “Two-frequency injection on a multimode vertical-cavity surface-emitting laser,” *Optics Express*, vol. 19, no. 23, pp. 22437–22442, 2011.
- [106] C. Xue, D. Chang, Y. Fan, S. Ji, Z. Zhang, H. Lin, P. S. Spencer, and Y. Hong, “Characteristics of microwave photonic signal generation using vertical-cavity surface-emitting lasers with optical injection and feedback,” *Journal of the Optical Society of America B*, vol. 37, no. 5, pp. 1394–1400, 2020.
- [107] M. J. Wishon, D. Choi, T. Niebur, N. Webster, Y. K. Chembo, E. A. Viktorov, D. S. Citrin, and A. Locquet, “Low-noise x-band tunable microwave generator

- based on a semiconductor laser with feedback,” *IEEE Photonics Technology Letters*, vol. 30, no. 18, pp. 1597–1600, 2018.
- [108] A. V. Kovalev, M. S. Islam, A. Locquet, D. Citrin, E. A. Viktorov, and T. Erneux, “Resonances between fundamental frequencies for lasers with large delayed feedbacks,” *Physical Review E*, vol. 99, no. 6, p. 062219, 2019.
- [109] S. C. Chan, S. K. Hwang, and J. M. Liu, “Radio-over-fiber am-to-fm upconversion using an optically injected semiconductor laser,” *Optics Letters*, vol. 31, no. 15, pp. 2254–2256, 2006.
- [110] C. Wang, R. Raghunathan, K. Schires, S. C. Chan, L. F. Lester, and F. Grillot, “Optically injected inas/gaas quantum dot laser for tunable photonic microwave generation,” *Optics Letters*, vol. 41, no. 6, pp. 1153–1156, 2016.
- [111] Yu-Han, Hung, Cheng-Hao, Chu, Sheng-Kwang, and Hwang, “Optical double-sideband modulation to single-sideband modulation conversion using period-one nonlinear dynamics of semiconductor lasers for radio-over-fiber links,” *Optics Letters*, vol. 38, no. 9, pp. 1482–1484, 2013.
- [112] C. Cui, X. Fu, and S.-C. Chan, “Double-locked semiconductor laser for radio-over-fiber uplink transmission,” *Optics Letters*, vol. 34, no. 24, pp. 3821–3823, 2009.
- [113] M. Zhang, T. Liu, A. Wang, J. Zhang, and Y. Wang, “All-optical clock frequency divider using fabry–perot laser diode based on the dynamical period-one oscillation,” *Optics Communications*, vol. 284, no. 5, pp. 1289–1294, 2011.
- [114] S. C. Chan and J. M. Liu, “Microwave frequency division and multiplication using an optically injected semiconductor laser,” *IEEE Journal of Quantum Electronics*, vol. 41, no. 9, pp. 1142–1147, 2005.

- [115] H. Ukita, Y. Uenishi, and Y. Katagiri, “Applications of an extremely short strong-feedback configuration of an external-cavity laser diode system fabricated with gaas-based integration technology,” *Applied Optics*, vol. 33, no. 24, pp. 5557–5563, 1994.
- [116] O. D. Bernal, U. Zabit, and T. M. Bosch, “Robust method of stabilization of optical feedback regime by using adaptive optics for a self-mixing micro-interferometer laser displacement sensor,” *IEEE Journal of Selected Topics in Quantum Electronics*, vol. 21, no. 4, pp. 336–343, 2014.
- [117] P. Zhou, F. Zhang, X. Ye, Q. Guo, and S. Pan, “Flexible frequency-hopping microwave generation by dynamic control of optically injected semiconductor laser,” *IEEE Photonics Journal*, vol. 8, no. 6, pp. 1–9, 2016.
- [118] C. Grebogi, E. Ott, and J. A. Yorke, “Chaos, strange attractors, and fractal basin boundaries in nonlinear dynamics,” *Science*, vol. 238, no. 4827, pp. 632–638, 1987.
- [119] Victor, Contreras, Horacio, Martinez, Michele, and Norgia, “Phase shift measurements between intensity and frequency modulations of a self-mixing interferometer,” *IEEE Photonics Technology Letters*, vol. 30, no. 22, pp. 1909–1912, 2018.
- [120] D. Guo, H. Jiang, L. Shi, and M. Wang, “Laser self-mixing grating interferometer for mems accelerometer testing,” *IEEE Photonics Journal*, vol. 10, no. 1, pp. 1–9, 2018.
- [121] J.-X. Dong, J.-P. Zhuang, and S.-C. Chan, “Tunable switching between stable and periodic states in a semiconductor laser with feedback,” *Optics Letters*, vol. 42, no. 21, pp. 4291–4294, 2017.

- [122] P. Zhou, F. Zhang, Q. Guo, S. Li, and S. Pan, “Reconfigurable radar waveform generation based on an optically injected semiconductor laser,” *IEEE Journal of Selected Topics in Quantum Electronics*, vol. 23, no. 6, pp. 1–9, 2017.
- [123] L. Li, X. Yi, S. X. Chew, S. Song, L. Nguyen, and R. A. Minasian, “Double-pass microwave photonic sensing system based on low-coherence interferometry,” *Optics Letters*, vol. 44, no. 7, pp. 1662–1665, 2019.
- [124] H. Chen, B. Nakarmi, M. R. Uddin, and S. Pan, “Optical behavior analysis of negative wavelength detuning in smfp-laser and its effect on multi-rf generation,” *IEEE Photonics Journal*, vol. 11, no. 1, pp. 1–9, 2019.
- [125] L. Fan, Z.-M. Wu, T. Deng, J.-G. Wu, X. Tang, J.-J. Chen, S. Mao, and G.-Q. Xia, “Subharmonic microwave modulation stabilization of tunable photonic microwave generated by period-one nonlinear dynamics of an optically injected semiconductor laser,” *Journal of Lightwave Technology*, vol. 32, no. 23, pp. 4660–4666, 2014.
- [126] A. Zhao, N. Jiang, S. Liu, C. Xue, and K. Qiu, “Wideband time delay signature-suppressed chaos generation using self-phase-modulated feedback semiconductor laser cascaded with dispersive component,” *Journal of Lightwave Technology*, vol. 37, no. 19, pp. 5131–5139, 2019.
- [127] Y. Tan, W. Wang, C. Xu, and S. Zhang, “Laser confocal feedback tomography and nano-step height measurement,” *Scientific Reports*, vol. 3, p. 2971, 2013.
- [128] B. Liu, Y. Yu, J. Xi, Q. Guo, J. Tong, and R. A. Lewis, “Displacement sensing using the relaxation oscillation frequency of a laser diode with optical feedback,” *Applied Optics*, vol. 56, no. 24, pp. 6962–6966, 2017.

- [129] Y. Ruan, B. Liu, Y. Yu, J. Xi, Q. Guo, and J. Tong, “High sensitive sensing by a laser diode with dual optical feedback operating at period-one oscillation,” *Applied Physics Letters*, vol. 115, no. 1, p. 011102, 2019.
- [130] C. Meritxell and A. Andrés, “Forecasting events in the complex dynamics of a semiconductor laser with optical feedback,” *Scientific Reports*, vol. 8, no. 1, p. 10741, 2018.
- [131] B. Nie, Y. Ruan, Z. Chen, Y. Yu, Q. Guo, J. Xi, and J. Tong, “State boundaries in a laser diode with optical feedback and its sensing application,” in *Applications of Lasers for Sensing and Free Space Communications*, pp. LTh4B–7, 2019.
- [132] S. C. Chan, R. Diaz, and J. M. Liu, “Novel photonic applications of nonlinear semiconductor laser dynamics,” *Optical & Quantum Electronics*, vol. 40, no. 2-4, pp. 83–95, 2008.
- [133] S. C. Chan and J. M. Liu, “Frequency modulation on single sideband using controlled dynamics of an optically injected semiconductor laser,” *IEEE Journal of Quantum Electronics*, vol. 42, no. 7, pp. 699–705, 2006.
- [134] J. Hult, “A fourth-order runge–kutta in the interaction picture method for simulating supercontinuum generation in optical fibers,” *Journal of Lightwave Technology*, vol. 25, no. 12, pp. 3770–3775, 2007.
- [135] Q. Cheng, B. Nie, B. Ji, Y. Ruan, and Y. Yu, “Development of a simulation platform for studying the dynamics of a semiconductor laser,” in *Frontiers in Optics*, pp. JW6B–28, 2020.
- [136] A. Ritter and H. Haug, “Theory of laser diodes with weak optical feedback. i. small-signal analysis and side-mode spectra,” *Journal of the Optical Society of America B*, vol. 10, no. 1, pp. 130–144, 1993.

- [137] D. Lenstra, “Relaxation oscillation dynamics in semiconductor diode lasers with optical feedback,” *IEEE Photonics Technology Letters*, vol. 25, no. 6, pp. 591–593, 2013.
- [138] Y. Yu, J. Xi, and J. F. Chicharo, “Measuring the feedback parameter of a semiconductor laser with external optical feedback,” *Optics Express*, vol. 19, no. 10, pp. 9582–9593, 2011.
- [139] Y. Yu, G. Giuliani, and S. Donati, “Measurement of the linewidth enhancement factor of semiconductor lasers based on the optical feedback self-mixing effect,” *IEEE Photonics Technology Letters*, vol. 16, no. 4, pp. 990–992, 2004.
- [140] Y. Ruan, B. Liu, Y. Yu, J. Xi, Q. Guo, and J. Tong, “Measuring linewidth enhancement factor by relaxation oscillation frequency in a laser with optical feedback,” *Sensors*, vol. 18, no. 11, p. 4004, 2018.
- [141] Y. Fan, K. Li, P. Li, B. Copner, and N. Copner, “Linewidth sharpening in optical frequency combs via a gain switched semiconductor laser with external optical feedback,” *Journal of Lightwave Technology*, vol. 39, no. 1, pp. 105–111, 2020.
- [142] S. Donati, D. Rossi, and M. Norgia, “Single channel self-mixing interferometer measures simultaneously displacement and tilt and yaw angles of a reflective target,” *IEEE Journal of Quantum Electronics*, vol. 51, no. 12, pp. 1–8, 2015.
- [143] U. Zabit, O. D. Bernal, S. Amin, M. F. Qureshi, A. H. Khawaja, and T. Bosch, “Spectral processing of self-mixing interferometric signal phase for improved vibration sensing under weak-and moderate-feedback regime,” *IEEE Sensors Journal*, vol. 19, no. 23, pp. 11151–11158, 2019.

- [144] D. Choi, M. J. Wishon, E. Viktorov, D. Citrin, and A. Locquet, “Nanometric sensing with laser feedback interferometry,” *Optics Letters*, vol. 44, no. 4, pp. 903–906, 2019.
- [145] Z. Chen, Y. Yu, Y. Ruan, B. Nie, J. Xi, Q. Guo, and J. Tong, “Dual-frequency doppler lidar based on external optical feedback effect in a laser,” *Sensors*, vol. 20, no. 21, p. 6303, 2020.
- [146] Z. Duan, Y. Yu, B. Gao, and C. Jiang, “Absolute distance measurement based on multiple self-mixing interferometry,” *Optics Communications*, vol. 389, pp. 270–274, 2017.
- [147] R. Sakuraba, K. Iwakawa, K. Kanno, and A. Uchida, “Tb/s physical random bit generation with bandwidth-enhanced chaos in three-cascaded semiconductor lasers,” *Optics Express*, vol. 23, no. 2, pp. 1470–1490, 2015.
- [148] B. Tykalewicz, D. Goulding, S. Hegarty, G. Huyet, T. Erneux, B. Kelleher, and E. Viktorov, “Emergence of resonant mode-locking via delayed feedback in quantum dot semiconductor lasers,” *Optics Express*, vol. 24, no. 4, pp. 4239–4246, 2016.
- [149] A. Murakami and J. Ohtsubo, “Dynamics and linear stability analysis in semiconductor lasers with phase-conjugate feedback,” *IEEE Journal of Quantum Electronics*, vol. 34, no. 10, pp. 1979–1986, 1998.
- [150] C. Xue, S. Ji, Y. Hong, N. Jiang, H. Li, and K. Qiu, “Numerical investigation of photonic microwave generation in an optically injected semiconductor laser subject to filtered optical feedback,” *Optics Express*, vol. 27, no. 4, pp. 5065–5082, 2019.

- [151] M. Sciamanna, M. Virte, C. Masoller, and A. Gavrielides, “Hopf bifurcation to square-wave switching in mutually coupled semiconductor lasers,” *Physical Review E*, vol. 86, no. 1, p. 016218, 2012.
- [152] Z. Zhong, D. Chang, W. Jin, M. LEE, A. Wang, S. Jiang, J. He, J. Tang, and Y. Hong, “Intermittent dynamical state switching in discrete-mode semiconductor lasers subject to optical feedback,” *Photonics Research*, vol. 9, no. 7, pp. 1336–1342, 2021.
- [153] S. S. Li, X. Z. Li, J. P. Zhuang, G. Mezosi, M. Sorel, and S. C. Chan, “Square-wave oscillations in a semiconductor ring laser subject to counter-directional delayed mutual feedback,” *Optics Letters*, vol. 41, no. 4, pp. 812–815, 2016.
- [154] A. M. Kaplan, G. P. Agrawal, and D. N. Maywar, “Optical square-wave clock generation based on an all-optical flip-flop,” *IEEE Photonics Technology Letters*, vol. 22, no. 7, pp. 489–491, 2010.
- [155] X. Zhang, C. Gu, G. Chen, B. Sun, L. Xu, A. Wang, and H. Ming, “Square-wave pulse with ultra-wide tuning range in a passively mode-locked fiber laser,” *Optics Letters*, vol. 37, no. 8, p. 1334, 2012.
- [156] F. Gouaux, N. Servagent, and T. Bosch, “Absolute distance measurement with an optical feedback interferometer,” *Applied Optics*, vol. 37, no. 28, pp. 6684–6689, 1998.
- [157] Y. Zhao, C. Wang, Y. Zhao, D. Zhu, and L. Lu, “An all-fiber self-mixing range finder with tunable fiber ring cavity laser source,” *Journal of Lightwave Technology*, vol. 39, no. 12, pp. 4217–4224, 2020.

References

- [158] J.-X. Dong, J. Ruan, L. Zhang, J.-P. Zhuang, and S.-C. Chan, “Stable-unstable switching dynamics in semiconductor lasers with external cavities,” *Physical Review A*, vol. 103, no. 5, p. 053524, 2021.

Appendix A

Vita

Bairun Nie was born in Henan, China. He received the B.E. degree from the Zhengzhou University, China, and received B.E.(Hon) degree from the University of Wollongong, Australia, both in 2017. Then he received the M.E. degree from the University of Wollongong, Australia, in 2018. The B.E./B.E.(Hon) degrees and M.E. degree are all in Telecommunications Engineering. He will receive Ph.D. degree from the University of Wollongong, Australia, in December 2022.

His research interests include semiconductor laser dynamics, semiconductor laser sensing, photonic microwave, and optical feedback interferometry. He works on both theoretical and experimental aspects.

Appendix B

List of Abbreviations

| | | | |
|-------------|--------------------------------------|-------------|------------------------------|
| OF | optical feedback | VA | variable attenuator |
| OFI | optical feedback interferometry | LC | laser controller |
| SMI | self-mixing interferometry | OSC | oscilloscope |
| PD | photodetector | OI | optical isolator |
| SL | semiconductor laser | RBW | resolution bandwidth |
| MWP | microwave photonics | FFT | fast Fourier transform |
| IF | intermediate frequency | STFT | short-time Fourier transform |
| EO | electrical-to-optical | | |
| OE | optical-to-electrical | | |
| CW | continuous-wave | | |
| PZT | piezoelectric transducer | | |
| LD | laser diode | | |
| BS | beam splitter | | |
| OA | optical attenuator | | |
| LMS | linear motor stage | | |
| SLOF | semiconductor laser optical feedback | | |
| OPLL | optical phase-lock loops | | |
| OEO | optoelectronic oscillator | | |
| RoF | radio over optical fiber | | |
| EOM | electro-optical modulator | | |
| DFB | distributed feedback laser | | |
| L-K | Lang-Kobayashi | | |
| FP | Fabry-Perot | | |
| S | steady | | |
| P1 | period-one | | |
| QP | quasi-period | | |
| C | chaos | | |